Generation and Application of Squeezed States of Light in Higher-Order Spatial Laser Modes

Von der QUEST-Leibniz-Forschungsschule
der Gottfried Wilhelm Leibniz Universität Hannover

zur Erlangung des akademischen Grades
Doktor der Naturwissenschaften
– Dr. rer. nat. –

genehmigte Dissertation

von

M.Sc. Joscha Heinze

2022

Referent:	Apl. Prof. Dr. Benno Willke Gottfried Wilhelm Leibniz Universität Hannover
Korreferent:	Prof. Dr. Karsten Danzmann Gottfried Wilhelm Leibniz Universität Hannover
Korreferent:	Asst. Prof. Dr. Paul Fulda University of Florida
Tag der Promotion:	5. August 2022

A wise person once said:

"Easy peasy laser squeezy."

Abstract

The next generation of gravitational-wave detectors (GWD), formed by the Einstein Telescope (ET) and Cosmic Explorer (CE), aims for improving the currently achieved sensitivities by one order of magnitude which requires significant progress in the overall noise reduction. In this regard, one discussed option for a thermal noise mitigation beyond the current ET and CE baselines is the replacement of the fundamental Gaussian $TEM_{0,0}$ laser mode by a higher-order spatial mode. To justify this approach it is crucial to investigate whether these modes comply with the targets for all other noise sources. In this thesis, this question is investigated with respect to the quantum noise and its reduction via squeezed states of light.

Cavity-enhanced second harmonic generation (SHG) is the first nonlinear process in every GWD squeezed light source. Based on the initial ET design study, the performance of the Laguerre-Gaussian $LG_{3,3}$ mode in this process was analysed first. A numerical model for the $LG_{3,3}$ SHG was developed and showed a good agreement with a corresponding experiment where a conversion efficiency of 45 % could be achieved. However, astigmatism strongly limited the conversion efficiency as well as the output mode purity and the focus then switched to Hermite-Gaussian (HG) modes which are less sensitive in this respect.

The theory on the generation of squeezed states in a type-I optical parametric amplifier was applied to higher-order HG modes, yielding that a $TEM_{0,0}$ SHG in combination with a subsequent spatial light modulator can generate an efficient pump field in a single higher-order mode. Based on these findings, bright squeezed states at a wavelength of 1064 nm in the $TEM_{0,0}$, $HG_{1,1}$, $HG_{2,2}$ and $HG_{3,3}$ mode were generated and characterised via a balanced homodyne detector in the measurement frequency range of 1 MHz to 20 MHz. The achieved benchmark of a quantum noise reduction of 10 dB in the $HG_{1,1}$ mode is a substantial improvement compared to previously published results. 7.5 dB and 4.5 dB in the $HG_{2,2}$ and $HG_{3,3}$ mode, respectively, were primarily limited by the available pump power.

Finally, the shot-noise limited sensitivity of a tabletop Michelson interferometer with balanced homodyne detection, which is the planned readout-scheme topology for future GW detectors, was improved via the generated squeezed states in the frequency range of 1 MHz to 20 MHz. In this thesis, the first successful 10 dB quantum noise reduction in a Michelson interferometer could be demonstrated with the $TEM_{0,0}$ mode at 5 MHz. Moreover, comparable levels of quantum noise reduction, unprecedented for any measurement application, could be achieved for the $HG_{1,1}$ and $HG_{2,2}$ operation at 4 MHz: 8.8 dB and 7.5 dB, respectively. These results were mainly limited by optical loss in the squeezed light injection stage including a Faraday rotator whose aperture caused additional clipping loss for the higher-order modes. At frequencies below 4 MHz, technical laser noise was the main limitation.

These findings are a highly promising step in the feasibility demonstration for an improved thermal noise reduction in gravitational-wave detectors via higher-order spatial modes.

Keywords: higher-order spatial laser modes, squeezed states of light, Michelson interferometer, gravitational-wave detector, mirror thermal noise.

Kurzfassung

Die nächste Generation der Gravitationswellen-Detektoren (GWD), bestehend aus dem Einstein Telescope (ET) und Cosmic Explorer, verfolgt das Ziel, die aktuell erreichten Sensitivitäten um eine Größenordnung zu verbessern. Für die Verringerung des thermischen Spiegelrauschens besteht dabei die Möglichkeit, die aktuell benutzte fundamentale Gauß'sche Lasermode $TEM_{0,0}$ durch höhere räumliche Moden zu ersetzen. Um diesen Vorschlag zu rechtfertigen, muss untersucht werden, ob diese Moden mit den Zielen für alle anderen Rauschquellen vereinbar sind. Die vorliegende Arbeit untersucht diese Frage bezüglich des Quantenrauschens und dessen Reduzierung durch gequetschte Lichtzustände.

Die in einem Resonator verstärkte Frequenzverdopplung (SHG) ist der erste nichtlineare Prozess, der in jeder GWD Quetschlichtquelle zum Einsatz kommt. Basierend auf der ursprünglichen ET Designstudie wurde die Performance der Laguerre-Gauß $LG_{3,3}$ Mode in diesem Prozess untersucht. Ein numerisches Modell der $LG_{3,3}$ SHG wurde entwickelt und zeigte eine hohe Übereinstimmung mit einem entsprechenden Experiment, bei dem eine Konversionseffizienz von 45 % erreicht wurde. Dabei limitierte Astigmatismus sowohl die Effizienz als auch die Ausgangs-Modenreinheit und der Fokus wechselte zu Hermite-Gauß (HG) Moden, die in dieser Hinsicht unempfindlicher sind.

Die Theorie zur Erzeugung von Quetschlicht in einem Typ-I optisch-parametrischen Verstärker wurde auf höhere HG Moden übertragen. Es stellte sich heraus, dass eine $TEM_{0,0}$ SHG kombiniert mit einem räumlichen Lichtmodulator ein effizientes Ein-Moden-Pumpfeld in einer höheren räumlichen Mode erzeugen kann. Mithilfe dieser Erkenntnisse wurden helle Quetschlicht-Zustände bei einer Wellenlänge von 1064 nm in den Moden $TEM_{0,0}$, $HG_{1,1}$, $HG_{2,2}$ und $HG_{3,3}$ erzeugt und in einem Frequenzbereich von 1 MHz bis 20 MHz charakterisiert. Die dabei erreichte Reduzierung des Quantenrauschens um 10 dB in der $HG_{1,1}$ Mode ist eine erhebliche Verbesserung gegenüber zuvor veröffentlichten Ergebnissen. 7.5 dB in der $HG_{2,2}$ und 4.5 dB in der $HG_{3,3}$ Mode waren hauptsächlich durch die verfügbare Pumpleistung begrenzt.

Zuletzt wurde die schrotrausch-limitierte Sensitivität eines Michelson-Interferometers, welches mit der für die künftigen GW-Detektoren geplanten symmetrischen homodynen Detektion betrieben wurde, mithilfe der erzeugten Quetschlicht-Zustände verbessert. In der vorliegenden Arbeit konnte die erste Quantenrausch-Reduktion um 10 dB in einem solchen Interferometer in der $TEM_{0,0}$ Mode bei einer Frequenz von 5 MHz demonstriert werden. Darüber hinaus konnten ähnlich hohe Reduktionslevel von 8.8 dB und 7.5 dB in der $HG_{1,1}$ und $HG_{2,2}$ Mode bei 4 MHz erreicht werden. Diese Ergebnisse waren hauptsächlich durch optische Verluste in dem Faraday-Rotator limitiert, über den die gequetschten Zustände in das Interferometer gekoppelt wurden und der bei den höheren Moden zusätzlich zu Verlusten aufgrund seiner begrenzten Aperturgröße führte. Unterhalb von 4 MHz stellte technisches Laserrauschen die primäre Limitierung dar.

Stichwörter: höhere räumliche Lasermoden, gequetschtes Licht, Michelson-Interferometer, Gravitationswellen-Detektoren, thermisches Spiegelrauschen.

Contents

List of Figures

List of Tables

List of Abbreviations

AR	anti-reflective
BS	beamsplitter
CBTN	coating Brownian thermal noise
CCD	charged coupled device
DBS	dichroic beamsplitter
DOE	diffractive optical element
DPDC	degenerate parametric down-conversion
EOM	electro-optical modulator
FI	Faraday isolator
FR	Faraday rotator
GTR	General Theory of Relativity
GW	gravitational wave
GWD	gravitational-wave detector
HG	Hermite-Gaussian
IMC	input mode cleaner
LG	Laguerre-Gaussian
LIGO	Laser Interferometer Gravitational-Wave Observatory
LISA	Laser Interferometer Space Antenna
LO	local oscillator
MC	mode cleaner
NPRO	non-planar ring oscillator
OMC	output mode cleaner
OPA	optical parametric amplifier
PBS	polarising beamsplitter
PD	photodetector
PDH	Pound-Drever-Hall
PM	powermeter
QN	quantum noise
RF	radio frequency
RPN	radiation pressure noise
SHG	second harmonic generation
SLS	squeezed light source
SMOP	spatial mode of operation
SN	shot noise
SQL	standard quantum limit
STN	suspension thermal noise

Chapter 1

Introduction

1.1 The history of gravitational waves in brief

Starting around 1915, Einstein's General Theory of Relativity (GTR) has brought a fundamentally new concept of gravity into prominence [Ein14]. After having been treated as a force for centuries, gravity was now interpreted as a geometrical perturbation of otherwise flat spacetime. Objects should not fall down and planets should not orbit stars due to an attractive gravitational pull, but because they freely move along geodesics through a curved spacetime [MTW73]. GTR was able to explain the deflection of light by the Sun and the perihelion precession of Mercury, which were not fully understood in Newtonian Gravity [Wil14]. Today, it is, however, even more astonishing that Einstein predicted a new phenomenon which took us no less than one hundred years to observe directly: gravitational waves (GW) [Ein18].

Amongst others, massive objects which perform a spherically asymmetric motion emit gravitational waves as ripples in spacetime that propagate at the speed of light [Sat13]. Such objects may be coalescing compact binaries or asymmetric rotating neutron stars. When these ripples eventually pass the Earth, they cause tiny periodic length changes which were first claimed to be detected by Joseph Weber in 1969 [Web69]. Weber had built two *resonant bar detectors*, solid bodies whose elastic resonances should be excited by a gravitational wave, and thought to have seen correlated signals between them. However, after several other resonant bar detectors failed to reproduce these observations, Weber's results were reanalysed and rejected.

In 1981, Weisberg and Taylor were the first to indirectly validate the existence of gravitational waves through experimental data [WT81]. Analysing the binary Pulsar 1913+16, which had been discovered by Hulse and Taylor six years prior [HT75], showed that its change in orbital period agreed well with what GTR predicted due to gravitational radiation. Their findings were confirmed in 2016, after thirty-five years of observation, with a high degree of confidence [WH16].

Laser interferometers had also been proposed for the direct GW detection in 1963 [GP63]. Compared to resonant bar detectors, interferometers benefit from a broadband sensitivity ranging from a few Hertz to several kilohertz. The TAMA300 detector in Japan started searching for gravitational waves in September 1999, followed by the GEO600 detector in Germany as well as by the first kilometre-scale Laser Interferometer Gravitational-Wave Observatory (LIGO) in the United States in 2002 and by the Virgo detector in Italy in 2007. It then took another nine years of work until, finally, the LIGO and Virgo Collaborations reported that the two LIGO detectors directly observed a gravitational wave for the very first time in September 2015 [Abb+16]. The signal, which swept through the frequencies from 35 Hz to 250 Hz, was produced by the inspiral, merger and ring-down of two black holes at a luminosity distance of 410^{+160}_{-180} Mpc. This observation was awarded with the Nobel prize in 2017 [The17].

This major success enabled a completely new channel to study the Universe. Since then, gravitational-wave detectors (GWD) have further been upgraded and the latest GW catalog lists 94 events from three observation runs [Nit+21]. Better and new methods for reducing the numerous noise sources are continuously investigated—and the next generation of ground-based GWDs as well as the space-based Laser Interferometer Space Antenna (LISA) are already on their way, potentially observing things we do not even expect.

1.2 Gravitational waves and how to detect them

1.2.1 A perturbation of space-time

Gravitational waves can be associated with a small perturbation $h_{\mu\nu}$ of the flat Minkowski metric $\eta_{\mu\nu}$ within the weak-field approximation [MTW73; Adh14]

$$g_{\mu\nu} \simeq \eta_{\mu\nu} + h_{\mu\nu} \,. \tag{1.1}$$

This perturbation can be written in the transverse-traceless gauge as

$$h_{\mu\nu}(z,t) = \begin{pmatrix} 0 & 0 & 0 & 0 \\ 0 & -h_+(z,t) & h_\times(z,t) & 0 \\ 0 & h_\times(z,t) & h_+(z,t) & 0 \\ 0 & 0 & 0 & 0 \end{pmatrix} \,, \tag{1.2}$$

where h_+ and $h_\times$ are two independent polarisations with a 45° angle inbetween. This *strain* acts transverse to the wave's propagation direction and can be visualised by assuming that we measure the distance between two free test masses which are located along the x axis at $x_1 = 0$ and $x_2 = L_0$. Such a measurement may employ a laser beam that is sent from one test mass to the other and reflected back such that the phase of the returning beam can be compared to the source. Assuming that the x axis is aligned with the h_+ polarsation and that the period of the gravitational wave is much longer than the light travel time, the accumulated roundtrip phase reads

$$\varphi_{\mathrm{rt}} = \frac{4\pi}{\lambda} L_0 \left(1 - h_+/2\right) = \frac{4\pi}{\lambda} L' \,. \tag{1.3}$$

Hence, the effect of a gravitational wave can be interpreted as a change in the effective length $L_0 \to L'$. If the same measurement is taken along the y axis, the roundtrip phase would scale with $+h_+/2$; a gravitational wave is quadrupolar in nature and influences perpendicular axes in an anti-correlated manner. This is illustrated in the top row of Figure 1.1 with a ring of test masses that is periodically deformed into an ellipse as a gravitational wave stretches and compresses its dimensions on the x and y axis.

A variety of measurement devices is theoretically capable of detecting gravitational waves. Tracking the periods of radio pulsars via pulsar timing arrays enables the measurement of signals in the frequency range from micro- to nanohertz [Bai+21]. Such a pulsar can be precisely modelled after a thorough study and gravitational-wave signals then appear as certain deviations of the pulse arrival times from this model due to perturbations of the space-time between the source and Earth. Another example is the resonant bar detector. After Weber's rejected claim of having measured a gravitational wave in 1969, a network of this kind of antenna has been developed which today not only aims to measure gravitational waves but also

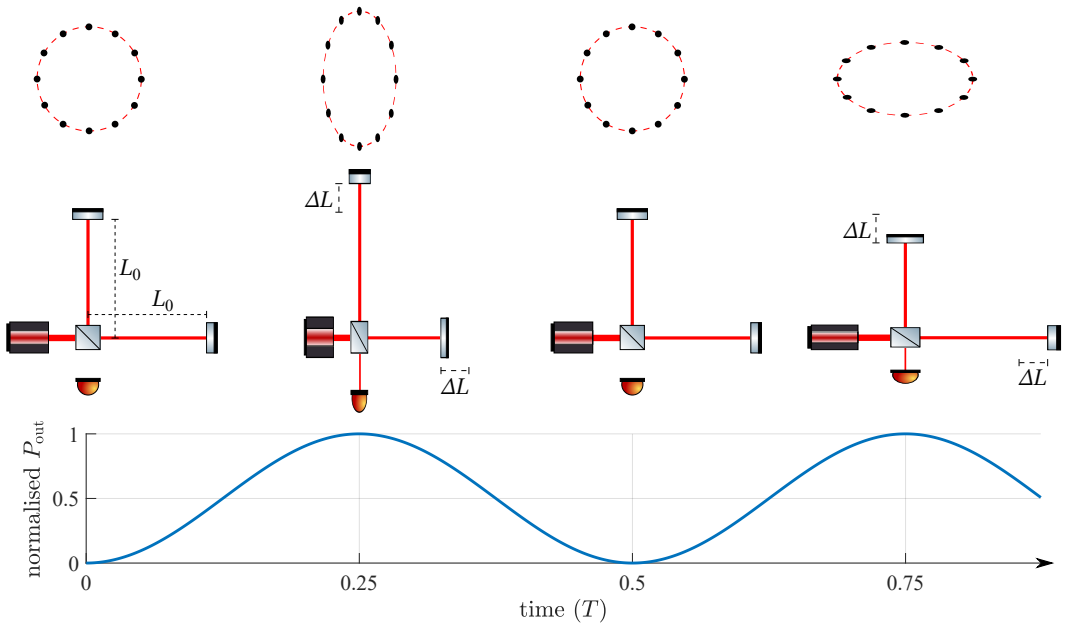

Figure 1.1: The effect of a passing gravitational wave in the h_+ polarisation on a ring of test masses (top), a properly oriented Michelson interferometer (middle) and its output power (bottom). Here, a nominal output power of zero and a ΔL of 1/8th of the light's wavelength are assumed. This ΔL is unrealistically large but allows to display the full-range interferometer response ($0 \leq P_{\text{out}} \leq P_{\text{in}} = 1$) for demonstration purposes. T is the wave's period.

the non-commulative structure of space [SG16]. Finally, primordial gravitational waves may be measured as specific signatures in the polarisation of the cosmic microwave background which statistically cover the whole frequency band down to 10^{-18} Hz. Neither of these strategies has yet been successful in detecting a gravitational wave.

This thesis will solely focus on the probably most prominent and, at the present day, only successful GW detection method which directly uses the quadrupolar nature of a gravitational wave: Michelson interferometers, covering the frequency band from 10^{-4} Hz to 10^{-1} Hz (future space-based) and from 1 Hz to 10^4 Hz (ground-based).

1.2.2 Michelson Interferometers for gravitational-wave detection

Fundamental design and principle

The, so far, only successful gravitational-wave detectors are highly sophisticated Michelson interferometers. In this kind of interferometer as shown in Figure 1.1, an incoming laser beam is split up by a 50:50 beamsplitter into a "north" and "east" arm where the two beams are each reflected back by a highly-reflective end mirror. When the two beams recombine at the beamsplitter, their relative phase determines how they interfere in the input and output port and, thus, how much optical power reaches the photodetector in the output.

The simplest model assumes this experimental design and plane waves. In the symmetric beamsplitter convention, the fields which recombine at the beamsplitter read

$$a_N = \rho a_{\text{in}} e^{i\varphi_N} \qquad \text{and} \qquad a_E = i\tau a_{\text{in}} e^{i\varphi_E}\,, \tag{1.4}$$

where a_{in} is the input field, ρ and τ are the amplitude reflection and transmission coefficients of the beamsplitter, respectively, and $\varphi_{N/E}$ are the phases accumulated in the north and east arm, respectively. The light field in the output then reads

$$\begin{aligned} a_{\text{out}} &= i\tau a_N + \rho a_E \\ &= i\rho\tau a_{\text{in}} e^{i\varphi_c} \left(e^{i\Delta\varphi} + e^{-i\Delta\varphi}\right) \\ &= i a_{\text{in}} e^{i\varphi_c} \cos\Delta\varphi \,, \end{aligned} \tag{1.5}$$

using $\rho = \tau = 1/\sqrt{2}$ and $\cos x = 1/2\left(e^{ix} + e^{-ix}\right)$. Here, $\varphi_c = 1/2\,(\varphi_N + \varphi_E)$ and $\Delta\varphi = 1/2\,(\varphi_N - \varphi_E)$ are defined as the common and differential phase, respectively. Hence, the detected output power is given by

$$P_{\text{out}} = |a_{\text{out}}|^2 = P_{\text{in}} \cos^2\Delta\varphi \tag{1.6}$$

which can be rewritten in terms of the optical arm path lengths L_N and L_E to

$$P_{\text{out}}(\Delta L) = P_{\text{in}} \cos^2(2\Delta L k) \qquad \text{with} \qquad \Delta L := \frac{L_N - L_E}{2} \,, \tag{1.7}$$

where $k = 2\pi n/\lambda$ is the wavenumber with the refractive index n and the wavelength λ. In such an interferometer, the strain of the gravitational wave translates to $h = 2\Delta L/L_0$ (recall Eq. 1.3) where L_0 is the unperturbed north and east arm length.

If the Michelson interferometer is properly aligned to a passing gravitational wave, the wave's quadrupolar nature will cause anti-correlated changes in L_N and L_E and, thus, changes in ΔL. The corresponding gravitational-wave signal then appears in the evolution of P_{out} where further processing and a matching procedure to simulated signals is used for an evaluation and source parameter estimation [CM22].

The operating principle of a Michelson interferometer is optimally sensitive to the gravitational-wave effect. Nevertheless, a detector which only follows this simple design would by far not be sensitive enough for a successful detection. While a complete description of an advanced GW detector is beyond the scope of this thesis, a selection of the advanced techniques which set the overall optical scheme apart from the one in Figure 1.1 are introduced in the following. This shall provide an insight into the complexity of these detectors.

An advanced 2nd generation gravitational-wave detector

The design sensitivities of gravitational-wave detectors require a high laser input power (e.g. 70 W [Bui+20]) to reduce noise in the higher-frequency regime (further explained in Chapter 3). In addition, the high-power input beam is stabilised with respect to intensity, frequency as well as beam jitter and needs to exhibit a high mode purity. This is achieved via a sophisticated pre-stabilised laser system (PSL) [Bod+20] in combination with an input mode cleaner cavity (IMC) (see Fig. 1.2).

As gravitational-wave detectors are sensitive to $\Delta L = hL_0$, large arm lengths L_0 are desired. Practical constraints like construction costs and available land, however, limited the arm lengths of the second-generation gravitational-wave detectors to a few kilometres (LIGO: 4 km, Virgo and KAGRA: 3 km). To increase the arm length artificially, a partially transmissive input test mass (ITM) is added in each interferometer arm to the end test mass (ETM). Together, they form a high-finesse arm cavity which results in a longer interaction time between the gravitational wave and the light while the latter bounces back and forth between these two mirrors. In this

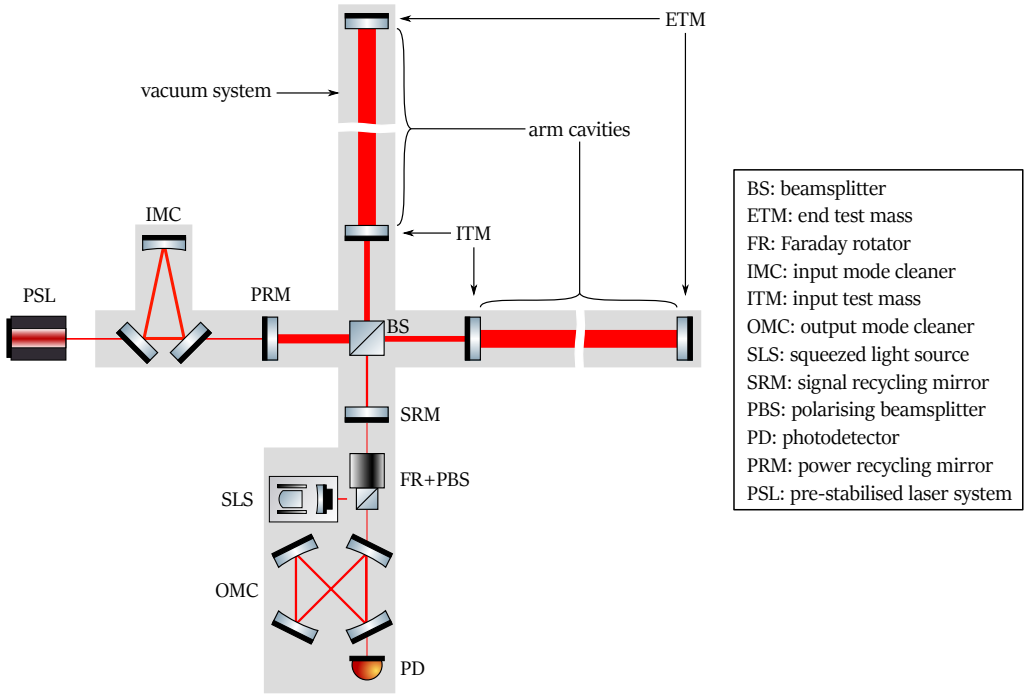

Figure 1.2: Simplified schematic of a gravitational-wave detector with a selection of advanced techniques compared to a basic Michelson interferometer.

process, the circulating optical power reaches the order of 10^5 W. The effective light travel time should, however, also remain small compared to the gravitational-wave period. Otherwise, the accumulated phase shift may decrease again.

During the third joint observation run O3 in 2019 and 2020, the detectors Advanced LIGO, Advanced Virgo, KAGRA and GEO600 [KAG22] employed the direct readout scheme where the interference of the beams which return from the arms is stabilised close to the point of zero output power (small offset from the *dark fringe*). The static output field serves as a local oscillator which beats with the signal field for amplification. If only a small fraction of the input laser power leaks through at the output, the major fraction is effectively reflected back towards the laser source. Placing a partially transmissive power recycling mirror (PRM) in the input can then form a cavity with the mostly reflecting interferometer, increase the input power that impinges on the beamsplitter and optimise the impedance matching of the input laser to the interferometer by adjusting the power recycling transmissivity to the interferometer losses [Adh14].

A similar method is employed in the output. Here, a partially transmissive mirror (SRM) forms a signal recycling or extraction cavity with the interferometer. With this cavity, the peak sensitivity of the detector can either be increased by resonantly enhancing the signal sidebands at the cost of a narrower bandwidth, or the opposite effect can be obtained by extracting the signal sidebands, thereby virtually increasing the linewidth of the high-finesse arm cavities [Miz+93; Gra+98]. The detectors can switch between these two cases via the tuning of the SRM. With the PRM and the SRM, the Michelson interferometer is referred to as "dual-recycled" [Mal06].

An essential technique that aims at the reduction of quantum noise as discussed in Chapter 3 is the injection of squeezed vacuum states into the interferometer output port. These states are provided by a squeezed light source (SLS) and injected via the combination of a polarising beamsplitter (PBS) and Faraday rotator (FR). Due to

the symmetry of the interferometer, the squeezed field is effectively reflected by the interferometer at the dark fringe and the polarisation rotation from the FR allows the PBS to then transmit the squeezed field together with the signal field towards the output photodetector (PD).

To protect this PD from excess power and reduce the shot noise contribution from radio-frequency control sidebands and unwanted higher-order laser modes, the detector output field is mode-filtered by an output mode cleaner cavity (OMC).

The vacuum system reduces the noise contributions from light that is scattered off gas molecules, from fluctuations in the refractive index due to a fluctuating number of gas molecules in the beams, from the damping of the mirrors by the surrounding residual gas and from acoustic noise.

There are many additional techniques which are not shown or mentioned here like seismic isolation platforms, multiple-stage mirror suspensions as well as a vast number of sensors and electronic feedback control loops. They are implemented to keep the interferometer and cavities at the desired operation points and to tackle the various noise sources which are, for instance, analysed regarding the latest improvements in [Bui+20; Ber+21]: quantum, thermal, seismic, Newtonian gravity gradient, length and alignment control, laser intensity, frequency and beam jitter, scattered light, residual gas and photodetector dark noise. The procedure to get such an advanced detector into operational mode needs up to half an hour in the case of the Advanced LIGO detectors, and the Advanced LIGO and Virgo detectors remained in operational mode for about 75 % of the time during the third joint observation run O3 (for Virgo, this at least holds for the second part O3b) [Bui+20; Ber+21].

While the success of these detectors is already astonishing, there is also always the need—and wish—for further improvements.

1.3 Motivation and goal

The current ground-based gravitational-wave detectors, especially Advanced LIGO and Advanced Virgo, already reach impressive sensitivities that enabled the detection of a total of 94 merger events in three observation runs between 2015 and 2020, including 90 binary black holes, 2 neutron star-black hole systems and 2 binary neutron stars [Nit+21]. This constitutes a huge success in high-precision metrology, leading to new insights into astrophysical processes and fundamental physics by allowing to study the dynamics of massive objects via a completely new messenger channel [Bai+21]. These insights and discoveries include, for instance, the origin of at least some gamma ray bursts, one formation site of the heaviest elements in the Universe, a previously unknown population of heavier stellar-mass black holes and the confirmation of the quasi-normal modes of the final black hole predicted by General Relativity [ET 20]. Nevertheless, these second-generation detectors do not enable the full potential of gravitational-wave astronomy and have, so far, only detected signals from a rather limited subset of possible sources.

While the second generation of gravitational-wave detectors had the goal to simply detect, the third generation aims to *observe* astrophysical processes and to significantly extend both the range of source types and the reach into the cosmos, which also corresponds to an increased reach into the past of our Universe. This will be made possible via an order of magnitude better sensitivity that also covers a wider range of frequencies as shown in Figure 1.3. With the resulting detection rate combined with high signal-to-noise ratios, revolutions in astrophysics, fundamental physics and cosmology may very well be ahead of us. The detection of mergers with

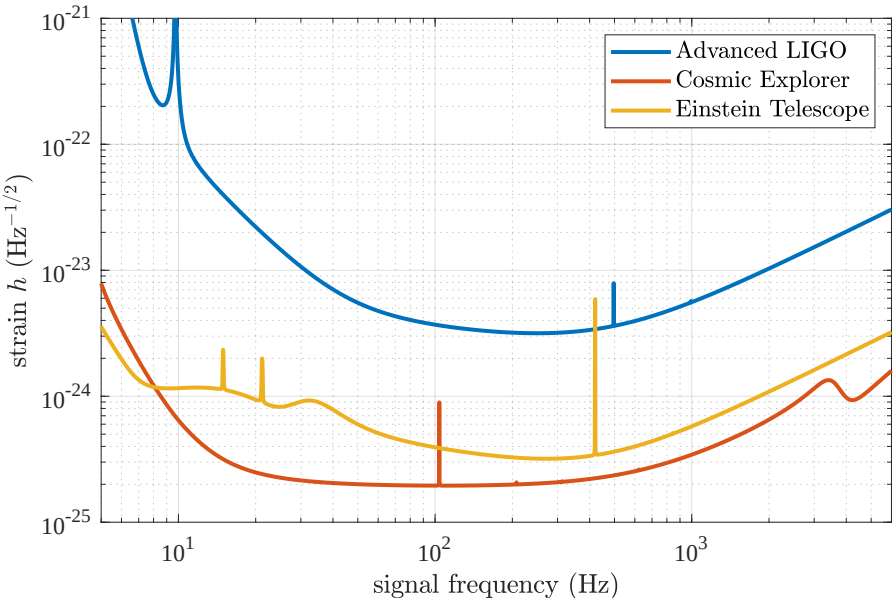

Figure 1.3: Calculated total noise budgets of the current Advanced LIGO detector and the future third-generation detectors Einstein Telescope and Cosmic Explorer which target an increase in the sensitivity of one order of magnitude [Hal; Eur].

a redshift in the order of 10 will allow to analyse how the black hole and neutron star populations evolved over the history of the Universe starting at an age of less than 500 million years [Eva+21]. Improved source localisation for multi-messenger astronomy will reveal how matter behaves under the most extreme conditions including the internal structure and equation of state of neutron stars, heavy element nucleosynthesis and highly relativistic jets. Furthermore, the third detector generation will enable us to study the nature of the strongest gravity with unprecedented fidelity and to test our theories on dark matter and dark energy. Finally, there is also always the possibility of discovering exotic and novel compact objects which are completely unexpected.

Reaching the targeted sensitivities is not a trivial task and requires significant advances in the mitigation of all noise sources, pushing to the limit of what is technically possible. For instance, part of the third-generation designs is an increase in the interferometer arm length to 10 km for the Einstein Telescope and 10 km to 40 km for Cosmic Explorer, the usage of megawatts of optical power for improvements in the high frequency regime and larger and heavier mirrors as well as cryogenic operation for the lower frequency regime [ET 20; Eva+21]. One of the currently dominant noise sources, that limits the second-generation detectors in the frequency range around 100 Hz, is coating Brownian thermal noise originating from the Brownian motion inside the mirror coatings and potentially masking a gravitational wave [Bui+20; Ber+21]. The mitigation of this noise source via improved and new techniques is hence of special relevance. Two examples are the cryogenic operation and the development of coatings with significantly lower mechanical loss. One additional option, that was proposed in the early 2000s, is replacing the currently used fundamental Gaussian laser mode by a higher-order spatial mode to better average over the thermally induced mirror fluctuations [MTV06; Vin10]. This proposal was part of the initial design study of the Einstein Telescope which included the 9th order Laguerre-Gaussian $LG_{3,3}$ mode for the high-frequency interferometer. Due to issues regarding astigmatism, the $LG_{3,3}$ mode was removed from this design study;

nevertheless, higher-order modes are a reasonable and promising candidate for the thermal noise reduction, currently investigated with respect to the much more robust Hermite-Gaussian modes.

In order to justify a design change to higher-order Hermite-Gaussian modes, it has to be thoroughly demonstrated that a gravitational-wave detector can be operated in a higher-order Hermite-Gaussian mode without any significant performance issues, i.e. that these modes are not only beneficial for the coating Brownian thermal noise but effectively for the total noise budget. One crucial aspect in this regard is the quantum noise reduction. The current detectors successfully reduced quantum shot noise by about 3 dB by injecting squeezed vacuum states into the interferometer output port and an effective reduction of quantum shot and radiation pressure noise by 10 dB is targeted for the future detectors. If squeezed states in higher-order spatial modes cannot be generated and applied at this level, which will already be challenging for the fundamental Gaussian mode, the deterioration in the quantum noise reduction could very likely annihilate the thermal noise benefit.

In this thesis, I investigate how squeezed states can be efficiently generated in a selection of higher-order Hermite-Gaussian modes. I furthermore demonstrate that comparable levels of quantum noise reduction as in the fundamental Gaussian mode are feasible in a tabletop Michelson interferometer. This is an essential step in making the case for a thermal noise reduction beyond the current third-generation detector designs via higher-order spatial laser modes.

Furthermore, research into nonclassical states in higher-order spatial modes is relevant for various other optical disciplines. Owing to their different amplitude distributions, these modes e.g. offer an enhancement in the resolution of imaging techniques [UP+13], enable multi-channel quantum communication and sensing [Las+07] and can improve robustness against spatial mismatches [RGR21; Ste+18]. When being limited by quantum noise, these applications naturally benefit from squeezed states. However, the generation of squeezed states in higher-order modes significantly lags behind the fundamental Gaussian mode in terms of the achieved quantum noise reduction. Moreover, to my knowledge, there is no report where squeezed states in higher-order modes were not only generated but also used in an actual measurement application. With this thesis, I also aim to make a contribution to this widely applicable research field.

1.4 Structure of this thesis

The theoretical framework for this thesis is split up into the Chapters 2 and 3.

Chapter 2 addresses thermal noise in gravitational-wave detectors. The origin is explained as well as how the different thermal noise contributions influence the current detector sensitivities. This will justify the different approaches to mitigate thermal noise for the third detector generation which are summarised afterwards. Since the core motivation for this thesis is the thermal noise mitigation via higher-order spatial modes, the idea behind this proposal is described in more detail and higher-order modes are introduced together with the associated challenges and the current resarch status regarding their usage in gravitational-wave detectors.

Quantum noise, as the other main driver for this thesis, is discussed in Chapter 3. How quantum noise influences the sensitivities of gravitational-wave detectors is explained and squeezed states of light are introduced as the most prominent

quantum noise reduction technique. How these states are defined, generated, characterised and applied in the detectors is summarised to provide a background for the subsequent experimental chapters.

The experimental part of this thesis consists of the Chapters 4, 5 and 6.

Chapter 4 combines a detailed numerical analysis of the second harmonic generation of the Laguerre-Gaussian $LG_{3,3}$ mode with a corresponding measurement. This experiment was conducted in light of the former design study of the Einstein Telescope, where the implementation of the $LG_{3,3}$ mode had been part of the high-frequency interferometer. Here, the $LG_{3,3}$ performance in the first nonlinear process employed in every detector's squeezed light source is investigated regarding its conversion efficiency, harmonic output field and sensitivity to astigmatism.

The Chapters 5 and 6 then turn to higher-order Hermite-Gaussian modes which are currently in the focus for the thermal noise mitigation method based on spatial modes. In Chapter 5, the theory on how to efficiently pump a direct higher-order mode squeezing process is introduced. Afterwards, bright squeezed states in the modes $HG_{1,1}$, $HG_{2,2}$ and $HG_{3,3}$ are generated in a type-I optical parametric amplifier and characterised with a balanced homodyne detector. Subsequently, in Chapter 6, these states are applied in a tabletop Michelson interferometer with balanced homodyne readout, which is based on the planned topology for the future gravitational-wave detectors.

Chapter 7 finally provides an overall summary, conclusion and outlook.

The appendix includes Matlab scripts which were used in this thesis.

Chapter 2

Thermal Noise and Higher-Order Spatial Modes

After Chapter 1 reasoned the relevance of future gravitational-wave detectors and their enhanced sensitivities, this chapter will closely discuss one of the limiting noise sources: mirror thermal noise. First, this topic is introduced and the coupling mechanisms are presented. Then, proposed mitigation techniques are outlined with a focus on using higher-order spatial laser modes. This chapter also provides an overview of the current research status on higher-order modes with respect to gravitational-wave detectors.

2.1 Thermal noise in gravitational-wave detectors

There are two main contributions to the overall thermal noise in gravitational-wave detectors: thermal noise related to the test mass substrate and coating (*test mass thermal noise*) and related to the test mass suspension (*suspension thermal noise*). Both contributions affect the effective position of the reflecting mirror surfaces. Hence, they cause fluctuations in the phase of the reflected light and couple to the gravitational-wave readout as noise. Common to both thermal noise sources is also that their origin is associated with channels of energy dissipation according to the fluctuation-dissipation theorem [CW51; Sau90]. A good introduction to thermal noise in gravitational-wave detectors can be found in [Sau94].

Test mass thermal noise causes variations in the effective position of the reflecting mirror surface *relative to its centre of mass* and can be computed as an incoherent sum of thermo-optic [Eva+08] and Brownian noise [Hon+13]. Thermo-optic noise results from temperature fluctuations in the mirror material (coating and/or substrate) leading to thermal expansion and contraction (thermo-elastic noise [LT00; BV03]) and from thermally induced changes in the refractive index (thermo-refractive noise [BGV00]). These two contributions, thermo-elastic and thermo-refractive noise, do not necessarily have to be incoherent. Brownian noise refers to the Brownian motion of the constituent atoms of the mirror material at a given temperature which excite the mirror's elastic modes. Both, thermo-optic and Brownian noise, have to be studied separately for the mirror substrates and coatings. Still, these noises can as well arise due to fluctuations at the interface between the substrate and coating. Suspension thermal noise relates to thermally induced fluctuations in the *position of the centre of mass* of the mirrors. They are especially caused by the fibres of the final mirror suspension stage [Gon00].

As an example, Figure 2.1 shows these different thermal noise contributions in the calculated noise budget of the Advanced LIGO detector. While their specifics

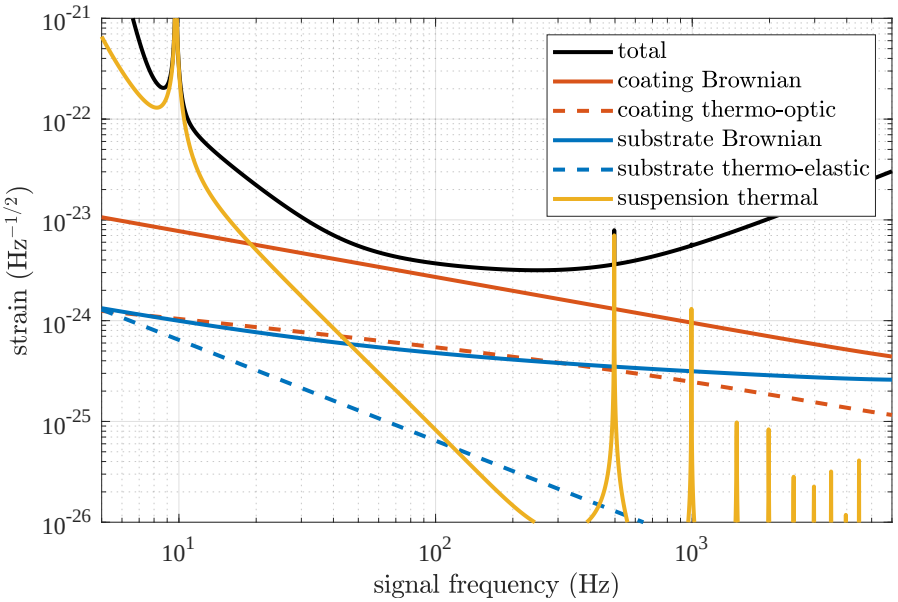

Figure 2.1: Calculated contributions to the thermal noise budget of Advanced LIGO in relation to the total noise budget [Hal].

of course vary among the different gravitational-wave detectors, the following relations apply in general: suspension thermal noise (STN) and test mass thermal noise are relevant below a few tens of Hertz and around 100 Hz, respectively. In the latter case around 100 Hz, the coating Brownian thermal noise (CBTN) has the largest contribution to the test mass thermal noise.

During the third joint observation run, STN was lower than e.g. the alignment and auxiliary length control noise in the Advanced LIGO detectors [Bui+20] and KAGRA [KAG22]. However, STN dominated the noise budget of the Virgo detector below signal frequencies of 30 Hz [Ber+21] and will also have significant contributions in the noise budget of the Einstein Telescope [ET 20]. CBTN dominated the noise budgets of the Advanced LIGO detector in Livingston between 40 Hz to 100 Hz [Bui+20] and of the Virgo detector between 30 Hz to 300 Hz [Ber+21]. The same holds for the design sensitivities of KAGRA [Aku+20] and the Einstein Telescope [ET 20]. For the high power silicon Cosmic Explorer, thermal noise is not expected to be a primarily limiting factor [Eva+21].

General dependences of thermal noise

Before discussing the different approaches to mitigate thermal noise, this paragraph shall briefly introduce how thermal noise can generally be computed based on the fluctuation-dissipation theorem. This theorem relates the near-equilibrium thermal noise power spectral density S_x of a given coordinate x to the rate of dissipation in the system when a generalised force acts directly on x [Hon+13; Gon00; Vin10]

$$S_x(f) = \frac{k_B T}{\pi^2 f^2} \mathrm{Re}\left[Z(f)\right] \ , \tag{2.1}$$

where k_B is the Boltzmann constant, T is the temperature, f is the frequency and $\mathrm{Re}\left[Z(f)\right]$ is the real part of the mechanical impedance Z. In the context of a GW detector, the coordinate x is the position of the reflecting test mass face along the beam propagation axis. Dependent on the different thermal noise contributions,

$\mathrm{Re}\,[Z(f)]$ takes on different forms. For instance, Equation 2.1 transforms into [Vin10]

$$S_x(f) = \frac{4k_B T}{\pi f}\phi U \qquad \text{with} \qquad \mathrm{Re}\,[Z(f)] = 4\pi f \phi U \tag{2.2}$$

for Brownian noise, where ϕ is the mechanical loss angle, which characterises the internal dissipation in the material, and U is the elastic energy stored in the mirror by a static pressure distribution which matches the intensity distribution of the incident readout beam, normalised to a force of 1 N.

Mitigation techniques can then be inferred from the parameters which contribute to S_x for the different thermal noise sources. As a general aspect, which will also be relevant in the following overview, Equations 2.1 and 2.2 reveal that the temperature as well as the mechanical properties of the used coating, substrate and suspension materials have to be taken into account.

2.2 Overview of mitigation techniques for thermal noise

Cryogenic temperatures

Most intuitively and also confirmed by Equation 2.1, thermal noise can be reduced by cooling the optics and suspension to cryogenic temperatures. However, this statement does not hold under all circumstances due to the temperature-dependent material properties of the mirrors, i.e. their mechanical impedance and loss angle. The mirror substrates of all current room-temperature detectors are made of fused silica not only for its outstanding optical properties but also for its very low Brownian noise at room temperature [ET 20]. In addition, fused silica allows to design quasi-monolithic suspension fibres based on pulled fused silica for low suspension thermal noise [Pli+98; M. 10]. However, the loss angle of fused silica shows a broad peak below room temperature such that it is not suitable for cryogenic cooling [Adh+20]. In contrast, sapphire and silicon are free of such cryogenic loss peaks and have a higher thermal conductivity at low temperature. For LIGO Voyager and Cosmic Explorer, silicon is planned for a temperature of 123 K, where this material shows a vanishing thermal expansion coefficient and, thus, no thermo-elastic noise [McG+78]. For the Einstein Telescope's low-frequency interferometer, silicon is planned for a temperature of 10 K to 20 K. KAGRA already uses sapphire mirrors [KAG22] and finally plans for an operating temperature of 20 K. The same material considerations apply to the suspension fibres.

The change to silicon, in turn, requires to operate at another wavelength because silicon is opaque at 1064 nm. While LIGO Voyager and Cosmic Explorer aim for 2 µm, the Einstein Telescope plans for 1550 nm. Hence, the corresponding laser development has to advance (see e.g. [MW22]). Other challenges of cryogenic operation are to simultaneously ensure the mechanical isolation of and an efficient thermal cooling link for the test mass, to decouple the payload from the vibrations of the refrigeration, and to perform maintenance without accessing the cryostat [ET 20].

Despite these challenges, KAGRA is the first kilometre-scale detector to successfully operate at cryogenic temperatures [Aku+19]. In 2018, one sapphire mirror was cooled down to 20 K within 35 days and remained at this level for 10 days. Still, KAGRA operated at room temperature during the third observation run because the thermal noise does not yet limit its sensitivity [KAG22] and KAGRA also experienced issues with ice layers on the mirror surfaces in 2019 [Aku+21]. Hence,

an actual reduction of a kilometre-scale GW detector's noise budget via cryogenic cooling has yet to be demonstrated (compare, however, with [Uch+12]).

Coating materials

[Ste18] provides an overview of different approaches for coating improvements. In this article, Equation 2.1 takes the form

$$S_x(f) = \frac{2k_B T}{\pi^2 f Y_{\text{sub}}} \frac{\delta_c}{w^2} \left(\frac{Y_{\text{coat}}}{Y_{\text{sub}}} \phi_{\parallel} + \frac{Y_{\text{sub}}}{Y_{\text{coat}}} \phi_{\perp} \right) \tag{2.3}$$

for coating Brownian thermal noise, where $Y_{\text{sub/coat}}$ is Young's modulus of the substrate and coating materials, δ_c is the coating thickness, w is the radius of the incident laser beam, assumed in the fundamental Gaussian laser mode, and $\phi_{\parallel}$ and $\phi_{\perp}$ are the mechanical loss angles of the coating parallel and perpendicular to the coating layers, respectively. This model can further be decomposed into the shear and bulk motion of the coating material which, however, only results in small correction factors [Abe+18].

Highly reflective coatings as currently used in gravitational-wave detectors consist of alternating layers of two materials with different refractive indices and the coating thickness depends on both the required reflectivity and the refractive indices of the used materials. The feasible variations in the thickness δ_c have a relatively small effect on the thermal noise compared to the mechanical loss angles [Ste18].

A significant research focus is on understanding how the atomic-scale mechanisms of a material, e.g. the medium-range atomic ordering, relate to its mechanical loss [Har+16] and computational models have started to agree well with experimental data [Tri+16]. Developing coatings with sufficiently low mechanical loss is crucial to reach the design sensitivities of the future detectors and the operating temperature has to be taken account in the same manner as for the mirror substrate material. Furthermore, matching the coating's to the substrate's Young's moduli generally results in the lowest coating thermal noise [RM16].

Another important aspect is the optical absorption of the highly-reflective coating (and substrate) which has to satisfy stringent requirements in the order of ppm [ET 20]. Optical absorption has to be minimised to keep the test masses at low temperature for cryogenic operation and to avoid thermal-lensing induced beam distortions.

The current detectors run with coating layers made of fused silica (Si:O_2) and tantalum pentoxide doped with titanium dioxide (Ti:Ta_2O_5). They are produced via ion beam sputtering. An overview of the alternatives amorphous silicon, silicon nitride, silica-doped hafnia, alumina, multi-material, nano-layer and crystalline coatings as well as of the ongoing research on their properties in relation to the production method can be found e.g. in [Ste18; ET 20].

Khalili cavities or etalons

The proposal to use Khalili cavities or etalons is based on the dependence of the coating thermal noise on the coating thickness and thus the number of coating layers due to the requirement of high reflectivity. In gravitational-wave detectors, the end test masses show the highest number of coating layers. Hence, replacing them by an anti-resonant linear cavity, such that most of the light only senses the first cavity mirror, could reduce the thermal noise because this first mirror can have a significantly smaller number of coating layers [Kha05]. An alternative which requires less

hardware are Khalili etalons [Gur+11]. The Hannover 10 m prototype plans to test Khalili cavities and to stabilise them to the anti-resonance condition via the injection of an offset phase-locked sub-carrier beam from the rear side [Goß+10]. However, this technique is not mentioned in [ET 20; Eva+21; Adh+20].

All-reflective interferometers

Issues related to combining high laser power with transmissive optics like the input test masses (see Fig. 1.2) are the optical absorption and, thus, thermal lensing due to thermo-elastic and thermo-refractive effects. In addition, the realisation of a cryogenic operation becomes more difficult with increasing absorption as well. One way to avoid these challenges is to replace transmissive cavities by diffractive grating cavities and to design an all-reflective interferometer [Dre96]. In 2000, a zero-area polarisation Sagnac interferometer which used a diffractive grating as a polarisation beam splitter was demonstrated [Tra+00]. However, additional phase noise from lateral grating displacements was encountered for this approach in [Hal+09]. Neither of the third-generation detectors currently aims to implement an all-reflective topology.

Larger beam radius and higher-order spatial modes

The power spectral density of the coating thermal noise in Equation 2.3 scales inversely with the square of the beam radius because a more uniform intensity distribution of the incident beam can better average over the thermal noise fluctuations. As an example, the Einstein Telescope aims for beam radii of 9 cm and 12 cm on the end mirrors of the low- and high-frequency interferometers, respectively. To reduce clipping losses to a negligible level, the mirror substrates then need to have a diameter of 45 cm and 62 cm, respectively.

Above, the laser beam which propgates through the interferometer was only considered to be in the fundamental Gaussian laser mode $\mathrm{TEM}_{0,0}$. However, based on Levin's analysis of the internal thermal noise in [Lev98], Vinet studied the impact of using arbitrary higher-order Hermite-Gaussian (HG) and Laguerre-Gaussian (LG) modes instead of the $\mathrm{TEM}_{0,0}$ mode [Vin10]. These modes show a more uniform intensity distribution than the fundamental mode and, thus, promise to average even better over the thermal noise fluctuations. This option, as the core motivation for this thesis, is outlined in more detail in the next section. Furthermore, higher-order modes lead to a more uniform optical absorption in the mirrors which is beneficial with respect to thermal lensing and thermal distortion [Vin09].

Before analysing LG and HG modes, it is worth mentioning that flat-top or mesa beams were first proposed for the thermal noise reduction in gravitational-wave detectors. They would, however, require non-spherical mirrors instead of the spherical ones which are used in the current detectors, planned for the third generation and compatible with LG and HG modes. Even though there has been research on these beams, e.g. [D'A03; Tar+07; Vin09], implementing flat-top beams into existing or future detectors thus implies significantly more effort compared to higher-order LG or HG modes and this thesis will not further consider flat-top beams.

2.3 Higher-order spatial laser modes

2.3.1 The Laguerre-Gaussian and Hermite-Gaussian mode basis

The wave-like nature of laser beams can be described by the differential paraxial Helmholtz equation (PHE) which allows to derive exact solutions in the form of complete, orthonormal sets of transverse spatial modes. In practice, most laser beams justify a description via the *paraxial approximation* [Sie86] and any such free-space beam can then be decomposed in the basis of any of these orthonormal sets. The two relevant bases for this thesis are the helical Laguerre-Gaussian (LG) and Hermite-Gaussian (HG), which are characterised by a cylindrical and rectangular symmetry, respectively.

The complete, normalised amplitude distribution of the helical LG modes in cylindrical coordinates ($\mathbf{r} = (r, \varphi, z)$, z defines the propagation axis) reads [Sie86; Ful+10]

$$\begin{aligned} \mathrm{LG}_{p,l}(\mathbf{r},t) &= A_{p,l}(\mathbf{r}) \times e^{i(kz-\omega t+\beta)} \\ &= \frac{1}{w(z)}\sqrt{\frac{2p!}{\pi(p+|l|)!}}\left(\frac{\sqrt{2}r}{w(z)}\right)^{|l|} L_p^{|l|}\left(\frac{2r^2}{w^2(z)}\right)\exp\left(-ik\frac{r^2}{2q(z)}+il\varphi\right) \\ &\quad\times\exp\left[i(2p+|l|+1)\Psi(z)\right]\exp\left[i(kz-\omega t+\beta)\right] \\ \text{with}\qquad &\int\left|\mathrm{LG}_{p,l}(\mathbf{r},t)\right|^2\,dA = 1\,, \end{aligned} \tag{2.4}$$

where the last line is an integral over the transverse plane and defines "normalised". $A_{p,l}$ is the complex transverse amplitude distribution and actual solution to the PHE, and $e^{i(kz-\omega t+\beta)}$ is a global phase term which is separated from $A_{p,l}$ before the PHE is solved. Further, $w(z)$ is the beam radius, $0 \leq p \in \mathbb{N}$ is the radial and $l \in \mathbb{Z}$ is the azimuthal mode index, $L_p^{|l|}$ is the generalised Laguerre polynomial, $\Psi(z) = \mathrm{atan}(z/z_R)$ multiplied with $2p+|l|+1$ is the Gouy phase with the Rayleigh range $z_R = n\pi w_0^2/\lambda$ (n: refractive index, w_0: waist size, λ: wavelength), $q(z) = z + iz_R$ is the complex beam parameter, $k = 2\pi n/\lambda$ is the wavenumber, ω is the angular optical frequency and β is a constant phase term. The mode order of an LG mode is $g_{p,l} = 2p + |l|$ and the waist position is at $z = 0$.

The complete, normalised amplitude distribution of the HG modes in Cartesian coordinates ($\mathbf{r} = (x, y, z)$, z again defines the propagation axis) reads [Sie86]

$$\begin{aligned} \mathrm{HG}_{m,n}(\mathbf{r},t) &= A_{m,n}(\mathbf{r}) \times e^{i(kz-\omega t+\beta)} \\ &= \frac{1}{w(z)}\sqrt{\frac{2}{2^{m+n}\pi m!n!}}\,H_m\left(\frac{\sqrt{2}x}{w(z)}\right)H_n\left(\frac{\sqrt{2}y}{w(z)}\right)\exp\left(\frac{-r^2}{w^2(z)}\right) \\ &\quad\times\exp\left(-i\frac{kr^2}{2R(z)}\right)\exp\left[i(m+n+1)\Psi(z)\right]\exp\left[i(kz-\omega t+\beta)\right] \end{aligned} \tag{2.5}$$

where $r = \sqrt{x^2+y^2}$, H_m and H_n are the Hermite polynomials and $R(z) = z[1+(z_R/z)^2]$ is the radius of curvature of the wave fronts at plane z. The other quantities as well as the normalisation are defined as for the LG mode and the mode order of an HG mode is $g_{m,n} = m + n$ with the mode indices $0 \leq m, n \in \mathbb{N}$.

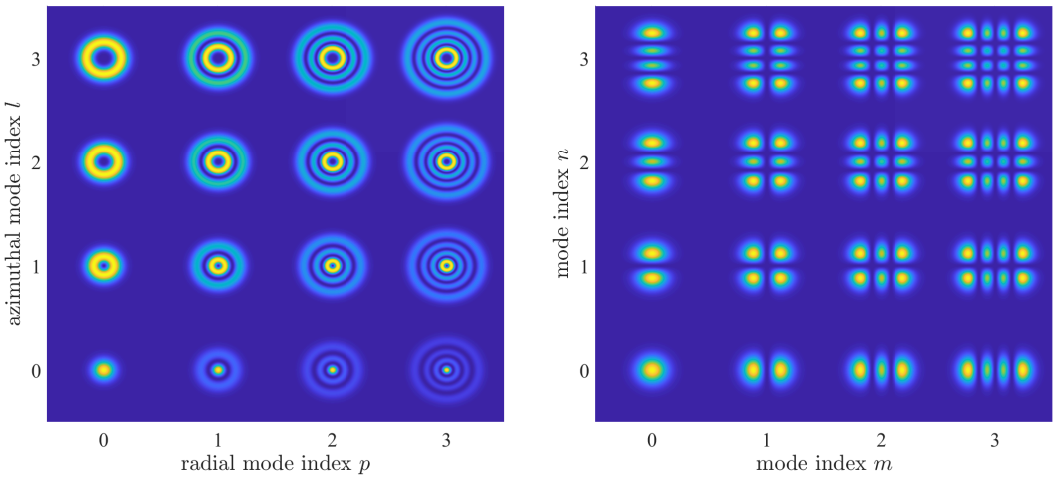

Figure 2.2: Selection of low-order cylindrically symmetric helical LG modes (left) and rectangularly symmetric HG modes (right). Shown are the intensity distributions over the transverse plane. The displayed mode orders are not identical because $g_{p,l} \neq g_{m,n}$ for $p = m$ and $l = n$. A laser beam can fully be described as a superposition of these modes, respectively, if all of the infinitely many LG or HG modes are included.

The intensity distributions (absolute value squared of the amplitude distributions) of some low-order LG and HG modes over the transverse plane are shown in Figure 2.2 for comparison. Furthermore, $\mathrm{LG}_{0,0} = \mathrm{HG}_{0,0} = \mathrm{TEM}_{0,0}$.

2.3.2 Higher-order modes for thermal noise mitigation

Higher-order LG modes were proposed for the thermal noise mitigation in gravitational-wave detectors as an alternative to flat-top beams for their compatibility with the existing spherical mirror geometry [MTV06]. Vinet then analysed the effect of arbitrary LG and HG modes on the thermal noise separately for substrate Brownian, substrate thermo-elastic, coating Brownian and coating thermo-elastic noise. Here, I will only outline Vinet's analysis for the coating Brownian noise as it most likely will constitute the largest contribution to the total test mass thermal noise in the frequency range where the test mass thermal noise significantly limits the detector sensitivities. Please note that Vinet only considered infinite mirror sizes in [Vin10] which is, however, sufficient for the basic idea. Further readings for finite mirrors or even arbitrarily shaped mirrors under symmetrical and non-symmetrical illumination are e.g. [BHV98; Dic21]. Furthermore, the considered frequency range is assumed to be sufficiently far from mechanical resonances.

Vinet uses Equation 2.2 in the form

$$S_x(f) = \frac{4k_\mathrm{B}T}{\pi f} U_c \phi_c \tag{2.6}$$

for the coating Brownian thermal noise where the subscript c now indicates that these are the coating parameters. The same equation also holds for the substrate Brownian thermal noise with the respective parameters. The dependence of the coating Brownian thermal noise on the intensity distribution of the incident beam is included in U_c.

Hermite-Gaussian modes

For Hermite-Gaussian modes, it is [Vin10]

$$U_c(m,n) = \delta_c \frac{(1+\sigma)(1-2\sigma)}{Y_{\text{coat}}} \Omega_1 \bar{\omega}_1(m,n) \tag{2.7}$$

where m, n are the mode indices, δ_c is again the coating thickness, σ is the Poisson ratio, Y_{coat} is the coating's Young's modulus, Ω_1 depends on the elastic constants of the material, which is, for instance, 1 if the coating's and substrate's constants are identical, and

$$\bar{\omega}_1(m,n) = \int_{\mathbb{R}^2} dpdq \tilde{I}^2_{m,n}(p,q) = \frac{\pi}{w^2} \bar{g}_{m,n} \,. \tag{2.8}$$

Here, p and q are the coordinates for the Fourier transform of the intensity distribution $\tilde{I}_{m,n}$ of the $\text{HG}_{m,n}$ mode. The right-hand side shows the same dependence on $1/w^2$ as in Equation 2.3 and $\bar{g}_{m,n}$ is a relative factor which is 1 for the $\text{TEM}_{0,0}$ mode and < 1 for the higher-order HG modes.

Laguerre-Gaussian modes

For Laguerre-Gaussian modes, the equation is more difficult, especially because Vinet does not only consider helical LG modes such that the intensity distribution does depend on φ in contrast to Figure 2.2. While the intensity distribution of the HG modes is given by the product of the x and y terms, the one for the general LG modes is given by the sum of an axially symmetric term and one with an angular parity of $\cos 2n\varphi$. This leads to a costlier calculation; however, finally, the result is similar to the HG case: it scales with $1/w^2$ and includes a relative factor $\bar{g}_{p,l}$ which is 1 for the $\text{TEM}_{0,0}$ and < 1 for the higher-order LG modes.

Comparison of Hermite-Gaussian and Laguerre-Gaussian modes

For a fair comparison of higher-order modes to the $\text{TEM}_{0,0}$ mode, the respective beam sizes on a mirror have to be adjusted such that they yield the same clipping loss. A typically assumed value for the clipping loss is 1 ppm. Under this assupmtion, Figure 2.3 examplifies that the intensities of the $\text{LG}_{3,3}$ and $\text{HG}_{4,4}$ mode are more uniformly distributed over a circular mirror than the intensity of the $\text{TEM}_{0,0}$ mode. The ratios of the beam sizes are roughly $w_{3,3}/w_{0,0} \approx w_{4,4}/w_{0,0} \approx 0.6$. The example also shows that the intensity of an LG mode is, in general, more homogenously distributed over the circular mirror surface than the intensity of a HG mode. Hence, the thermal noise mitigation factors are better for LG modes at comparable mode order. The opposite would apply for rectangular mirrors [Ful12].

The improvement factors for the power spectral density S_x of the coating Brownian thermal noise of higher-order LG and HG modes, assuming the same clipping loss, are given in Table 2.1. They confirm that LG modes are more effective for a given mode order; the $\text{LG}_{3,3}$ and $\text{HG}_{4,4}$ mode e.g. have factors of 2.65 and 1.47, respectively. The scaling factors for the other thermal noise contributions can be looked up in [Ful12].

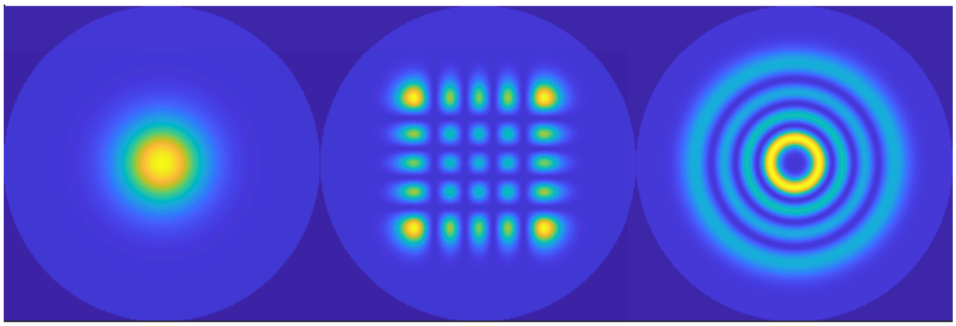

Figure 2.3: The $TEM_{0,0}$ (left), $HG_{4,4}$ (middle) and helical $LG_{3,3}$ (right) mode on a circular mirror (brighter background) for the same clipping loss of 1 ppm.

l p	0	1	2	3	4
0	1.00	1.40	1.61	1.69	1.78
1	1.66	1.99	2.17	2.22	2.30
2	1.90	2.23	2.42	2.47	2.47
3	2.09	2.44	2.52	2.65	2.74
4	2.18	2.50	2.68	2.70	2.84

m n	0	1	2	3	4
0	1.00	1.10	1.11	1.08	1.05
1	1.10	1.29	1.33	1.40	1.30
2	1.10	1.33	1.40	1.41	1.41
3	1.08	1.32	1.41	1.44	1.45
4	1.05	1.30	1.41	1.45	1.47

Table 2.1: Improvement factors for the power spectral density S_x of coating Brownian thermal noise of higher-order LG (left) and HG (right) modes, assuming identical clipping losses on a circular mirror [Ful12].

2.3.3 Current research status on higher-order spatial modes

Higher-order mode generation with a phase plate

In the research for gravitational-wave detectors, higher-order modes are usually generated by shining the $TEM_{0,0}$ mode onto a phase plate. A phase plate is a grid of finitely sized pixels each of which has an individual optical path length. This can either be a transmissive or reflective optic. Both types have in common that they modulate the transverse phase distribution of the incoming beam while, in general, leaving the intensity distribution unaffected. If the incoming beam is in the $TEM_{0,0}$ mode with a waist of w_{in} and a higher-order mode with a waist of w_{out} shall be generated, the phase plate can be used to transform the $TEM_{0,0}$ mode's phase distribution $\Theta_{0,0}$ into the one of the intended mode $\Theta_{m,n}$. The phase plate is usually placed at the waist position of the incoming beam because $\Theta_{0,0}(x, y, z = 0, w_{\text{in}}) = \text{const}$. In this case, the optical path length distribution of the phase plate can simply be set equal to $\Theta_{m,n}$. The resulting field A_{res} directly after the phase plate is then given by

$$\begin{aligned} &A_{\text{res}}(x, y, 0, w_{\text{in}}, w_{\text{out}}) \propto I_{0,0}(x, y, 0, w_{\text{in}})\Theta_{m,n}(x, y, 0, w_{\text{out}}) \\ &\text{with} \quad \int I_{0,0}(x, y, z, w_{\text{in}})\, dxdy = 1\,, \end{aligned} \tag{2.9}$$

where $I_{0,0}$ is the normalised intensity distribution of the $TEM_{0,0}$ mode. Neglecting absorption losses or technical imperfections, the conversion efficiency can be derived as the spatial overlap of A_{res} to the intended mode $A_{m,n}$, that is, as the mode purity

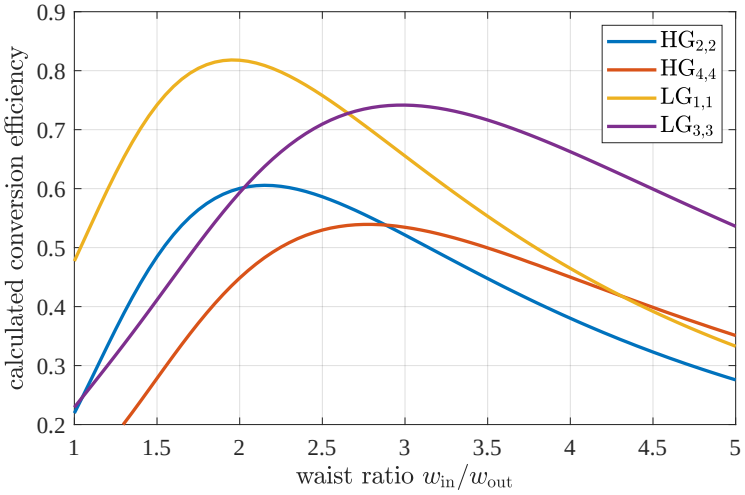

Figure 2.4: Calculated conversion efficiency of a phase plate from the TEM$_{0,0}$ mode into two LG and two HG modes of comparable mode order, respectively, dependent on the waist size ratio of the incoming and outgoing beams. The phase plate is assumed to be at the waist position ($z = 0$).

of A_{res} with respect to $A_{m,n}$:

$$\eta_{\mathrm{conv}}(w_{\mathrm{in}}, w_{\mathrm{out}}) = \left| \int A^*_{m,n}(x, y, 0, w_{\mathrm{out}}) A_{\mathrm{res}}(x, y, 0, w_{\mathrm{in}}, w_{\mathrm{out}})\, dxdy \right|^2 , \tag{2.10}$$

assuming the fields are normalised. In this equation, both fields have the same phase distribution and the conversion efficiency only depends on the overlap of the intensity distributions which, in turn, depends on the ratio of the waist sizes of the incoming and outgoing beam, $w_{\mathrm{in}}/w_{\mathrm{out}}$, as shown in Figure 2.4. Let us assume that the TEM$_{0,0}$ shall be converted into the LG$_{3,3}$ mode. If the waist of the incoming beam is too small compared to the waist which the phase plate is set to generate, not enough of the TEM$_{0,0}$ power gets into the outer LG$_{3,3}$ ring (compare with Fig. 2.3). On the other hand, if the incoming waist is too large compared to the generated waist, not enough power remains in the centre for the most intense inner ring and, in an extreme case, too much power is lost in the region outside the outer ring. The same consideration applies to HG modes which have the additional disadvantage that their rectangular intensity shape matches the round shape of the TEM$_{0,0}$ mode fundamentally less. Furthermore, the maximally achievable conversion efficiency decreases with the mode order because the intensity distributions of higher-order modes differ evermore from the TEM$_{0,0}$ distribution.

In addition, a contoured blazed grating can be added to the phase distribution that the phase plate generates to spatially separate the modulated from the unmodulated light and, at the same time, achieve some amplitude modulation, as well [Ful12]. Theoretically, conversion efficiencies of up to 100 % are possible with this method; however, this is unlikely to be achieved in reality due to technical limitations. The conversion efficiency can also be increased up to almost 100 % by using two subsequent phase plates [Jes+08]. To my knowledge, the highest conversion efficiencies were achieved with two phase plates and amounted to 61 % to 75 % for the HG$_{1-5,0}$ and LG$_{3,3}$ mode [Ma+20]. Absorption and an imperfect diffraction efficiency mainly limited these results. In this thesis, one computer-controlled spatial light modulator (SLM), type LCOS-Hamamatsu, without a blazed grating generates

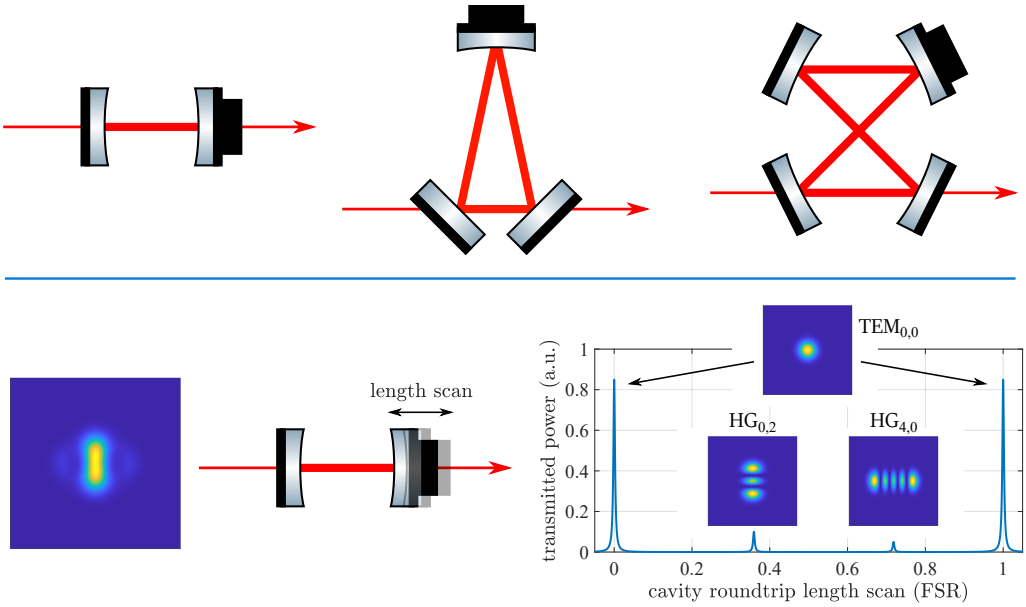

Figure 2.5: Top: typical geometries of optical cavities: linear (left), triangular (middle) and bow-tie (right). A piezo-electric transducer is attached to one mirror per cavity to control the cavity length. Bottom: an impure beam is injected into a linear cavity consisting of 85 % $TEM_{0,0}$, 10 % $HG_{0,2}$ and 5 % $HG_{4,0}$ with respect to the cavity eigenbasis. This mode composition can be analysed by scanning the cavity length and measuring the transmitted power where each injected mode relates to an individual peak of corresponding height, if the mode resonances are non-degenerate. If the cavity length is stabilised to one of the resonance conditions, the transmitted field only consists of the corresponding mode to a typically very good approximation. FSR: free spectral range (here, = wavelength).

the higher-order HG modes (see also Appendix A.2) and a diffractive optical element from Jenoptik with a blazed grating generates the $LG_{3,3}$ mode.

Mode cleaning, mode purity and mode conversion efficiency

Even for a mode conversion efficiency of 75 % of a phase plate, 25 % of the outgoing laser beam are in unwanted modes. To filter them out, an optical cavity can be used. Typically, such a cavity is arranged with two (linear), three (triangular) or four (bow-tie) mirrors (see Fig. 2.5). For mode cleaning, the laser beam is coupled into the cavity via an incoupling mirror, which shows a corresponding transmissivity, and gets reflected back and forth by the cavity mirrors. The radii of curvature of the mirrors and their distances define a waist position and size such that the modes of a basis with these waist parameters will repeat their shape after each roundtrip. These are the eigenmodes of the cavity; for instance, the LG and HG modes. The incoupled laser beam can then be decomposed into these eigenmodes.

If a piezo-electric transducer is attached to one of the cavity mirrors, the cavity roundtrip length can be adjusted with high precision, i.e. with a resolution significantly below the laser's wavelength. If an eigenmode accumulates a phase of an integer multiple of 2π during one roundtrip for a given cavity length, it will interfere constructively with light that is injected into the cavity and coupled to the same eigenmode. This mode will, thus, be resonantly enhanced and have a maximum in the transmitted power at this cavity length. Especially since the Gouy phase depends on the mode, different eigenmodes experience this resonance condition at

different cavity lengths, that is, they are non-degenerate. If an eigenmode is not resonantly enhanced, its transmitted power is typically negligible. Hence, a cavity can be used to analyse the mode content of a laser beam: if the cavity length is scanned, the peaks in the transmitted power correspond to the mode decomposition of the injected laser beam in the cavity eigenbasis [KW08] (see Fig. 2.5). Furthermore, if the cavity length is stabilised to the resonance condition of an intended mode, other modes will have a negligible contribution in the transmitted field, assuming they are non-degenerate with the intended mode, such that the mode purity of the laser beam can be significantly increased in transmission of a cavity. For this reason, such a cavity is also referred to as *mode cleaner*.

The input mode cleaners of gravitational-wave detectors have the triangular geometry, while the output mode cleaners have the bow-tie one. Unfortunately, helical LG modes are not compatible with either design. A cavity with an odd number of mirrors requires a symmetry around the vertical axis which the phase distributions of helical LG modes generally do not exhibit, and the bow-tie cavity causes problems due to an inherent astigmatism (discussed below). Alternatives are linear and non-planar four-mirror cavites. With the linear design, a mode purity for the $LG_{3,3}$ mode of up to 99 % was reported in [Ful+10] and up to 97 % in [Car+13]. In the latter article, a conversion efficiency of 59 % from a $TEM_{0,0}$ into a 83 W $LG_{3,3}$ mode was demonstrated with a transmissive diffractive optical element. In [NBW17], a four-mirror cavity avoided the bow-tie astigmatism by going out of the plane with one of the mirrors. $LG_{3,3}$ mode purites of 98 % to 94 % were achieved for 10 W to 80 W of optical power being injected into this cavity.

In contrast to LG modes, HG modes can resonate in triangular and bow-tie cavities. In [Ast+21], higher-order HG modes up to a mode order of 30 were generated with a reflective spatial light modulator and an input power of up to 1 W, cleaned with a linear cavity and analysed with a triangular one. While the achieved mode purity for the $HG_{5,5}$ reached 96 %, the conversion efficiency was relatively low with only 6.6 %. These values decreased for the $HG_{15,15}$ mode down to a purity of 78 % and an efficiency of 1.7 %. This article also presents a method to genereate LG modes from HG modes via non-tilted cylindrical lenses.

In this thesis, a linear cavity (see Fig. 2.7) was chosen as a mode cleaner for the $LG_{3,3}$ experiments since it is easier to implement than a non-planar four-mirror cavity. For the HG experiments, a triangular cavity was finally chosen (see also end of next section). The power-wise conversion efficiencies (ratio of optical power upstream the phase plate and downstream the mode cleaner) were measured to be about 45 % ($LG_{3,3}$) and 29 % ($HG_{4,4}$, exemplary).

Astigmatism and mode-degeneracy

Non-cylindrically symmetric optics or optical systems as described below are called astigmatic. An optical cavity, for instance, with such a geometry favours the HG over the LG modes because the former are symmetric with respect to the vertical axis while the latter are not. The basic mechanism is as follows: since the LG and HG mode bases are both complete, any LG mode can be decomposed into the HG modes of identical mode order. A symbolic example is [HVW20a]

$$\mathrm{LG}_{3,3} = \sum_{k=0}^{9} c_{k,9-k}\mathrm{HG}_{k,9-k} \qquad \text{with} \qquad \sum_{k=0}^{9} |c_{k,9-k}|^2 = 1\,, \tag{2.11}$$

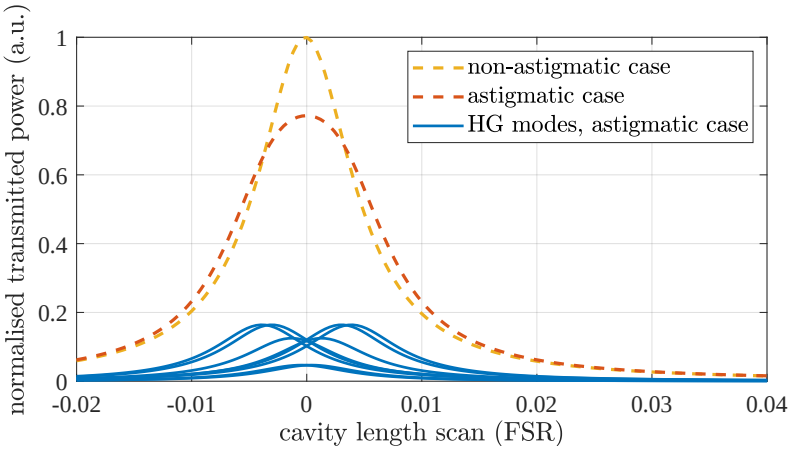

Figure 2.6: Power P_{trans} transmitted through a cavity, if an $\text{LG}_{3,3}$ mode is injected, dependent on the cavity length for the astigmatic and non-astigmatic case (based on [HVW20a]). The curves are normalised to the non-astigmatic case. FSR: free-spectral range.

where $c_{k,9-k}$ are complex coefficients. Let us assume that the $\text{LG}_{3,3}$ mode is injected into a linear cavity with one plane mirror (radius of curvature $R_{c1} = \infty$) and one mirror with different radii of curvature along the x and y axis, $R_{c2,x}$ and $R_{c2,y}$ such that the cylindrically symmetry is broken. Each of these HG modes can now be assumed to experience an individual effective radius of curvature

$$R_{c2}(m,n) = \frac{mR_{c2,x} + nR_{c2,y}}{g_{m,n}} \tag{2.12}$$

because the mode indices indicate how the intensity of the $\text{HG}_{m,n}$ mode is distributed between the x and y axis. The roundtrip Gouy phase $\xi^{\text{rt}}_{m,n}$ is then [Ara13]

$$\xi^{\text{rt}}_{m,n} = 2\arccos\left[\text{sign}(g_1) \times \sqrt{g_1 g_2(m,n)}\right] \tag{2.13}$$

where $g_1 = 1 - L/R_{c1}$ and $g_2(m,n) = 1 - L/R_{c2}(m,n)$ with the cavity length L. Hence, the HG modes of the same mode order experience different roundtrip Gouy phases and will, thus, satisfy the resonance condition at slightly different cavity lengths. The normalised transmitted power of this cavity reads [Kwe+07]

$$P_{\text{trans}}(L) = \sum_{k=0}^{9} \frac{P_{k,9-k}}{1 + \left(\frac{2\mathcal{F}}{\pi}\right)^2 \sin^2\left(\frac{-\pi L}{\lambda} + 5\,\xi^{\text{rt}}_{k,9-k}\right)}\,, \tag{2.14}$$

assuming that the injected HG modes are perfectly matched to their respective cavity eigenmodes. $P_{k,9-k} = |c_{k,9-k}|^2$, $\mathcal{F}$ is the cavity finesse and λ is the wavelength.

The consequence of this kind of astigmatism is illustrated in Figure 2.6. The normalised yellow dashed line represents the case of no astigmatism with $R_{c2,x} = R_{c2,y} = 50\,\text{cm}$, $L = 20\,\text{cm}$ and $\mathcal{F} = 200$ where the 9th order HG modes are perfectly degenerate and maximally add up. In the astigmatic example with $R_{c2,y} = 50.15\,\text{cm}$, these HG modes shown in blue have drifted so much apart that they only add up to a maximum transmitted power of about 0.77. This can be interpreted as a reduction in the effective mode-matching of the $\text{LG}_{3,3}$ to the cavity by about 23 % caused by a distortion of the LG cavity eigenmodes. Hence, if the cavity

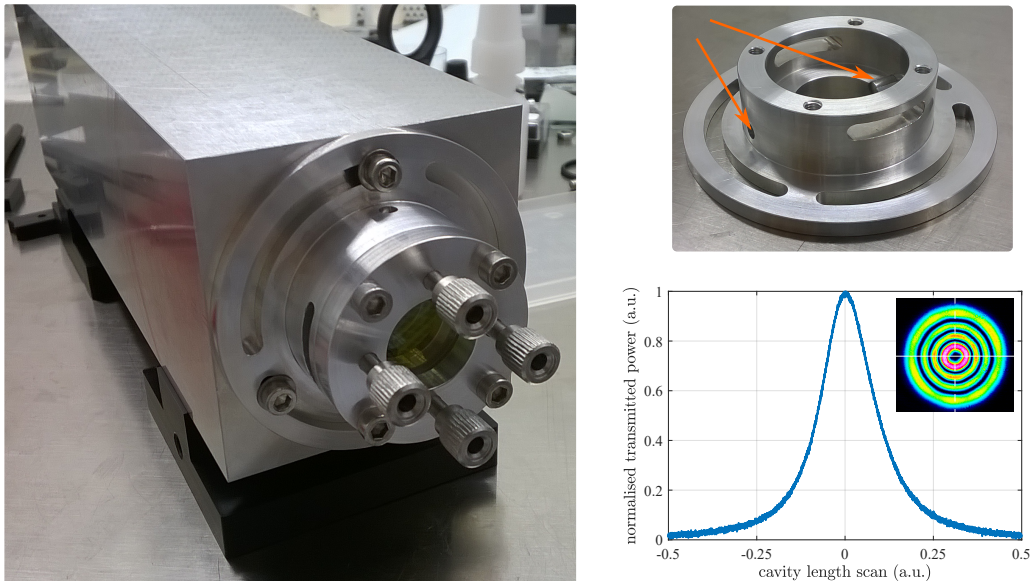

Figure 2.7: Left: linear cavity, which is formed by an aluminium spacer, for the $LG_{3,3}$ mode cleaning in this thesis. The visible mirror mount allows to bend the mirror around one axis via two of the four fine-adjustment screws which reach out towards the reader. The other two fasten the mirror on two pins pointed at by the arrows on the top right. These two aligned pins define the bending axis. Bottom right: transmitted power of this cavity for an injected $LG_{3,3}$ mode where the cavity length is scanned around the corresponding resonance condition. The CCD (charged coupled device) picture shows the intensity distribution of the transmitted field when the cavity is stabilised to the resonance condition.

is stabilised to the maximum of the transmitted power, 23 % of the injected power will minimally be reflected by the cavity and are unusable for downstream applications. A similar consideration applies to cavity-enhanced nonlinear processes for which the circulating intra-cavity power is relevant. Since this power is proportional to the transmitted power,[1] the maximum circulating power is also reduced by 23 % and less power is available for the nonlinear process. In addition, the cavity resonance length, which corresponds to the maximum of the transmitted/circulating power, does not coincide with the resonance lengths of the individual HG modes. Hence, the HG mode composition at the total maximum differs from the one of the $LG_{3,3}$ mode in the non-astigmatic case such that the mode purity of the circulating and transmitted field with respect to an ideal theoretical $LG_{3,3}$ mode is deteriorated.

In reality, unwanted mirror deformations are much more complex and showed to significantly deteriorate the performance of the $LG_{3,3}$ mode in optical cavities and interferometers [Bon+11; Sor+13; Hon+11; HL18]. For this reason, the $LG_{3,3}$ mode was cancelled from the design study of the Einstein Telescope where it had been planned to be used for the high-frequency interferometer. Also for the $LG_{3,3}$ experiment in Chapter 4, the astigmatism of the linear mode-cleaning cavity had to be reduced. In the end, this worked best with a special mount for one of the two mirrors where two pins define an axis around which the mirror can be bent by applying pressure via two fine-adjustment screws (see Fig. 2.7). Reducing the radius of curvature of the mirror on the proper axes had a significantly beneficial effect on the mode purity of the transmitted beam.

[1] The proportionality factor is the power transmissivity coefficient of the outcoupling mirror.

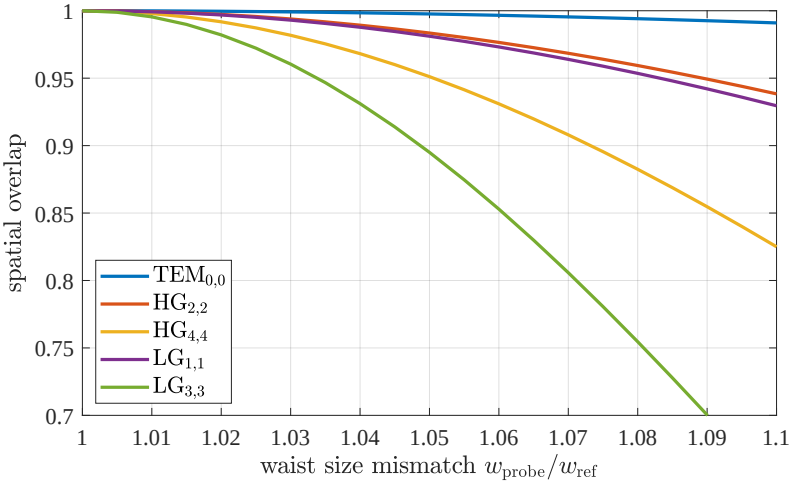

Figure 2.8: Spatial overlap of a probe and reference (ref) beam which are, in general, in the same pure mode indicated in the legend, dependent on a mismatch in the waist sizes. Higher-order modes are increasingly more sensitive to spatial mismatches.

Higher-order HG modes are less sensitive to astigmatism but share the disadvantage with LG modes that modes with equal mode order are degenerate in an (ideal) linear cavity such as the interferometer arm cavities of the gravitational-wave detectors. This simplifies the coupling from the intended higher-order mode into other modes of the same order via mirror imperfections and scattering. This effect can constitute a primary loss source [TGF20]. For higher-order HG modes, astigmatism can then even be beneficial and increase the robustness of the used mode in terms of power loss, mode purity and contrast defects [TGF20].

For the HG experiments in this thesis, it was first planned to employ the linear cavity from Figure 2.7. However, the degeneracy of modes of equal mode order appeared to be an issue for the HG$_{1,1}$ operation. Since no blazed grating was used for the spatial light modulator which generated the HG modes, the generated field co-propagated with the remaining part of the original TEM$_{0,0}$ field. Due to the discrepancy of the incoming TEM$_{0,0}$ and outgoing modulated waist sizes, the mode matching of this TEM$_{0,0}$ field to the linear mode cleaner was relatively low as the mode matching was optimised with respect to the generated HG field. Waist size and position mismatches of the TEM$_{0,0}$ mode, however, couple to the LG$_{1,0}$ mode which is degenerate with the HG$_{1,1}$ mode due to the equal mode order. This effect significantly deteriorated the HG$_{1,1}$ mode purity in transmission of the mode cleaner and the linear cavity was replaced by a triangular mode cleaner which breaks this degeneracy.

Sensitivity to spatial mismatches

Higher-order modes are more sensitive to spatial mismatches (see Fig. 2.8). Let us assume that we have a pure reference mode which can e.g. be the eigenmode of a cavity or the local oscillator field at the output of a gravitational-wave detector. Then, we have a probe laser beam which is, in principle, in the same pure mode. This can e.g. be the beam we want to inject into the cavity or the signal field of the detector. Now, we want to spatially match this probe beam to the reference. Theoretically, a spatial overlap of 100 % can be achieved for any spatial mode. However, there will always be slight deviations in the beam parameters or in the alignment.

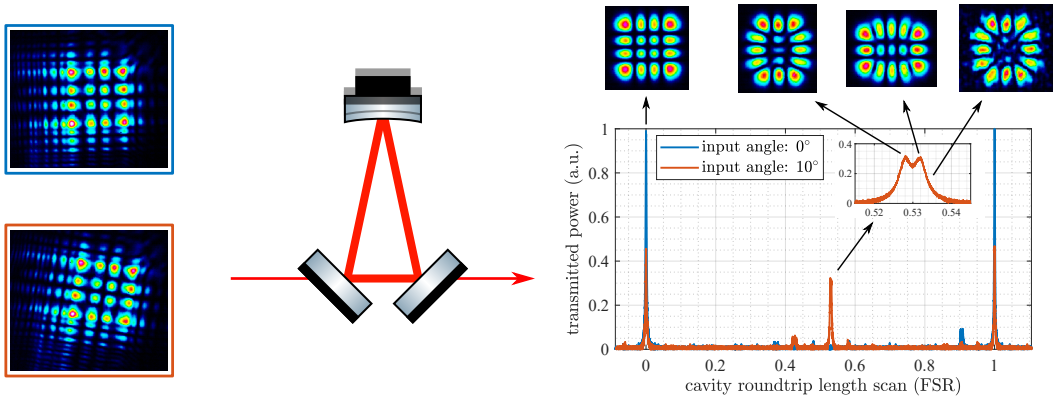

Figure 2.9: Left: unfiltered $HG_{3,3}$ field generated by a spatial light modulator for a rotation angle of 0° and 10° (top, bottom). Both fields are injected into a triangular cavity (middle). Right: transmitted power for both fields while the cavity length is scanned, normalised to the 0° $HG_{3,3}$ resonance peak. The coupling of the injected field to the cavity's $HG_{3,3}$ eigenmode decreases by about 55 % due to the rotation angle and, especially, one double-peak is additionally excited. The mode pictures were taken with a CCD camera. The rotation mismatch primarily corresponds to a mixture of HG and sinusoidal LG modes of the injected mode order, here 6.

For instance, the waist size of the probe beam might differ by a few percent from the reference waist size. For a fixed mismatch in the waist parameters, the alignment or arbitrary combinations of the above, the spatial overlap decreases more with higher mode order. Consequently, less power of the probe beam is coupled to the intended eigenmode of the cavity or a smaller fraction of the signal field is effectively detected with increasing mode order. This is analysed in more detail in [JF20; Tao+21b]. Consequences of these effects are also mentioned below under "control schemes" or in the chapters on the experimental work for this thesis.

For Hermite-Gaussian modes, there is an additional degree of freedom for mismatches which helical Laguerre-Gaussian modes as well as the $TEM_{0,0}$ mode are not affected by. The intensity distribution of a higher-order HG mode is not symmetric under arbitrary rotations around the propagation axis. In a defined eigenbasis, a rotated higher-order HG mode thus partially couples to one or more additional modes. Such a fixed eigenbasis can again be defined by e.g. a cylindrically asymmetric cavity, like a triangular or bow-tie cavity, or a reference beam, like a local oscillator field. An experimental example is shown in Figure 2.9 where a spatial light modulator was used to generate the $HG_{3,3}$ mode without and with a large rotation angle around the propagation axis (0° and 10°). The angle significantly reduces the coupling of the injected field to the cavity's $HG_{3,3}$ eigenmode and the figure also shows CCD camera pictures of the modes which primarily correspond to this mismatch: a mixture of HG and sinusoidal LG modes [Ful+10] of mode order 6. To my knowledge, a theoretical analysis of this rotational mismatch has not been published. A similar kind of mismatch arises for any mode for the case of linear polarisation.

Control schemes

The optimum performance of the gravitational-wave detectors relies on the quality of several different control schemes. For, instance, cavity lengths need to be stabilised to the resonance condition of the spatial mode of operation via the Pound-Drever-Hall (PDH) [Bla01] or dither-lock scheme, and the interferometer has to be stabilised to its operating point. Furthermore, automated alignment control schemes

are implemented. In all cited articles on the higher-order mode purities, cavity lengths were stabilised and the results showed that the PDH error signal for higher-order modes is equal to the one of the $TEM_{0,0}$ mode. In [Gat+14], a tabletop Michelson interferometer with arm cavities operated in the $LG_{3,3}$ mode was succesfully and robustly stabilised to the dark fringe. Hence, the performance of control schemes does, in general, not deteriorate with increasing mode order which agrees with my own experience.

This statement does, however, not strictly hold anymore if the increased sensitivity of higher-order modes to spatial mismatches is taken into account. The PDH error signals are only equal to the signal of the $TEM_{0,0}$ if the same amount of power is coupled into the respective cavity eigenmode. For the same injected power and a worse mode matching, the PDH signal is smaller and noise from the unmatched fraction becomes larger. The dark fringe of a Michelson interferometer can only be achieved as precisely in higher-order modes as in the $TEM_{0,0}$ mode for an identical interferometer contrast, that is, if the two returning beams from the interferometer arms have the same spatial overlap in the output. This is, however, harder to achieve with higher-order modes (compare with [Gat+14] and Chapter 6).

Cavity mode matchings, interferometer contrasts or other kinds of spatial beam overlaps can be improved and kept stable via feedback control schemes. Such a scheme may still lead to larger mismatches with increasing mode order due to the reduced mismatch tolerance of higher-order modes. If the scheme is gain limited, alternative mode matching sensing schemes, where the sensing gain increases in accordence with the increasing mismatch sensitivity of higher-order modes, are a possible solution [Tao+21a; Ful+17].

2.4 Summary

Mirror thermal noise can be a major limiting noise source for the future generation of gravitational-wave detectors and there are different approaches to reduce the different thermal noise contribution like an operation at cryogenic temperatures and the usage of materials for the mirror substrates and coatings with lower mechanical loss and lower optical absorption. One additional option is replacing the fundamental $TEM_{0,0}$ mode with a higher-order Laguerre-Gaussian (LG) or Hermite-Gaussian (HG) mode to mitigate test mass thermal noise. The benefit from higher-order modes can be intuitively understood by the fact that their intensity is more homogenously distributed on the mirror surfaces. Hence, these modes can better average over the thermal noise fluctuations which, for instance, arise from the Brownian motion of the constituent atoms of the mirror coating.

Flat-top beams were first proposed but require non-spherical mirrors. LG modes, especially the $LG_{3,3}$ mode, were the next candidates for their compatibility with the spherical mirrors of the gravitational-wave detectors. These modes, however, showed to be highly sensitive to astigmatism and are no longer carried forward in the design of the future GW detectors.

HG modes are also compatible with spherical mirrors. On the one hand, they are less efficient than LG modes in reducing thermal noise for a given mode order because their rectangular intensity distributions fit less well to the circular mirrors. On the other hand, they can benefit from a deliberate vertical astigmatism and perform almost as well as the $TEM_{0,0}$ mode with respect to power loss in the interferometer arms, mode purity and contrast defects.

Even though higher-order modes are currently not planned for future detctors, they are still a viable method for the thermal noise reduction. Previous reports, e.g. on the achievable mode purity and improved alignment control schemes, motivate further research on optimising the adaptation of the different interferometer techniques to these modes. One crucial example for these techniques, which the remainder of this thesis focuses on, is the application of squeezed states to reduce quantum noise.

In the next chapter, quantum noise in gravitational-wave detectors as well as squeezed states are introduced.

Chapter 3

Quantum Noise and Squeezed States of Light

Chapter 2 motivated the investigation of squeezed states of light in higher-order spatial modes regarding their usage in gravitational-wave detectors. This chapter aims to introduce the effects of quantum noise in these detectors as well as the corresponding definition, generation and application of squeezed states.

3.1 Quantum noise in gravitational-wave detectors

Quantum noise in gravitational-wave detectors was first analysed, especially regarding its possible reduction via squeezed light, by Caves in 1981 [Cav81]. A good introduction to this topic can also be found in [Heu18].

The quantum nature of light couples to the gravitational-wave readout in the form of noise via two mechanisms which can both be understood in the photon picture of light. In a laser beam, the photons are not evenly distributed. Instead, their arrival time at a given point in space follows the Poisson statistic [Fox06]

$$\mathcal{P}(n) = \frac{\bar{n}^n}{n!} e^{-\bar{n}} , \tag{3.1}$$

where $\mathcal{P}(n)$ is the probability of detecting n photons in a given time interval with a mean photon number of $\bar{n}$. The resulting varying photon number per measurement time interval becomes relevant at the detector readout because it implies random modulations in the measured optical power of the local oscillator field. Hence, these fundamental, quantum mechanical fluctuations in the photon number translate into fluctuations in the gravitational-wave readout (see Fig. 3.1). These fluctuations normalised to the mean photon number are called (relative quantum) *shot noise*.

In the interferometer arms, the same photon number fluctuations cause fluctuations in the radiation pressure which is exerted on the suspended input and end test masses by the incident laser beam (see also Fig. 3.1). As a consequence, the test masses are pushed out of their equilibrium position and, in combination with the restoring force (gravity), they act back on the reflected light field (back-action noise) modulating its phase. As a gravitational-wave also modulates the phase of the light fields in the interferometer arms, this effect competes with a gravitational-wave signal. It is referred to as (quantum) *radiation pressure noise*.

The amplitude spectral density associated with the effective gravitational-wave

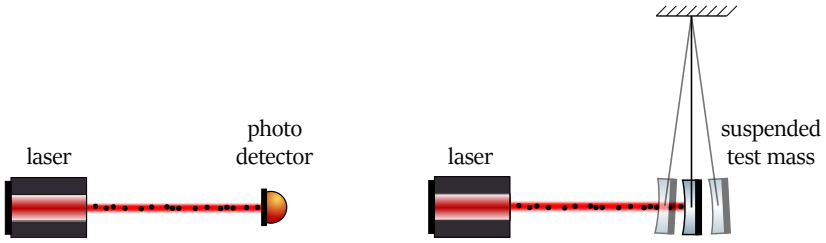

Figure 3.1: Photon picture of the quantum noise mechanisms in a gravitational-wave detector (based on [Heu18]). The photon distribution in a coherent laser beam follows a Poisson statistic. Left: this leads to fluctuations in the detected output power (shot noise). Right: the suspended test masses experience fluctuations in radiation pressure and transform them into phase fluctuations of the reflected light (radiation pressure noise).

strain of relative shot noise $h_{\text{rel SN}}$, radiation pressure noise h_{RPN} and the total quantum noise h_{QN}, computed as their incoherent sum, yields [Heu18]

$$\begin{aligned} h_{\text{rel SN}} &= \frac{1}{L_0}\sqrt{\frac{\hbar c\lambda}{2\pi P}} \\ h_{\text{RPN}} &= \frac{1}{mf^2L_0}\sqrt{\frac{\hbar P}{2\pi^3 c\lambda}} \\ h_{\text{QN}} &= \sqrt{h_{\text{rel SN}}^2 + h_{\text{RPN}}^2}\,, \end{aligned} \tag{3.2}$$

where L_0 is the mean interferometer arm length, $\hbar$ is the reduced Planck constant, c is the speed of light, λ is the wavelength, P is the mean optical power, m is the mass of the test mass and f is the measurement/signal frequency (see Fig. 3.2). While shot noise is frequency-independent, radiation pressure noise falls off with $1/f^2$. Hence, the total quantum noise is dominated by the latter at low frequencies and by the former at high frequencies. Furthermore, relative shot noise scales inversely with the square root of the optical power while radiation pressure noise scales with the square root of the power. From this relation, the *standard quantum limit* (SQL) [Vah08],

$$h_{\text{SQL}} = \sqrt{\frac{\hbar}{m\pi^2 f^2 L_0^2}}\,, \tag{3.3}$$

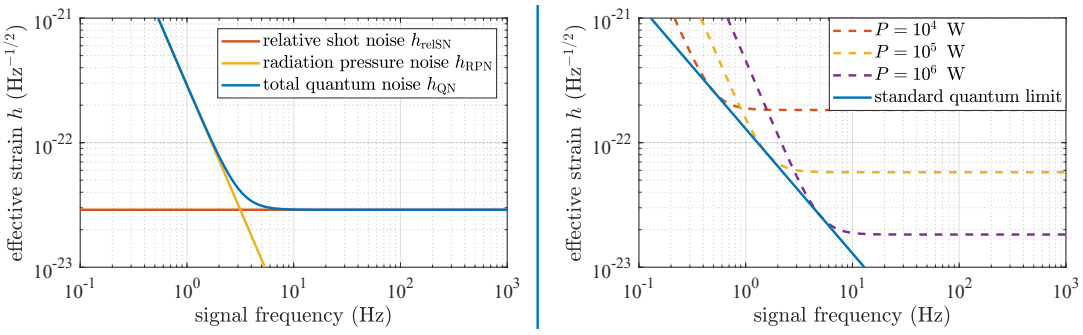

Figure 3.2: Left: The effective strain of quantum noise as an incoherent sum of relative shot noise and radiation pressure noise (see Eq. 3.2 with $L_0 = 4\,\text{km}$, $\lambda = 1064\,\text{nm}$, $P = 10^5\,\text{W}$ and $m = 40\,\text{kg}$). Right: the standard quantum limit as the minimum quantum-noise limited strain per frequency and respective optimised optical power P.

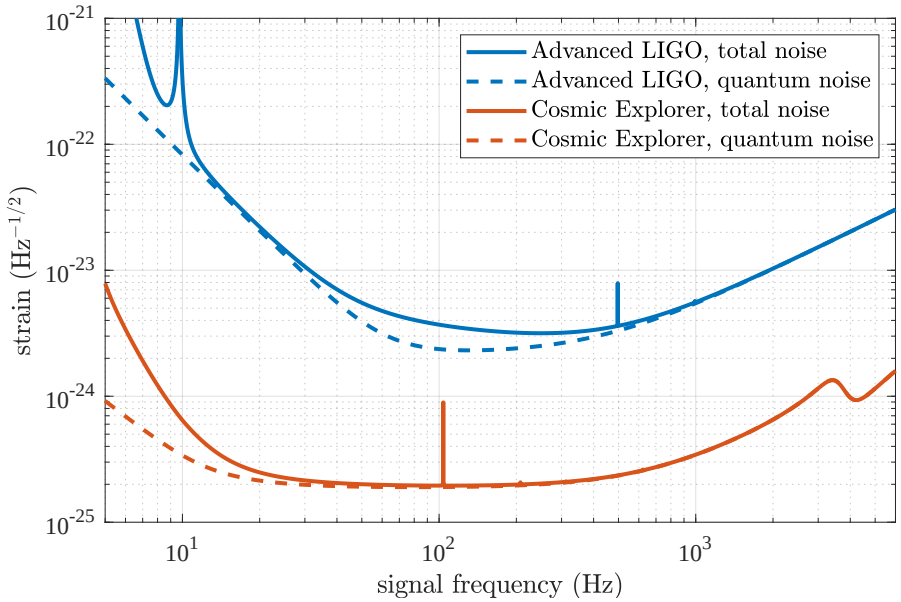

Figure 3.3: Calculated total and quantum noise budget of Advanced LIGO and Cosmic Explorer [Hal].

arises which is the minimum quantum-noise limited strain at a given signal frequency if the optical power is optimised (see also Fig. 3.2). Without advanced techniques, the sensitivity of a Michelson interferometer cannot reach below the SQL even if the other noise sources are sufficiently low.

Figure 3.3 shows the calculated total noise strain of the Advanced LIGO and Cosmic Explorer detectors as well as the respective quantum noise contributions.[1] The noise budgets are dominated by quantum noise over a broad frequency range. The same holds for the measured noise budgets in Advanced LIGO [Bui+20], Advanced Virgo [Ber+21] and KAGRA [KAG22] and for the calculated noise budget of the Einstein Telescope [ET 20] which renders the quantum noise reduction highly important. During the third joint observation run O3, the shot noise contribution was reduced via a maximum feasible optical power—and the application of squeezed (vacuum) states of light. This technique, which can also allow to surpass the standard quantum limit, will be explained in the following.

3.2 Squeezed states of light

This section provides the relevant background on squeezed states of light for this thesis. First, their definition is provided and the generation for gravitational-wave detectors is explained. It will be assumed that the reader is familiar with the basics and notation of quantum optics. More thorough introductions into the quantum-mechanical description of (squeezed) light can be found e.g. in [GK05; Fox06; Che07; Vah08]. Finally, the characterisation of squeezed states with a balanced homodyne detector as well as limitations and their application in a GW detector are discussed.

[1] In the detectors, the relative shot noise contribution increases with increasing signal frequency because the power buildup of the GW signal sidebands in the interferometer cavities decreases in agreement with the cavity linewidths. Hence, P is frequency-dependent.

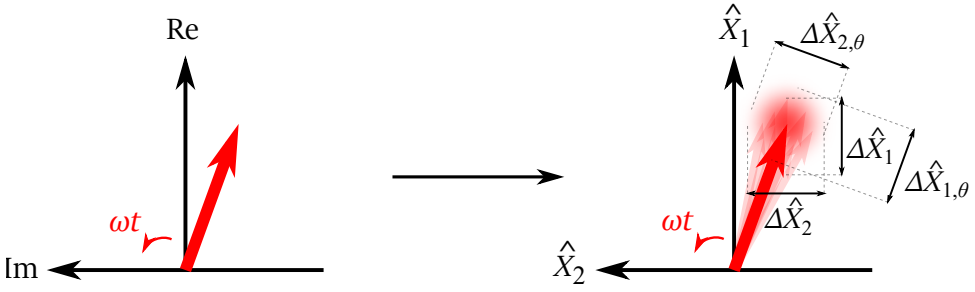

Figure 3.4: Left: electric field vector in the complex plane. Right: electric field phasor in the quadrature phase space with a "noise ball" that follows a Gaussian distribution with variance 1 and represents the quantum noise in the form of the quadrature's standard deviations $\Delta\hat{X}_1$ and $\Delta\hat{X}_2$. As the transparent phasors indicate, these uncertainties translate into amplitude and phase noise.

3.2.1 Definition

A coherent field in quantum optics

If an electric field $E(t)$ is described in the complex plane (here, at position $z = 0$ for simplicity), it can be decomposed into the real and imaginary part which oscillate 90° out of phase using Euler's formula:[2]

$$E(t) = E_0 e^{i\omega t} = E_0 \left[1\cos(\omega t) + i\sin(\omega t)\right] , \tag{3.4}$$

where E_0 is the coherent amplitude at the angular optical frequency ω. In quantum optics, the electric field operator $\hat{E}(t)$ can be written in a formally identical way [GK05]:

$$\hat{E}(t) = E_0 \left[\hat{X}_1\cos(\omega t) + \hat{X}_2\sin(\omega t)\right] . \tag{3.5}$$

Here, the real part, the imaginary part and the complex plane are replaced by the two quadrature operators $\hat{X}_1$ and $\hat{X}_2$ which span the quadrature phase space. These quadratures are also often referred to as the *amplitude* and *phase* quadrature, respectively. This quantisation now allows to derive quantum fluctuations of the electric field via the commutator and uncertainty relation which have to be fulfilled by the two orthogonal quadratures [Che07]:

$$\left[\hat{X}_1, \hat{X}_2\right] = 2i \qquad \Rightarrow \qquad \Delta^2\hat{X}_1\Delta^2\hat{X}_2 \geq 1 , \tag{3.6}$$

where Δ^2 denotes the variance of a respective time series. These uncertainties translate into "noise" in the quadratures $\hat{X}_1$ and $\hat{X}_2$ which is illustrated in Figure 3.4. In this figure, it is also shown that an arbitrary reference frame can be defined with

$$\begin{aligned} \hat{X}_{1,\theta} &= \hat{X}_1\cos\theta + \hat{X}_2\sin\theta \\ \hat{X}_{2,\theta} &= -\hat{X}_1\sin\theta + \hat{X}_2\cos\theta , \end{aligned} \tag{3.7}$$

which is co-aligned and co-rotating for $\theta = \omega t$. In the co-aligned frame, noise in $\hat{X}_{1,\omega t}$ and $\hat{X}_{2,\omega t}$ can directly be associated with amplitude and phase noise, respectively.

[2] Similar considerations apply to the magnetic part of an electro-magnetic field.

In quantum optics, a classical laser beam is described by a coherent state [GK05]

$$|\alpha\rangle = \exp\left(-|\alpha|^2/2\right) \sum_{n=0}^{\infty} \frac{\alpha^n}{\sqrt{n!}} |n\rangle \ , \tag{3.8}$$

which is a sum over the Fock states $|n\rangle$ weighted with respect to the mean photon number

$$\bar{n} = \langle\alpha| \hat{n} |\alpha\rangle = |\alpha|^2 \ , \tag{3.9}$$

where $\hat{n}$ is the number operator. Equation 3.8 can be interpreted as allocating a probability to the detection of n photons in a given measurement time interval dependent on the mean value $\bar{n}$, which results in the Poisson statistic from Equation 3.1.

Next, the variances of $\hat{X}_1$ and $\hat{X}_2$ can be calculated for a coherent state yielding [Che07]

$$\langle \Delta \hat{X}_{1,2} \rangle_\alpha^2 = \langle\alpha| \Delta^2 \hat{X}_{1,2} |\alpha\rangle = 1 \ , \tag{3.10}$$

such that a coherent state is a *minimum uncertainty* state with

$$\langle \Delta^2 \hat{X}_1 \rangle_\alpha \langle \Delta^2 \hat{X}_2 \rangle_\alpha = 1 \quad , \quad \langle \Delta^2 \hat{X}_1 \rangle_\alpha = 1 \quad , \quad \langle \Delta^2 \hat{X}_2 \rangle_\alpha = 1 \ , \tag{3.11}$$

independent of the value of $|\alpha|^2$. Another (or special) example for a minimum uncertainty state is the vacuum state $|0\rangle$. A vacuum state can be transformed into a coherent state via the displacement operator $\hat{D}(\alpha)$ [GK05]

$$|\alpha\rangle = \hat{D}(\alpha) |0\rangle \qquad \text{with} \qquad \hat{D}(\alpha) := \exp\left(\alpha \hat{a}^\dagger - \alpha^* \hat{a}\right) \ , \tag{3.12}$$

where $\hat{a}^\dagger$ and $\hat{a}$ are the creation and annihilation operators.

Quadrature squeezed states

Quantum mechanics does not allow a violation of the uncertainty relation but a redistribution of the uncertainties. While still a minimum uncertainty state, squeezed states are thus defined by exhibiting a noise variance below that of a vacuum state in an arbitrary quadrature (recall Eq. 3.7) which is said to be "squeezed". At the same time, this requires the noise variance in the orthogonal quadrature to be larger than that of a vacuum state, "anti-squeezed". Since this definition is based on the quadrature phase space, these states are also referred to as *quadrature squeezed states* defined by [Vah08]:

$$\Delta^2 \hat{X}_{1,\theta} < 1 \qquad \text{or} \qquad \Delta^2 \hat{X}_{2,\theta} < 1 \ . \tag{3.13}$$

A vacuum state $|0\rangle$ or a coherent state $|\alpha\rangle = \hat{D}(\alpha) |0\rangle$ can be transformed into a squeezed vacuum state or bright squeezed state, respectively, via the squeezing operator [GK05]

$$\hat{S}(\xi) := \exp\left[\frac{1}{2}\left(\xi^* \hat{a}^2 - \xi \hat{a}^{\dagger 2}\right)\right] \qquad \text{with} \qquad \xi = r e^{i\Theta} \ , \tag{3.14}$$

where $r \geq 0$ is the squeezing parameter and $0 \leq \Theta \leq 2\pi$ is the squeezing angle. The squeezed states are written as

$$|0, \xi\rangle = \hat{S}(\xi) |0\rangle \qquad \text{and} \qquad |\alpha, \xi\rangle = \hat{S}(\xi) |\alpha\rangle = \hat{S}(\xi) \hat{D}(\alpha) |0\rangle \ . \tag{3.15}$$

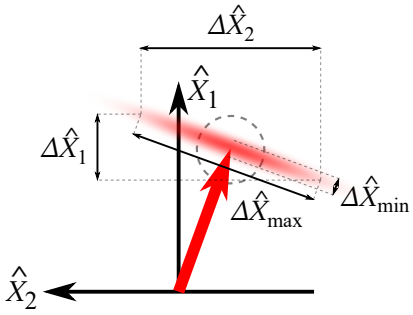

Figure 3.5: A bright squeezed state with reduced noise in the amplitude as seen from a co-aligned reference frame with $\Delta\hat{X}_{\mathrm{min,max}}$ and from the reference frame $\hat{X}_{1,2}$. The grey dashed circle indicates the classical uncertainty of a coherent state.

For this bright squeezed and squeezed vacuum state, the minimum and maximum noise variances, $\Delta^2\hat{X}_{\mathrm{min}}$ and $\Delta^2\hat{X}_{\mathrm{max}}$, are equal and read [Vah08]

$$\Delta^2\hat{X}_{\mathrm{min}} = e^{-2r} \leq 1 \qquad \text{and} \qquad \Delta^2\hat{X}_{\mathrm{max}} = e^{2r} \geq 1\,. \tag{3.16}$$

A reference frame with an arbitrary angle to the squeezing angle experiences the general noise variances [Vah08]

$$\begin{aligned} \Delta^2\hat{X}_{1,\theta}(r,\Theta) &= \cosh^2 r + \sinh^2 r - 2\sinh r\cosh r\cos\left(\theta-\Theta\right) \\ \Delta^2\hat{X}_{2,\theta}(r,\Theta) &= \cosh^2 r + \sinh^2 r + 2\sinh r\cosh r\cos\left(\theta-\Theta\right)\,. \end{aligned} \tag{3.17}$$

Figure 3.5 presents an example for a bright amplitude-squeezed state as seen from the reference frame with $\theta = \Theta$, which senses the minimum and maximum variances $\Delta\hat{X}_{\mathrm{min,max}}$, and as seen from the reference frame with $\theta = 0$, which effectively senses less squeezing and anti-squeezing because $1 > \Delta^2\hat{X}_1 > \Delta^2\hat{X}_{\mathrm{min}}$ and $1 < \Delta^2\hat{X}_2 < \Delta^2\hat{X}_{\mathrm{max}}$.

Squeezing and anti-squeezing level

If $\Delta^2\hat{X}_- < 1$ and $\Delta^2\hat{X}_+ > 1$ generally denote squeezed and anti-squeezed variances, the quantum noise reduction, or *squeezing level*, V_- and the *anti-squeezing level* V_+ are typically indicated in units of decibel:

$$\begin{aligned} V_-\,[\mathrm{dB}] &= -10\log_{10}\Delta^2\hat{X}_- \\ V_+\,[\mathrm{dB}] &= 10\log_{10}\Delta^2\hat{X}_+\,. \end{aligned} \tag{3.18}$$

3.2.2 Generation of squeezed states

Degenerate parametric down-conversion

Squeezed light sources for gravitational-wave detectors employ the second-order nonlinear process of degenerate parametric down-conversion. In this process, a nonlinear medium enables an interaction between a harmonic pump field at optical angular frequency ω_2 and a fundamental field at frequency $\omega_1 = \omega_2/2$, the latter of which shall be squeezed. If the nonlinear medium is pumped by a coherent harmonic field, harmonic photons will be converted into pairs of fundamental photons. These two photons are associated with a "signal" and an "idler" field which are degenerate in optical frequency, polarisation ("type-I" condition) and spatial mode.

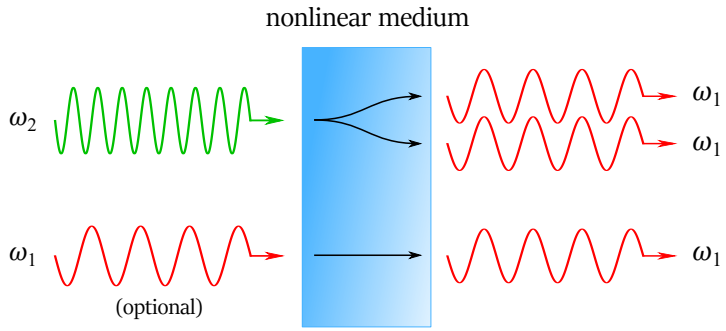

Figure 3.6: Degenerate parametric down-conversion: a harmonic pump field at optical angular frequency ω_2 is converted down into a signal and idler field which are degenerate in frequency $\omega_1 = \omega_2/2$, polarisation and spatial mode. Optionally, a seed field can be injected at the fundamental frequency. The residual harmonic field is omitted on the right side of the nonlinear medium.

This is visualised in Figure 3.6. Whether the fundamental field exhibits a coherent amplitude, as well, determines whether squeezed vacuum states or bright squeezed states are generated.

The Hamiltonian for this process reads [GK05]

$$\hat{H} = \hbar\omega_1 \hat{a}^\dagger \hat{a} + \hbar\omega_2 \hat{b}^\dagger \hat{b} + i\hbar\chi^{(2)} \left(\hat{a}^2 \hat{b}^\dagger - \hat{a}^{\dagger 2} \hat{b} \right) , \tag{3.19}$$

where $\hat{b}$ is the harmonic pump field, $\hat{a}$ is the fundamental signal/idler field and $\chi^{(2)}$ is the second-order optical susceptibility of the nonlinear medium. Here, the two terms in the brackets can be interpreted as the annihilation of one pump photon in order to create two fundamental photons and vice versa. If the pump field is assumed to be a strong coherent field which is approximately undepleted during the process, $\hat{b}$ and $\hat{b}^\dagger$ can be rewritten as $\beta \exp(-i\omega_2 t)$ and $\beta^* \exp(i\omega_2 t)$, respectively. The Hamiltonian in the interaction picture then reads

$$\hat{H} = i\hbar\chi^{(2)} \left[\beta^* \hat{a}^2 e^{i(\omega_2 - 2\omega_1)t} - \beta \hat{a}^{\dagger 2} e^{-i(\omega_2 - 2\omega_1)t} \right] . \tag{3.20}$$

This equation can further be simplified by inserting $\omega_2 = 2\omega_1$ and transformed into the evolution operator

$$\hat{U} = \exp\left(-\frac{i}{\hbar} \hat{H} t \right) = \exp\left(\beta^* \hat{a}^2 - \beta \hat{a}^{\dagger 2} \right) , \tag{3.21}$$

which is now equal to the squeezing operator in Equation 3.15.

The second-order nonlinear optical susceptibility and related processes

The optical response of a medium to an applied field $E(t)$ can be expressed in terms of the medium's polarisation $P(t)$, that is, its dipole moment per unit volume [Boy03],

$$P(t) = \epsilon_0 \left[\chi^{(1)} E(t) + \chi^{(2)} E^2(t) + \chi^{(3)} E^3(t) + \cdots \right] , \tag{3.22}$$

where $\chi^{(1,2,3)}$ are the linear, second-order and third-order nonlinear optical susceptibilities and ϵ_0 is the permittivity of free space.[3] While the first-order term is, for instance, related to the medium's refractive index $n = \sqrt{1+\chi^{(1)}}$, the second-order term is relevant for the generation of squeezed light for gravitational-wave detectors. Assuming an optical field with $E(t) = E_0 \cos(\omega_1 t)$ yields

$$P^{(2)} = \epsilon_0 \chi^{(2)} E_0^2 \cos^2(\omega_1 t) = \epsilon_0 \frac{\chi^{(2)} E_0^2}{2} \left[1 + \cos\left(\underbrace{2\omega_1}_{=\omega_2} t \right) \right] , \tag{3.23}$$

such that the second-order polarisation connects fields which oscillate at the fundamental and harmonic frequency. Hence, the second-order term enables the degenerate parametric down-conversion as well as the reversed process: second harmonic generation. In the latter, a fundamental pump field at ω_1 is up-converted to the harmonic frequency ω_2. This process is used in GWD squeezed light sources to generate the pump field for the parametric down-conversion. More generally, the second-order polarisation allows for sum- and difference-frequency generation if no degeneracy in the involved frequencies is assumed. However, only the special degenerate cases are relevant for this thesis.

For a typical material, $\chi^{(1)}$ is in the order of unity whereas $\chi^{(2)} \simeq 10^{-12}\,\mathrm{m\,V^{-1}}$ [Boy03]. To achieve high efficiencies in the parametric down-conversion and second harmonic generation, sufficiently strong pump fields and materials with a relatively large $\chi^{(2)}$ should be used. In this thesis, these are two different nonlinear crystals. One is made of 7 % magnesium-doped lithium niobate (MgO:$LiNbO_3$) for the $LG_{3,3}$ experiment in Chapter 4 and the other is periodically poled potassium titanyl phosphate (PPKTP) for the experiments with Hermite-Gaussian modes in the Chapters 5 and 6. These materials have nominal effective nonlinearities of $d_{\mathrm{eff}} = \chi^{(2)}/2 \simeq 3\,\mathrm{pm\,V^{-1}}$ and $9\,\mathrm{pm\,V^{-1}}$, respectively. Apparently, PPKTP exhibits a stronger nonlinearity which would theoretically imply higher efficiencies. Nevertheless, it was not used for the $LG_{3,3}$ experiment because two tested PPKTP crystals both highly distorted the injected $LG_{3,3}$ mode such that no proper second harmonic generation was feasible. The reason for this strong distortion was not further investigated and this extreme effect did not appear in the used MgO:$LiNbO_3$ crystal.

Phase matching

A second requirement for a high efficiency in parametric down-conversion and second harmonic generation is the conservation of momentum through the nonlinear medium which is referred to as phase matching. In the plane-wave approximation, the phase matching condition can be expressed via the wavenumbers k_1 and k_2 of the fundamental and harmonic field, respectively, and reads [Boy03]

$$k_2 = \frac{n_2 \omega_2}{c} = \frac{n_2 2\omega_1}{c} \overset{!}{=} \frac{2 n_1 \omega_1}{c} = 2k_1 \qquad \Rightarrow \qquad n_1 = n_2 \,, \tag{3.24}$$

where $n_{1,2} = n(\omega_{1,2})$ are the refractive indices at the fundamental and harmonic frequency. Since the refractive index in most dielectric nonlinear media does not satisfy the condition $n_1 = n_2$ but increases monotonically with ω, the phase matching condition is not automatically achieved. In this regard, it can be used that a

[3] In a more thorough description, the polarisation and optical field are treated as vectors and the susceptibilities become tensors of corresponding rank.

birefringent crystal typically has three optical axes where one of them, called "extraordinary", exhibits a lower refractive index n_e than the other "ordinary" two, n_o. In addition, these refractive indices are temperature-dependent. Examples for this are $\mathrm{d}n_o/\mathrm{d}T \approx 3 \times 10^{-6}\,\mathrm{K}^{-1}$ and $\mathrm{d}n_e/\mathrm{d}T \approx 37 \times 10^{-6}\,\mathrm{K}^{-1}$ [Vah08]. As a consequence, there are three approaches to still achieve phase matching [Boy03]:

1. *Type-I phase matching*
   "Type-I" again refers to the case where the signal and idler field at the fundamental frequency are degenerate in polarisation. For type-I phase matching, the harmonic field is orthogonally polarised. If the harmonic field experiences the lower of the two refractive indices n_e while the fundamental field experiences the higher index n_o, the phase matching condition is within the range accessible via temperature tuning. This type of phase matching is used in MgO:$LiNbO_3$.

2. *Type-II phase matching*
   Here, the signal and idler field are non-degenerate in polarisation. Phase matching can again be achieved via temperature tuning; however, this type of process is not suited for the generation of quadrature squeezing.

3. *Quasi phase matching*
   Type-I or type-II phase matching can be unfeasible for a couple of reasons. For example, a material may possess insufficient birefringence to compensate for the frequency dependence of the refractive index. Another example is KTP where accessing the desired effective nonlinearity requires the fundamental and harmonic field to be in the same polarisation. In this case, the crystal is divided into segments along which the phase matching condition is approximately satisfied. Then, one of the crystalline axes is inverted in adjacent segments such that the sign of the effective nonlinearity d_{eff} alternates and compensates for a mismatch $\Delta n = n_1 - n_2$. In this case, KTP becomes periodically poled KTP, short PPKTP. The advantage of quasi phase matching is that materials such as KTP with significantly larger effective nonlinearities can be employed.

A typical squeezed light source for gravitational-wave detectors

As derived above, degenerate parametric down-conversion (DPDC) can generate quadrature squeezed states of light at the fundamental optical frequency via the second-order nonlinear optical susceptibility of a material such as PPKTP or MgO:$LiNbO_3$. DPDC is driven by a pump field at the harmonic frequency which can be generated via the reversed process, second harmonic generation (SHG). In turn, SHG is pumped by a field at the fundamental frequency. This fundamental frequency is equal to the frequency at which the gravitational-wave detector is operated. Using SHG instead of an extra laser to provide the harmonic field has the advantage to ensure that the harmonic field is at exactly twice the GWD's operating frequency such that squeezed states are generated at exactly the operating frequency.

To increase the efficiency of both processes, they are conducted in an optical cavity to resonantly enhance at least one of the involved fields. In the LIGO and Virgo detectors, only the fundamental field resonates in the SHG cavity while the DPDC cavity allows a dual-resonance of both the fundamental and harmonic field [MV20; Tse+19]. The DPDC cavity is also referred to as optical parametric amplifier (OPA) or OPA cavity in this thesis. With this in mind, Figure 3.7 presents the simplified

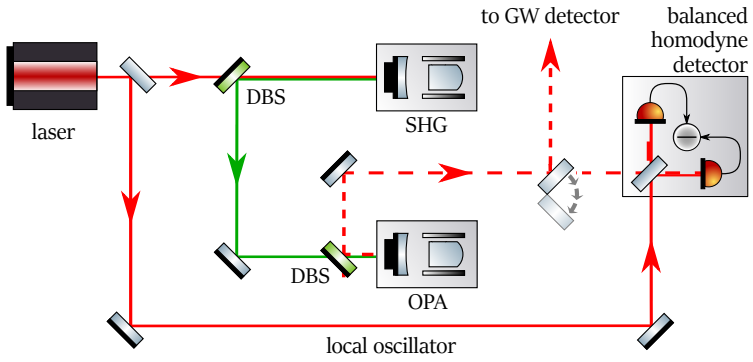

Figure 3.7: Simplified schematic of a tyical squeezed light source for a gravitational-wave (GW) detector. The laser emits light at the operating frequency of the detector. The harmonic field is generated in the SHG cavity and separated from the injected fundamental pump field by a dichroic beamsplitter (DBS). The harmonic field is guided to the OPA cavity where the squeezed field (dashed line) is generated. The squeezed field can either be guided to the GW detector, or to a balanced homodyne detector where its superposition with a local oscillator field is measured for characterisation.

schematic of a GWD squeezed light source. More detailed schematics can be found in the subsequent chapters. The cavities do not necessarily have to follow the linear design but can as well show the bow-tie geometry [Tse+19]. Furthermore, the crystal temperatures are stabilised to the optimum phase matching via a feedback control scheme using Peltier elements as actuators (not shown in the schematic).

Figure 3.7 already introduces a prominent experimental method to characterise squeezed states: a balanced homodyne detector, which will be discussed in the next section.

3.2.3 Characterisation with a balanced homodyne detector

In this thesis, the generated squeezed states are characterised by a balanced homodyne detector. This approach is used for both the direct detection of squeezing in the Hermite-Gaussian modes in Chapter 5 and the balanced homodyne detection scheme used for the Michelson interferometer in Chapter 6.

In general, a balanced homodyne detector measures the superposition of two incoming light fields at the two output ports of a 50:50 beamsplitter via photodetectors whose photocurrents are subtracted. Finally, a spectrum analyser calculates the noise power spectrum[4] of the resulting signal. This is shown in Figure 3.8. The following analysis is based on [Ste+15].

In the beamsplitter convention where one of the reflected fields experiences a phase shift of 180°, the output fields $\hat{c}$ and $\hat{d}$ can be written in terms of the input fields $\hat{a}$ (local oscillator field) and $\hat{b}$ (signal field) as follows:

$$\hat{c} = \frac{1}{\sqrt{2}}\left(\hat{a}e^{i\theta} + \hat{b}\right) \qquad \text{and} \qquad \hat{d} = \frac{1}{\sqrt{2}}\left(-\hat{a}e^{i\theta} + \hat{b}\right) , \tag{3.25}$$

[4]While the presented calculations commonly use the variance, a spectrum analyser typically displays a power spectrum (or power spectral density). Even though these quantities are not identical, they can be handled similarly with respect to the squeezing and anti-squeezing level. This especially holds if a frequency-dependent variance is obtained by applying a scanned bandpass filter to a time series.

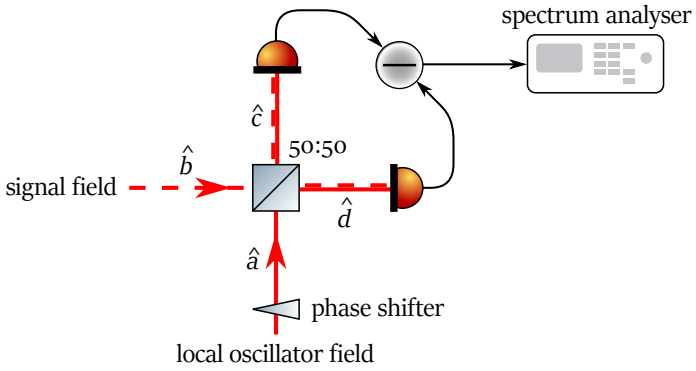

Figure 3.8: Schematic of a balanced homodyne detector where a local oscillator field $\hat{a}$ is superimposed with a signal field $\hat{b}$ on a 50:50 beamsplitter. The resulting fields $\hat{c}$ and $\hat{d}$ at the beamsplitter output ports are measured by photodetectors whose subtracted photocurrents are analysed by a spectrum analyser. A phase shifter can control the relative phase between the two input fields.

where the relative phase θ between the two fields can be controlled by a phase shifter in one of the input beam paths. The input fields can be linearised into the forms

$$\hat{a} = \alpha + \delta\hat{a} \qquad \text{and} \qquad \hat{b} = \beta + \delta\hat{b} \tag{3.26}$$

where α and β are the field's real-valued classical coherent amplitudes and $\delta\hat{a}$ and $\delta\hat{b}$ are the respective fluctuations. Furthermore, it is

$$\hat{X}_1^a = \frac{\hat{a} + \hat{a}^\dagger}{2} \qquad \hat{X}_2^a = -i\frac{\hat{a} - \hat{a}^\dagger}{2} \tag{3.27}$$

$$\hat{X}_1^b = \frac{\hat{b} + \hat{b}^\dagger}{2} \qquad \hat{X}_2^b = -i\frac{\hat{b} - \hat{b}^\dagger}{2}\,, \tag{3.28}$$

which defines the amplitude and phase quadratures $\hat{X}_1$ and $\hat{X}_2$ of the two input fields in terms of their respective annihilations and creation operators. The quadrature operators can be linearised in accordance with Equation 3.26, as well. The intensities of the output fields then read [Ste+15]

$$\begin{aligned}
\hat{c}^\dagger\hat{c} &= \frac{1}{2}\left(\alpha^2 + \beta^2 + 2\alpha\beta\cos\theta + 2\alpha\delta\hat{X}_1^a + 2\beta\delta\hat{X}_1^b + 2\alpha\delta\hat{X}_{-\theta}^b + 2\beta\delta\hat{X}_\theta^a\right) \\
\hat{d}^\dagger\hat{d} &= \frac{1}{2}\left(\alpha^2 + \beta^2 - 2\alpha\beta\cos\theta + 2\alpha\delta\hat{X}_1^a + 2\beta\delta\hat{X}_1^b - 2\alpha\delta\hat{X}_{-\theta}^b - 2\beta\delta\hat{X}_\theta^a\right),
\end{aligned} \tag{3.29}$$

where terms which are quadratic in the fluctuations are neglected and $\hat{X}_\theta = \hat{X}_1\cos\theta + \hat{X}_2\sin\theta$ similar to Equation 3.7. If these intensities are detected by the two photodetectors, their subtracted photocurrents yield

$$\hat{i}_- \propto \hat{c}^\dagger\hat{c} - \hat{d}^\dagger\hat{d} = 2\alpha\beta\cos\theta + 2\alpha\delta\hat{X}_{-\theta}^b + 2\beta\delta\hat{X}_\theta^a \tag{3.30}$$

which finally leads to a measured noise variance of

$$\Delta^2\hat{i}_- \propto P_{\mathrm{LO}}\,\Delta^2\hat{X}_{-\theta}^{\mathrm{sig}} + P_{\mathrm{sig}}\,\Delta^2\hat{X}_\theta^{\mathrm{LO}}\,, \tag{3.31}$$

where $P_{\mathrm{LO}} = \alpha^2$ and $P_{\mathrm{sig}} = \beta^2$ are the optical power in the local oscillator and signal field, respectively, and the superscripts of the quadrature variances are changed according to $a \to$ "LO" and $b \to$ "sig".

Measuring the squeezing and anti-squeezing level

Let us first assume that the balanced homodyne detector shall characterise squeezed vacuum states as these states are employed in gravitational-wave detectors. In this case, $P_{\mathrm{sig}} = 0$ such that the variance of the subtracted photocurrents is directly proportional to the variance of the signal field in a quadrature $\hat{X}_\theta^{\mathrm{sig}}$ which can be freely controlled via θ and, thus, via the phase shifter in the path of the local oscillator field. Now, the path of the squeezed field can first be blocked such that the signal field merely consists of the vacuum state with variance $\Delta^2\hat{X}^{\mathrm{vac}}$ independent of the relative phase θ. The corresponding measured variance is

$$\Delta^2\hat{i}_-^{\mathrm{vac}} \propto P_{\mathrm{LO}}\Delta^2\hat{X}^{\mathrm{vac}} \,. \tag{3.32}$$

If the squeezed field ("sqz") is then injected into the balanced homodyne detector, the relative phase θ can be set to measure the noise variances in the two quadratures which exhibit the maximally squeezed and anti-squeezed variances $\Delta^2\hat{X}_{\mathrm{min}}^{\mathrm{sqz}}$ and $\Delta^2\hat{X}_{\mathrm{max}}^{\mathrm{sqz}}$ yielding

$$\begin{aligned} \Delta^2\hat{i}_{-,\mathrm{min}}^{\mathrm{sqz}} &\propto P_{\mathrm{LO}}\Delta^2\hat{X}_{\mathrm{min}}^{\mathrm{sqz}} \\ \Delta^2\hat{i}_{-,\mathrm{max}}^{\mathrm{sqz}} &\propto P_{\mathrm{LO}}\Delta^2\hat{X}_{\mathrm{max}}^{\mathrm{sqz}} \,. \end{aligned} \tag{3.33}$$

The corresponding maximum squeezing and anti-squeezing levels V_{min} and V_{max} can then be computed in relation to the vacuum state and indicated in units of decibel:[5]

$$\begin{aligned} V_{\mathrm{min}}\,[\mathrm{dB}] &= -10\log_{10}\left(\frac{\Delta^2\hat{i}_{-,\mathrm{min}}^{\mathrm{sqz}}}{\Delta^2\hat{i}_-^{\mathrm{vac}}}\right) = -10\log_{10}\left(\frac{\Delta^2\hat{X}_{\mathrm{min}}^{\mathrm{sqz}}}{\Delta^2\hat{X}^{\mathrm{vac}}}\right) \\ V_{\mathrm{max}}\,[\mathrm{dB}] &= 10\log_{10}\left(\frac{\Delta^2\hat{i}_{-,\mathrm{max}}^{\mathrm{sqz}}}{\Delta^2\hat{i}_-^{\mathrm{vac}}}\right) = 10\log_{10}\left(\frac{\Delta^2\hat{X}_{\mathrm{max}}^{\mathrm{sqz}}}{\Delta^2\hat{X}^{\mathrm{vac}}}\right) \,, \end{aligned} \tag{3.34}$$

which becomes Equation 3.18 for $\Delta^2\hat{X}^{\mathrm{vac}} = 1$.

A variety of factors in the experimental setup can limit the measured squeezing and anti-squeezing levels. In general, these factors can be divided into two categories: a reduction in the detection efficiency, which can effectively be associated with optical loss, and an increase in phase noise. In the following, these factors are explained in more detail.

Reduction in the detection efficiency (optical loss)

Anything in the experimental setup which effectively causes optical loss in the squeezed field can be interpreted as a beamsplitter process. This beamsplitter reflects a fraction ρ of the squeezed field into an unused beam path while interfering the remaining transmitted squeezed field with a fraction ρ of the vacuum field that couples in through the open beamsplitter input port. Figure 3.9 illustrates that the interference of the squeezed and anti-squeezed noise with the vacuum noise reduces both the squeezing and anti-squeezing level. A squeezing or anti-squeezing level of $V_\mp$ then becomes [Meh12]

$$V_\mp(\eta_{\mathrm{det}}) = \mp 10\log_{10}\left[\eta_{\mathrm{det}}10^{V_\mp/10} + (1-\eta_{\mathrm{det}})\right] \,, \tag{3.35}$$

[5] Similar equations apply to the noise power spectrum at a given measurement frequency.

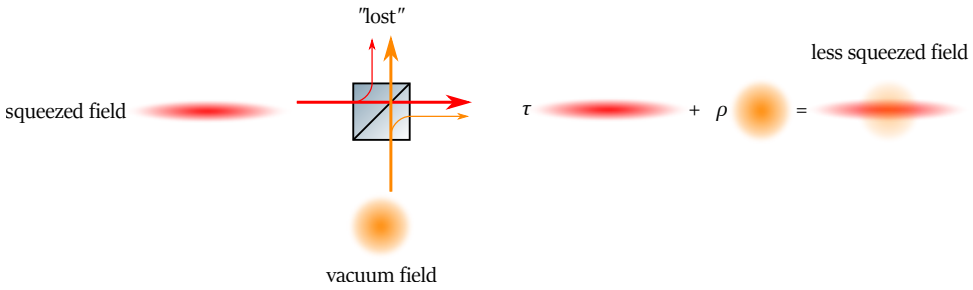

Figure 3.9: Optical loss can be interpreted as a beamsplitter process where a fraction ρ of the original field is lost and replaced by a corresponding fraction of the vacuum field which couples in through the open beamsplitter input port. The resulting superposition exhibits reduced squeezing and anti-squeezing values.

where $\eta_{\mathrm{det}} = 1 - L$ is the detection efficiency for the squeezed field and $L = \rho^2$ is the effective optical loss.

There are numerous sources for optical loss like imperfect high-reflectivity coatings where the transmitted fraction is lost, anti-reflective coatings where the residually reflected fraction is lost, clipping loss etc. In the following, three loss sources which are specifically important for a squeezed light setup and balanced homodyne detector are discussed.

1. *OPA escape efficiency*
   The escape efficiency indicates the fraction of the squeezed field that can "escape" the OPA cavity. It is given by [Vah08]

$$\eta_{\mathrm{esc}} = \frac{T}{T + L_{\mathrm{cav}}} \overset{\frac{L_{\mathrm{cav}}}{T} \ll 1}{\approx} 1 - \frac{L_{\mathrm{cav}}}{T}\,, \tag{3.36}$$

   where T is the power transmission coefficient of the OPA output coupler and L_{cav} is the OPA cavity roundtrip loss excluding the transmission through the output coupler. The escape efficiency can be increased via lower internal OPA losses which are determined by the properties and absorption of the crystal material, the residual transmission losses through the non-output coupler OPA mirrors and intra-cavity scattering. Furthermore, increasing T leads to a higher escape efficiency but also reduces the OPA cavity finesse and power buildup factor such that a more intense pump field is required. The finesse also affects the bandwidth of the OPA cavity (half-width at half maximum) which quantifies the measurement frequency range in which significant squeezing is generated. In this thesis, the OPA escape efficiency is $99.0(5)\,\%$ with an OPA bandwidth of about 25 MHz.

2. *Photodiode's quantum efficiency*
   The quantum efficiency of the two homodyne detector photodiodes indicates their efficiency in generating a photocurrent from the incident light field, that is, how many electrons contribute to the photocurrent output per incident photon. At a wavelength of 1064 nm, quantum efficiencies of up to 99.5 % can be reached [Vah+16]. This result was achieved with additional high-reflectivity "retro-reflectors". These mirrors can recycle the light that is reflected and not measured by the anti-reflective coated photodiodes. For this purpose, retro-reflectors are used in Chapter 6 for the Michelson interferometer experiment.

3. *The homodyne contrast*
For this effective loss source, the local oscillator and signal field have to be analysed in terms of their spatial mode content. In general, a normalised local oscillator field A_{LO} can be in an arbitrary superposition of spatial modes A_i:

$$A_{\mathrm{LO}} = \sum_i a_i A_i \qquad \text{with} \qquad \sum_i |a_i|^2 = 1\,. \tag{3.37}$$

The quantum fluctuations $\delta\hat{X}_i^{\mathrm{vac}}$ in these modes A_i, which enter the balanced homodyne detector through the signal port, will then contribute to the measured noise variance dependent on a_i according to (adapted from [Zha+17])

$$\Delta^2\hat{i}_-^{\mathrm{vac}} \propto P_{\mathrm{LO}} \sum_i |a_i|^2\, \Delta^2\hat{X}_i^{\mathrm{vac}}\,. \tag{3.38}$$

The squeezed field can only properly reduce the noise contribution from the spatial mode A_i if a corresponding fraction $|a_i|^2$ of the squeezed field is in the mode A_i. That is, the total fraction of the squeezed field which is not mode-matched to the local oscillator field only reduces noise in spatial modes which do not contribute to $\Delta^2\hat{i}_-^{\mathrm{vac}}$. Effectively, this fraction can be interpreted as part of the total optical loss.

If the squeezed field is written as

$$A_{\mathrm{sqz}} = \sqrt{\mu}A_{\mathrm{LO}} + \sqrt{1-\mu}A_{\mathrm{mis}}, \tag{3.39}$$

where μ indicates the mode matching between the local oscillator and squeezed field and A_{mis} is a normalised field associated with the mismatch, the effective optical loss from the imperfect mode matching is equal to μ. Usually, this loss source is, however, not indicated as μ but in terms of the homodyne contrast C as this quantity can be measured directly.

To measure the homodyne contrast, the squeezed field is replaced by a coherent field which is ideally set to have the same (here unit) optical power as the local oscillator field. These two fields are then superimposed on the 50:50 beamsplitter of the homodyne detector yielding the following output field in one of the beamsplitter output ports

$$\begin{aligned} A_{\mathrm{out}} &= \frac{i}{\sqrt{2}} A_{\mathrm{LO}}\, e^{i\theta} + \frac{1}{\sqrt{2}} A_{\mathrm{sqz}} \\ &= \frac{1}{\sqrt{2}} \left(i e^{i\theta} + \sqrt{\mu} \right) A_{\mathrm{LO}} + \sqrt{\frac{1-\mu}{2}}\, A_{\mathrm{mis}}\,. \end{aligned} \tag{3.40}$$

If θ is varied via the phase shifter in the local oscillator beam path, this results in the following maximum and minimum power

$$\begin{aligned} P_{\mathrm{max}} &= \left| A_{\mathrm{out}} \left(\theta = -\frac{1}{2} \right) \right|^2 = \frac{1}{2} \left[(1+\sqrt{\mu})^2 + 1 - \mu \right] = 1 + \sqrt{\mu} \\ P_{\mathrm{min}} &= \left| A_{\mathrm{out}} \left(\theta = +\frac{1}{2} \right) \right|^2 = \frac{1}{2} \left[(\sqrt{\mu}-1)^2 + 1 - \mu \right] = 1 - \sqrt{\mu}\,, \end{aligned} \tag{3.41}$$

and, finally, in the homodyne contrast

$$C := \frac{P_{\max} - P_{\min}}{P_{\max} + P_{\min}} = \sqrt{\mu}\,. \tag{3.42}$$

Hence, the associated effective optical loss, or reduction in the detection efficiency, is equal to the square of the measured and often indicated homodyne contrast.

Phase noise

The effect of phase noise can be understood via Figure 3.5 and Equation 3.17. Let us assume that we want to measure the quadrature with the minimum noise variance at $\theta_{\min} = \Theta$. If θ cannot be perfectly stabilised to Θ, e.g. due to residual high-frequency phase modulations or vibrations of reflective surfaces, a fraction of the maximum noise variance couples into the measurement. If the period of these phase jitters is shorter than the spectrum analyser's measurement time for one data point, the analyser will measure the noise variances over a certain span $\theta_{\min} - \delta\theta$ to $\theta_{\min} + \delta\theta$, resulting in a reduction of the effectively measured squeezing level. A similar consideration applies to the measurement of the anti-squeezing level and a corresponding simulation is shown below.

Theoretical model for the squeezing and anti-squeezing level

The squeezing process in an OPA cavity can be divided into the regimes below and above the *threshold power* [BK68; Las10]. Below this threshold, the cavity roundtrip losses are larger than the power gain in the fundamental field. Squeezed light sources for gravitational-wave detectors are operated in this regime as it allows for the generation of squeezed vacuum states and also for higher squeezing levels. Above threshold, the roundtrip power gain exceeds the losses and the OPA cavity generates a coherent amplitude at the fundamental frequency. This regime is not relevant for this thesis.

Below threshold and without phase noise, the detected squeezing ($-$) and anti-squeezing ($+$) level of the OPA output field can be computed as [Vah+16; PCK92]

$$\Delta^2 \hat{X}_{+,-} = 1 \pm \eta_{\text{det}} \frac{4\sqrt{P/P_{\text{thr}}}}{\left(1 \mp \sqrt{P/P_{\text{thr}}}\right)^2 + 4\left(\frac{2\pi f}{\gamma}\right)^2}\,, \tag{3.43}$$

where η_{det} is the detection efficiency including the total effective optical loss, P is the harmonic pump power, P_{thr} is the threshold power, f is the measurement frequency and $\gamma = c\,(T + L_{\text{cav}})\,/l_{\text{rt}}$ is the cavity decay rate with the speed of light c, the incoupling mirror's power transmissivity T of the OPA cavity, the round-trip loss L_{cav} and the round-trip optical path length l_{rt}. The effect of phase noise between the local oscillator field and the squeezed field can be included by assuming that the homodyne detector measures at a phase offset $\delta\theta$:

$$V_{\mp}\,[\text{dB}] = \mp 10 \log_{10}\left(\Delta^2 \hat{X}_{\mp} \cos^2\delta\theta + \Delta^2 \hat{X}_{\pm} \sin^2\delta\theta\right)\,. \tag{3.44}$$

Figure 3.10 illustrate the influences of the pump power P, the total optical loss $L_{\text{tot}} = 1 - \eta_{\text{det}}$ and the phase noise $\delta\theta$ on the squeezing and anti-squeezing level for the OPA cavity used in this thesis. For this cavity, the following parameters are assumed: $T = 8\,\%$, $L_{\text{cav}} = 0.12\,\%$, $l_{\text{rt}} = 72\,\text{mm}$. In the relevant ranges for this thesis (compare

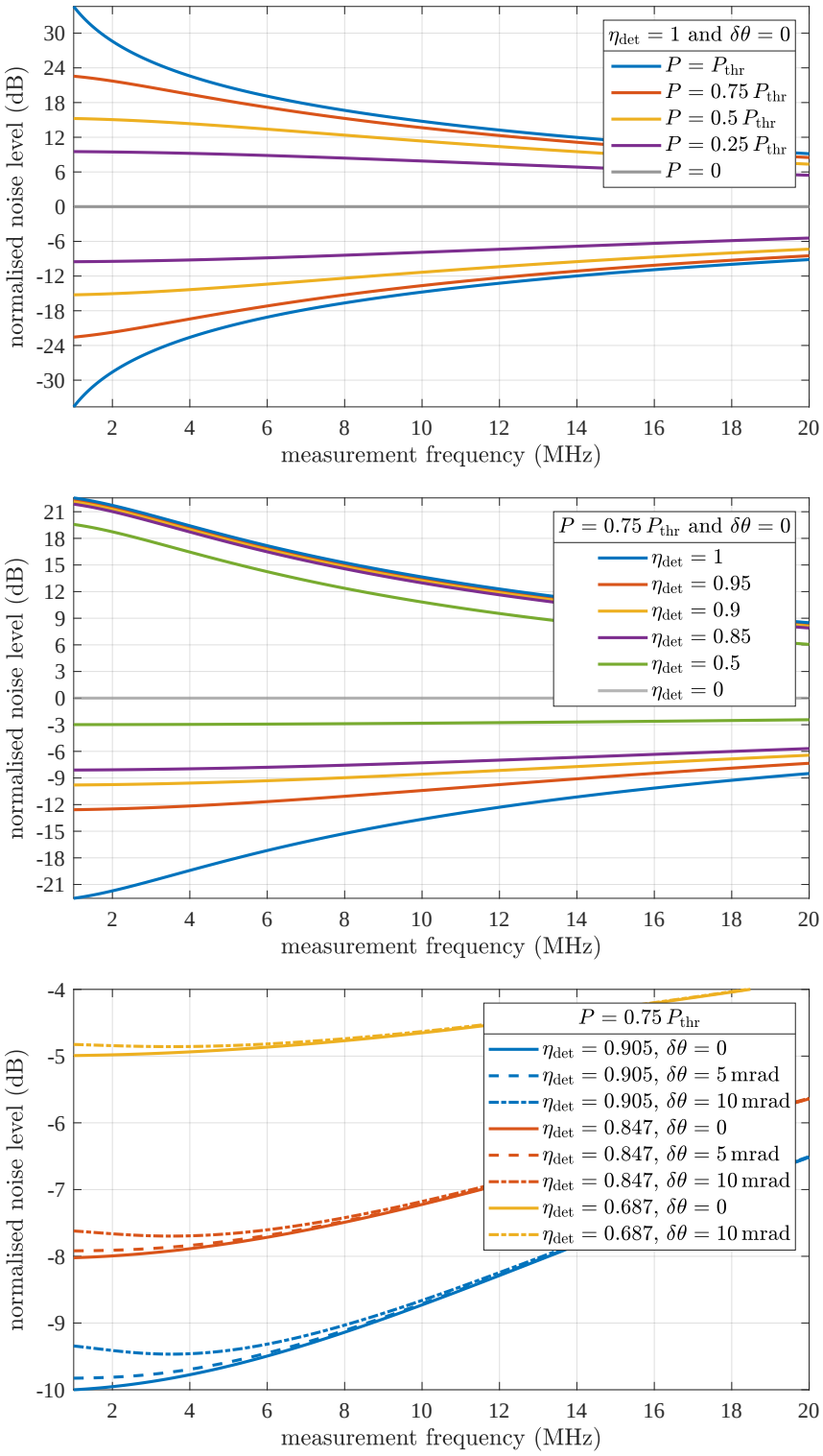

Figure 3.10: The three primary dependencies of the measured squeezing (< 0 dB) and anti-squeezing (> 0 dB) level according to the model from Eqs. 3.43 and 3.44. P: harmonic pump power, P_{thr}: threshold power, η_{det}: detection efficiency, $\delta\theta$: phase noise. The curves are normalised to the vacuum noise level at 0 dB.

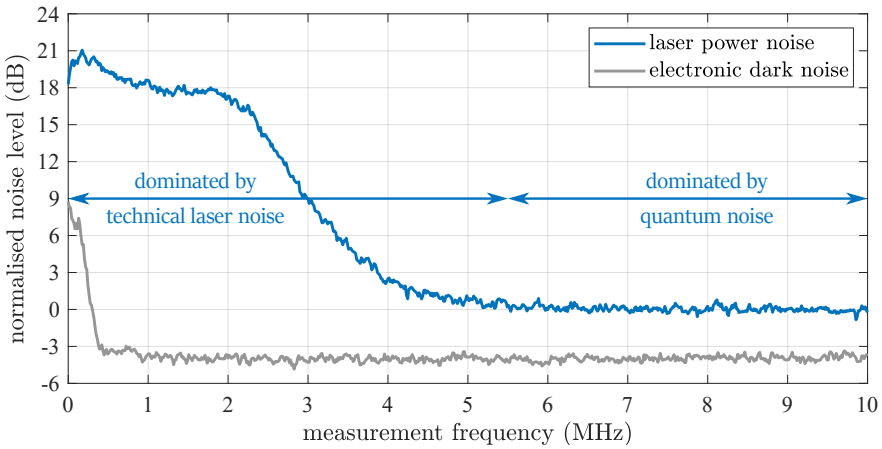

Figure 3.11: Laser power noise spectrum measured with a single photodetector at a dc photocurrent level of about 3.5 mA. The noise spectrum is normalised to the quantum noise at about 6 MHz to 10 MHz. The electronic dark noise is not subtracted from the data.

with Chapters 5 and 6), optical loss as well as phase noise leave the anti-squeezing approximately unaffected. A given amount of optical loss reduces the squeezing level more for a higher initial squeezing level. The same holds for the phase noise which additionally has a larger impact if a given squeezing level coincides with a larger anti-squeezing level, i.e. in combination with optical loss.

3.2.4 Bright squeezed states and technical laser noise

As explained in Section 5.1, the squeezed light source in this thesis generates bright squeezed states instead of squeezed vacuum states. As a consequence, technical laser (power) noise influences the balanced homodyne detection. Figure 3.11 shows the power noise spectrum of the laser beam in transmission of the (input) mode cleaner in Figures 5.4 and 6.4 measured with a single photodetector at a dc photocurrent level of about 3.5 mA.[6] The spectrum is dominated by quantum (shot) noise above a measurement frequency of about 5.5 MHz and by technical laser noise below that.

Even though the local oscillator field always exhibits this power noise, it cancels out for the measurement of squeezed or classical vacuum states if the homodyne detector is sufficiently balanced. If the signal field, however, has a coherent amplitude and, thus, also exhibits technical laser power noise, this technical noise appears in the amplitude quadrature ($\theta = 0$) and dominates the corresponding noise variance $\Delta^2 \hat{X}_0^{\mathrm{sig}}$ in the first term of Equation 3.31 at lower frequencies. Vice versa, the coherent amplitude in the signal field now also amplifies the technical laser noise in the local oscillator's amplitude quadrature $\Delta^2 \hat{X}_0^{\mathrm{LO}}$ via the second term of Equation 3.31.

If bright squeezed states are generated, the amplitude quadrature is typically also the squeezed quadrature because the parametric process in the OPA cavity then not only reduces the quantum noise in this quadrature but also the coherent amplitude via parametric deamplification [Che07; Ebe13]. Hence, the measured squeezing level can be largely reduced at lower frequencies due to technical laser noise (see Fig. 5.7 or 6.9). The exact reduction in the squeezing level depends on the optical power in the signal field for a given power in the local oscillator field. Assuming

[6] The typical relaxation peak is not visible because of an active noise eater which was used for all presented measurements.

that the local oscillator and signal field roughly have the same relative intensity noise RIN, Equation 3.31 becomes

$$\Delta^2\hat{i}_-(\theta=0) \propto P_{\mathrm{LO}}P_{\mathrm{sig}}\mathrm{RIN}^2 \qquad \text{with} \qquad \mathrm{RIN} := \frac{\sqrt{P_{\mathrm{LO,sig}}\Delta^2\hat{X}_0^{\mathrm{LO,sig}}}}{P_{\mathrm{LO,sig}}} \ ([\mathrm{Ste}+15]) \ , \tag{3.45}$$

such that doubling the power in the signal field increases the measured variance of the technical laser noise by 3 dB. Furthermore, a comparison between Figure 3.11 and 3.10 shows that the effect of phase noise is qualitatively similar to the shape of the power noise spectrum. Thus, the effect of phase noise can be masked by sufficiently large technical laser noise.

Finally, a coherent amplitude in the signal field also has an effect at frequencies where $\Delta^2\hat{i}_-$ is dominated by quantum noise. This is again due to the non-zero second term in Equation 3.31 ($P_{\mathrm{sig}}\,\Delta^2\hat{X}_\theta^{\mathrm{LO}}$) where the coherent amplitude in the signal field beats with the quantum noise in the local oscillator field. $\Delta^2\hat{X}_\theta^{\mathrm{LO}}$ does not reduce with squeezing in the signal field. Even though $P_{\mathrm{LO}} \gg P_{\mathrm{sig}}$ should always hold, the contribution from the LO's quantum noise can reduce the effectively measured squeezing level.

3.2.5 Application of squeezed states

Conceptually, a simple Michelson interferometer with balanced homodyne detection does not differ from a mere balanced homodyne detector setup. If the Michelson interferometer is operated at the dark fringe, it effectively reflects any injected (squeezed) field and can thus simply be interpreted as a complex mirror in the signal beam path which potentially causes large optical losses as well as an increase in the phase noise (e.g. about 25 % and 15 mrad in Advanced LIGO [Tse+19], 21 % and 17 mrad in GEO600 [Lou+21], respectively). If a squeezed field is injected into the interferometer output, it replaces the otherwise entering vacuum field and reduces the measured quantum noise variance in the readout, when stabilised to the correct phase. To avoid that the interferometer output signal field now propagates to the squeezed light source, a Faraday rotator is employed as shown in Figure 3.12 (see also Chapter 6 for more details). The same principle applies to an advanced gravitational-wave detector; however, the effects of the recycling, arm and filter cavities have to be taken into account, as well, because optical cavities can further degrade squeezed states via additional optical losses and decoherence/dephasing [Kwe+14].

As a gravitational wave modulates the phase of the interferometer arm fields, the corresponding GW signal appears in the phase quadrature. For an efficient quantum shot noise reduction, the squeezed quadrature thus has to be stably aligned with the phase quadrature of the interferometer output field via a coherent control scheme [Vah+06; Che+07]. The second-generation gravitational-wave detectors have followed this approach resulting in effective quantum shot noise reduction levels of about 3 dB in Advanced LIGO and Advanced Virgo [Bui+20; Ber+21] as well as 6 dB in GEO600 [Lou+21].

Let us assume that quadrature $\hat{X}_2$ of the injected squeezed field is aligned with the signal (phase) quadrature of the interferometer arm field. Intuitively, reduced quantum noise in the $\hat{X}_2$ quadrature will then be beneficial. At the same time, noise in the $\hat{X}_1$ quadrature of the injected squeezed field will be aligned with the amplitude quadrature of the interferometer arm field, thereby causing amplitude noise.

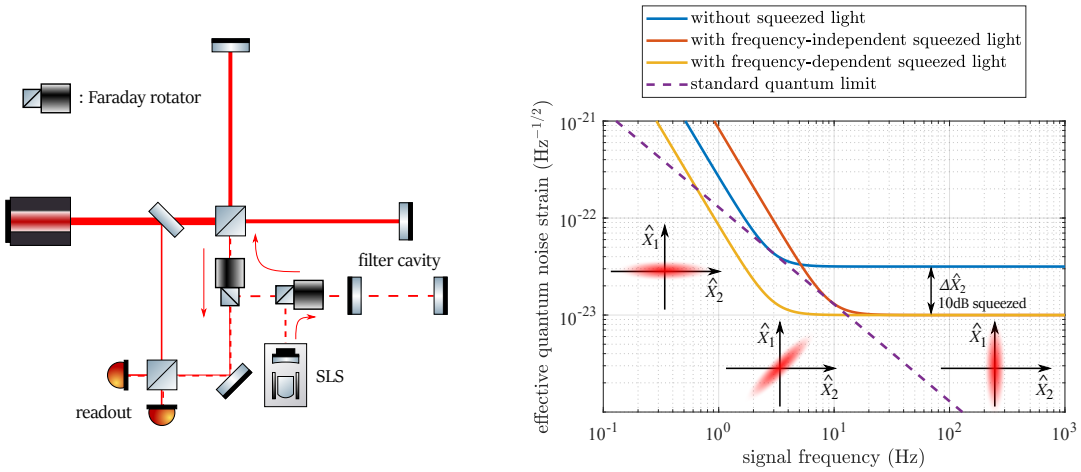

Figure 3.12: Left: frequency-independent squeezed states are provided by the squeezed light source (SLS). A Faraday rotator (FR) first reflects the squeezed states towards the filter cavity and then transmits the frequency-dependent squeezed states towards the interferometer. Here, a second FR first injects the squeeezd states into the detector and then transmits them together with the signal field to the readout. Right: frequency-independent squeezing has the same effect as an increase in the optical laser power, reducing shot noise but increasing radiation pressure noise (based on [Bas14]). If the squeezing ellipse was rotated by 90°, radiation pressure noise would be reduced at the cost of an increased shot noise. With frequency-dependent squeezing, i.e. a frequency-dependent squeezing angle, both radiation pressure and shot noise can be mitigated at the same time in the respective frequency ranges. This theoretically allows to surpass the standard quantum limit.

This amplitude noise can be associated with the fluctuations in the photon number from Section 3.1 and is, thus, transformed into phase noise by the suspended mirrors' back action. Hence, noise in the squeezed field's $\hat{X}_1$ quadrature also ultimately appears in the signal quadrature as quantum radiation pressure noise which could first be directly measured by the Advanced Virgo detector [Ace+20]. Future gravitational-wave detectors therefore aim to implement frequency-dependent squeezing where the noise in the $\hat{X}_1$ quadrature is reduced at low frequencies, where radiation pressure noise dominates, and noise in the $\hat{X}_2$ quadrature is reduced at high frequencies, where shot noise dominates (see also Fig. 3.12). This is achieved via a filter cavity and using the fact that the phase of the reflected field depends on the relation between the cavity's resonance frequency and the frequency of the reflected field [Zha+20; Pol21; ET 20; Eva+21].

3.3 Summary

A coherent laser beam exhibits fundamental quantum-mechanical noise in amplitude and phase. The quantum amplitude noise couples into the readout of a gravitational-wave detector via two mechanisms: first, the suspended test masses in the interferometer arms experience a fluctuating radiation pressure which pushes them out of their position of equilibrium; second, amplitude noise in the detected output field directly couples into the readout as shot noise. With these two mechanisms combined, quantum noise has dominated the noise budgets of the second-generation gravitational-wave detectors over a broad frequency range and is expected to remain a main limitation for the third generation. Hence, a lot of research

focuses on the proposed mitigation methods like speedmeters, variational readout and white-light-cavity schemes, which are at different stages of development. They are summarised and reviewed e.g. in [DKM19; CM04].

The most prominent quantum noise reduction is the injection of squeezed states of light into the detectors' output ports. Radiation pressure and shot noise can be related to two orthogonal quadratures of the vacuum state which normally enters a Michelson interferomter through the output port and beats with the coherent field that is injected through the input port. Squeezed vacuum states redistribute the quantum noise in these quadratures such that either radiation pressure or shot noise is reduced at the cost of increasing the other. So far, gravitational-wave detectors only reduced the shot noise contribution via squeezed light with only a small effect of the anti-squeezing on the radiation pressure noise. However, they currently work on the implementation of frequency-dependent squeezing which will reduce both of the two quantum noise contributions in the frequency range where they are dominant, respectively.

A typical squeezed light source for a gravitational-wave detector employs second harmonic generation and subsequent degenerate parametric down-conversion. These are nonlinear optical processes which use the second-order susceptibility of a crystalline medium and are enhanced via optical cavities. The generated squeezed states can then be characterised via a balanced homodyne detector where they are superimposed with a strong coherent local oscillator field on a 50:50 beamsplitter. If the power in the two beamsplitter outputs is detected and subtracted, the variance, or noise power spectrum, of this signal directly corresponds to the variance, or noise power spectrum, of the sensed quadrature (to a good approximation).

In this thesis, the typical approach to generate squeezed states shall be adapted to higher-order modes. The next chapter will start with this endeavour by investigation the second harmonic generation of the Laguerre-Gaussian $LG_{3,3}$ mode.

Chapter 4

Second Harmonic Generation of the $LG_{3,3}$ mode

Chapter 3 explained the role of second harmonic generation (SHG) in the typical squeezed light source for gravitational-wave detectors. To examine the differences in this process between the fundamental and higher-order laser modes, this chapter first analyses the SHG theoretically for an arbitrary Laguerre-Gaussian mode, including a numerical simulation of the $TEM_{0,0}$ and $LG_{3,3}$ SHG. The simulation results are then compared to an experimental investigation of the $TEM_{0,0}$ and $LG_{3,3}$ SHG with a special focus on the conversion efficiencies and harmonic output fields.

This chapter is based on the publications [HVW20a] and [HVW20b].

4.1 Theory and numerical simulation

The theory behind second-order nonlinear processes like second harmonic generation (SHG) is, in general, well known and understood. Boyd's book on nonlinear optics is a good introduction [Boy03], and in [BK68] the influence of the focusing parameter as well as of double-refraction on both the second harmonic generation and parametric down-conversion were already thoroughly discussed for the $TEM_{0,0}$ mode. Nevertheless, the research on nonlinear processes for the $TEM_{0,0}$ mode is still ongoing (e.g. on more efficient phase matchings [LS07]) and is also progressing for higher-order modes [Dho+96; Cou+97; Del+07; BTL08; Zho+14].

Based on this literature, the theoretical investigation in this section aims to answer additional questions about second harmonic generation with a focus on the comparison between the $TEM_{0,0}$ and $LG_{3,3}$ mode. Using a novel description that tracks the phases in the harmonic field in relation to the excited crystal polarisation will allow to give an in-depth analysis on how the Gouy phase affects the phase matching and the harmonic output field. Moreover, it will provide the first detailed explanation for the influence of the pump intensity distribution on the conversion efficiency. Both of these aspects will be investigated in relation to the focusing parameter. Without loss of generality, the Laguerre-Gaussian mode basis will be assumed while differences to the Hermite-Gaussian basis will be indicated.

4.1.1 Mathematical description for Laguerre-Gaussian modes

The first goal of this section is to get an intuitive understanding of how the fundamental pump field is converted into the (second) harmonic field by a nonlinear medium, and of why most higher-order modes excite more than one harmonic mode. For this purpose, the differential equation for the harmonic field will be discretised into an iterative equation which describes the conversion process within

a finitely small segment of the nonlinear medium in which the influence of phase matching is negligible. For simplicity, the fundamental field is assumed undepleted through the whole nonlinear medium, the polarisation direction is omitted and walk-off effects as well as absorption are neglected. The assumed phase matching is type-I as employed in gravitational-wave detectors. Type-II phase matching would require two orthogonally polarised pump fields.

The second goal is to use this iterative equation to understand how different parameters influence the conversion efficiency and to numerically simulate the $TEM_{0,0}$ and $LG_{3,3}$ SHG. This simulation will not only show how the power in the excited harmonic modes evolves through the nonlinear medium but will also illustrate how the Gouy phase affects the conversion into the different excited harmonic modes.

Helical Laguerre-Gaussian modes (rewritten)

In this section, the general expression of a Laguerre-Gaussian (LG) mode in cylindrical coordinates ($\mathbf{r} = (r, \varphi, z)$) from Equation 2.4 will be rewritten as follows:

$$\begin{aligned} \mathrm{LG}_{p,l}(\mathbf{r}, t) &= A_{p,l}(\mathbf{r}) \times e^{i(kz-\omega t+\beta)} \\ &= T_{p,l}(\mathbf{r}) \times \Phi_{p,l}(z) \times e^{i(kz-\omega t+\beta)} \end{aligned} \tag{4.1}$$

with

$$\begin{aligned} T_{p,l}(\mathbf{r}) &:= \frac{1}{w(z)} \sqrt{\frac{2p!}{\pi(p+|l|)!}} \left(\frac{\sqrt{2}r}{w(z)}\right)^{|l|} L_p^{|l|}\left(\frac{2r^2}{w^2(z)}\right) \times e^{-ik\frac{r^2}{2q(z)}+il\varphi} \\ \Phi_{p,l}(z) &:= e^{i\gamma_{p,l}\Psi(z)} \,. \end{aligned} \tag{4.2}$$

Here, the normalised amplitude distribution $A_{p,l}$ is separated into the normalised transverse amplitude distribution $T_{p,l}(\mathbf{r})$, which defines the mode and includes normalisation factors, and into the Gouy phase term $\Phi_{p,l}(z)$ with the Gouy phase factor $\gamma_{p,l} := 2p + |l| + 1$. The separation into $T_{p,l}$ and $\Phi_{p,l}$ will help to understand how the fundamental and harmonic field interact in the nonlinear medium. Without loss of generality, β will be set to zero.

Differential equation of the harmonic field and its discretisation

The homogeneous paraxial Helmholtz equation (PHE) describes an electric field and its propagation in an undisturbed environment without any sources or sinks. In a nonlinear medium, there is, however, a source[1] when the dielectric crystal polarisation is excited by the fundamental pump field and emits light at the harmonic frequency. This effect can be included in the PHE by adding a corresponding source term $S(\mathbf{r})$ on the right-hand side [Boy03; Del+07]:

$$\left[\nabla_T^2 - 2ik_2\partial_z\right] A_2(\mathbf{r}) = \underbrace{-2\frac{\omega_2^2}{c^2} d_{\mathrm{eff}} A_1^2(\mathbf{r}) e^{i\Delta kz}}_{=:\, S(\mathbf{r})} \,, \tag{4.3}$$

where the indices 1 and 2 denote the total fundamental pump field and total harmonic field including their optical power, respectively, c is the speed of light in vacuum, d_{eff} is the effective nonlinearity of the nonlinear crystal medium and

[1] There is a potential sink, as well, if the harmonic field is reconverted into the fundamental field.

$\Delta k = 2k_1 - k_2$ is the wavevector mismatch which corresponds to a difference in the refractive indices according to $\Delta k = 4\pi\Delta n/\lambda_1$ (for SHG) with $\Delta n = n_1 - n_2$. Since the SHG process is considered to be time-invariant, the term $\exp(-i\omega t)$ is omitted.

The derivative ∂_z can be discretised as

$$\partial_z A_2(r,\varphi,z) = \frac{A_2(r,\varphi,z+\Delta z) - A_2(r,\varphi,z)}{\Delta z} \tag{4.4}$$

and be applied to the homogeneous PHE that describes the mere propagation of the field A_2 without any source term:

$$A_2(r,\varphi,z+\Delta z) = A_2(r,\varphi,z) - k'\Delta z \cdot \nabla_T^2 A_2(r,\varphi,z)\,, \tag{4.5}$$

where $k' := i/(2k_2)$. Thus, only the transverse derivative ∇_T^2 determines how any electric field locally changes phase and shape during propagation. Applying Equation 4.4 and 4.5 to Equation 4.3 yields

$$\begin{aligned} A_2(r,\varphi,z+\Delta z) &= \underbrace{A_2(r,\varphi,z) - k'\Delta z\nabla_T^2 \cdot A_2(r,\varphi,z)}_{=A_2'(r,\varphi,z+\Delta z)} + \underbrace{k'\Delta z \cdot S(r,\varphi,z+\Delta z)}_{=:C^h(r,\varphi,z+\Delta z)} \\ &= A_2'(r,\varphi,z+\Delta z) + C^h(r,\varphi,z+\Delta z)\,. \end{aligned} \tag{4.6}$$

Here, Δz has to be added in the arguments of S and C^h to ensure that they are evaluated at the same z position as A_2'. This addition becomes negligible for $\Delta z \to dz$.

Using Equation 4.6, the evolution of the harmonic field along the nonlinear medium can be described as follows: the initial harmonic field A_2 is present at the position z and propagates up to $z + \Delta z$ according to Equation 4.5 as if there was no source term. At the position $z + \Delta z$, A_2 is renamed into A_2' and interferes with C^h which describes the harmonic field that is emitted from the excited crystal polarisation. The resulting field becomes the new initial field A_2 for the next iteration step. Based on this mechanism, the numerical simulation in Section 4.1.2 and 4.1.3 will compute how the harmonic field iteratively progresses through the nonlinear medium. The resolution parameter Δz was reduced until the solution converged. In the following, C^h will be referred to as *excited* harmonic field and the superscript h indicates the harmonic frequency.

Excited harmonic modes

To understand why most higher-order modes excite more than one harmonic mode, $A_2' = 0$ can be set in Equation 4.6. In this way, there is no initial harmonic field and no interference or phase relation between A_2' and C^h has to be taken into account. The equation reduces to

$$A_2(r,\varphi,z+\Delta z) = C^h(r,\varphi,z+\Delta z) \propto A_1^2(r,\varphi,z+\Delta z) \tag{4.7}$$

where the mode composition of the excited harmonic field C^h, which is proportional to the square of the pump field A_1^2, determines the harmonic field A_2. Figure 4.1 illustrates the meaning and consequence of the dependence of A_2 on the square of the pump field: the conversion efficiency is not constant across the transverse plane but larger where the pump intensity is higher. Hence, the intensity profiles of the excited harmonic fields show narrower peaks than the $TEM_{0,0}$ and $LG_{3,3}$ pump modes, and the peak height relations are altered in the latter case, as well. The harmonic field excited by the $TEM_{0,0}$ mode can still be represented as one single mode which

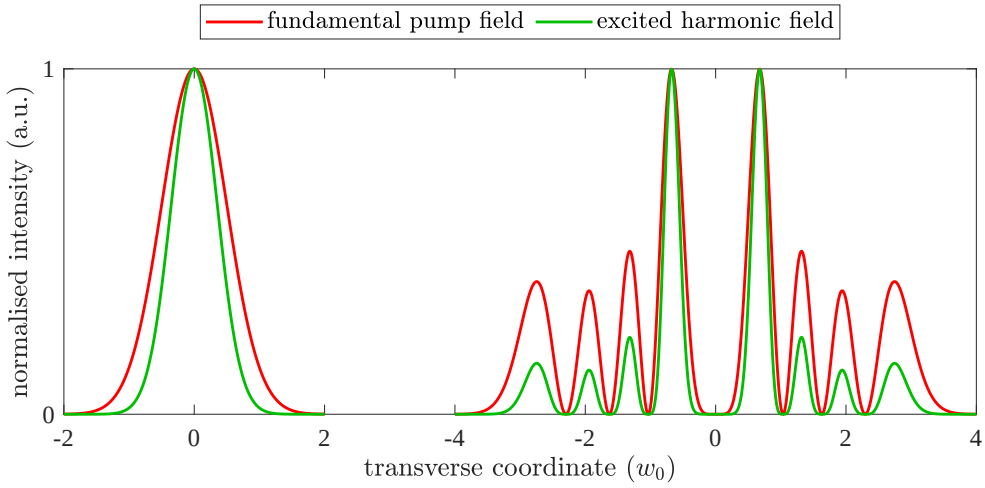

Figure 4.1: Intensity distributions of the fundamental pump field and excited harmonic field, normalised to their respective peak value, at the waist position ($z = 0$) in case of the $TEM_{0,0}$ (left) and $LG_{3,3}$ (right) mode. The x axis refers to an arbitrary coordinate axis across the transverse plane where w_0 is the waist size of the fundamental field in both cases.

is the harmonic $TEM_{0,0}$ mode in a basis where the waist size is reduced by a factor of $\sqrt{2}$. However, this is generally not possible in the case of a higher-order pump mode because there is no mode parameter which changes the peak height relations or the ring widths while keeping their separation constant. In this case, the harmonic field needs to be represented as a superposition of several modes, where the basis with a waist reduction factor of $\sqrt{2}$ is again the most reasonable choice. In this basis, the $LG_{3,3}$ mode excites the harmonic modes $LG_{0,6}$, $LG_{2,6}$, $LG_{4,6}$ and $LG_{6,6}$ (derived from $LG^2_{3,3}$).

The next section will show that the initial harmonic field A'_2 as well as the excited harmonic field C^h can be decomposed into the same modes at each z position in the nonlinear medium, where each mode experiences an interference between both fields independent of the other modes.

Mode composition of the excited harmonic field C^h

Let us start by writing the mode composition of the harmonic field which is excited at $z + \Delta z$ as a function of the pump field A_1. Assuming that the SHG is pumped by an $LG_{p,l}$ mode, the excited harmonic field $C^h \propto A_1^2 \propto A_{p,l}^2$ can be written as (refer to [Cou+97] for the relation in the third line)

$$\begin{aligned} C^h(r,\varphi,z+\Delta z) &\propto A^2_{p,l}(r,\varphi,z+\Delta z) = T^2_{p,l}(r,\varphi,z+\Delta z)\Phi^2_{p,l}(z+\Delta z) \\ &\propto T^2_{p,l}(r,\varphi,z+\Delta z)\Phi_S(z+\Delta z) \\ T^2_{p,l}(r,\varphi,z+\Delta z) &= \sum_{m=0}^{p} t_{2m,2l}(z+\Delta z)T^h_{2m,2l}(r,\varphi,z+\Delta z) \\ \Phi_S(z+\Delta z) &= \Phi^2_{p,l}(z+\Delta z) = e^{i2(2p+|l|+1)\Psi(z+\Delta z)}\,. \end{aligned} \tag{4.8}$$

where the squared $T^2_{p,l}(r,\varphi,z+\Delta z)$ is not normalised and $t_{2m,2l}(z+\Delta z)$ are real-valued coefficients. The $T^h_{2m,2l}$ describe the normalised transverse amplitude distributions (nTADs) which correspond to the harmonic modes with twice the frequency

of the fundamental field and a reduced waist size according to $w_0^h = w_0/\sqrt{2}$. The third line implies that the excited harmonic field can be decomposed into the harmonic LG modes with $l' = 2l$ and $p' = 0, 2, \ldots, 2p$ and, thus, consists of more than one mode if $p > 0$. Hence, the $LG_{3,3}$ mode with $p = 3$ and $l = 3$ excites the harmonic modes with $p' = 0, 2, 4, 6$ and $l' = 6$. The fourth line implies that the modes in the excited harmonic field all have the same Gouy phase Φ_S which only depends on the mode order of the pump field.

Equation 4.8 shows that the excited harmonic field C^h consists of the same modes T^h_{2m2l} independent of the z position which are solely determined by the pump mode. Furthermore, the mode composition of the harmonic field A_2 does not change upon the propagation from z to $z + \Delta z$ as each mode can propagate independently. Hence, if the modes in the harmonic field A_2 and excited harmonic field C^h match at one z position, they will also match at every subsequent z position.[2] With this in mind, Equation 4.8 can be inserted into Equation 4.6, resulting in a mode-resolved version:

$$\begin{aligned}
A_2(r,\varphi,z+\Delta z) &= A_2'(r,\varphi,z+\Delta z) + C^h(r,\varphi,z+\Delta z) \\
&= \sum_{m=0}^{p} \Big[a_{2m,l'}(z) A^h_{2m,l'}(r,\varphi,z+\Delta z) + \\
&\qquad \bar{c}_{2m,l'}(z+\Delta z) T^h_{2m,l'}(r,\varphi,z+\Delta z) \Phi_S(z+\Delta z) \Big] \\
&= \sum_{m=0}^{p} \Big[a_{2m,l'}(z) A^h_{2m,l'}(r,\varphi,z+\Delta z) + \\
&\qquad c_{2m,l'}(z+\Delta z) \underbrace{T^h_{2m,l'}(r,\varphi,z+\Delta z)\Phi_{2m,l'}(z+\Delta z)}_{=A^h_{2m,l'}(r,\varphi,z+\Delta z)} \Big] \\
&= \sum_{m=0}^{p} \underbrace{\Big[a_{2m,l'}(z) + c_{2m,l'}(z+\Delta z) \Big]}_{= a_{2m,l'}(z+\Delta z)} A^h_{2m,l'}(r,\varphi,z+\Delta z)
\end{aligned} \tag{4.9}$$

with

$$c_{2m,l'}(z+\Delta z) := \bar{c}_{2m,l'}(z+\Delta z)\Phi_S(z+\Delta z)/\Phi_{2m,l'}(z+\Delta z)\,, \tag{4.10}$$

where $a_{2m,l'}(z)$ are the complex coefficients for the harmonic field which has been generated in the previous iteration steps up to z. They do not change with the mere propagation between z and $z + \Delta z$, which is completely described by $A^h_{2m,l'}$. The complex $c_{2m,l'}(z + \Delta z)$ and $\bar{c}_{2m,l'}(z + \Delta z)$ coefficients correspond to the excited harmonic field at $z + \Delta z$. $\bar{c}_{2m,l'}$ is converted into $c_{2m,l'}$ such that $A^h_{2m,l'}$ can be extracted from both terms.

Equations 4.8 and 4.9 can be adapted to the HG basis by using the corresponding expressions for $T^2_{m,n}$ and Φ_S.

Phase matching

Let us now analyse the phase matching between the inital harmonic field A_2' and excited harmonic field C^h. If $\Delta\alpha_{2m,l'}(z + \Delta z) \in (-\pi, \pi]$ denotes the phase difference between $a_{2m,l'}(z)$ and $c_{2m,l'}(z + \Delta z)$ in Equation 4.9, $\Delta\alpha_{2m,l'} \approx 0$ will result in constructive interference and a maximum power increase in the harmonic mode $LG_{2m,l'}$. In contrast, $|\Delta\alpha_{2m,l'}| \approx \pi$ will result in destructive interference and a maximum power reduction. The phase matching of each harmonic mode thus corresponds to

[2] Strictly, this only holds for $\Delta n = 0$, but suffices as an approximation for a reasonable small Δn.

the evolution of $\Delta\alpha_{2m,l'}$ through the nonlinear medium which is determined by the evolution of the phases in A_2' and C^h.

The harmonic field is given by

$$A_2(\mathbf{r}) = \sum_{m=0}^{p} a_{2m,l'}(z) T^h_{2m,l'}(\mathbf{r}) \Phi_{2m,l'}(z) \,. \tag{4.11}$$

Since the excited harmonic field consists of the same harmonic modes, it includes the same nTADs $T^h_{2m,l'}$. However, in contrast to A_2, each of these nTADs is weighted by the same Gouy phase and wavevector mismatch:

$$\begin{aligned} C^h(\mathbf{r}) &= i\mathcal{C}_{p,l}(z) \left[\sum_{m=0}^{p} c'_{2m,l'} T^h_{2m,l'}(\mathbf{r}) \right] \Phi_S(z) e^{i\Delta k z} \,, \\ \sum_{m=0}^{p} &\left| c'_{2m,l'} \right|^2 = 1 \,. \end{aligned} \tag{4.12}$$

where the real-valued $c'_{2m,l'}$ coefficients quantify the fractional contributions of the harmonic modes to the excited harmonic field and $\mathcal{C}_{p,l}(z)$ is the dimensionless real-valued amplitude. See Equation 4.13 for the relation between $c_{2m,l'}$ and $c'_{2m,l'}$.

The difference in the Gouy phases $\Phi_{2m,l'}$ in A_2 and Φ_S in C^h causes the phases of the coeffcients $a_{2m,l'}(z)$ and $c_{2m,l'}(z+\Delta z)$ in Equation 4.9 to evolve differently for the following reason. $a_{2m,l'}$, especially its phase, remains constant between z and $z+\Delta z$ because $A^h_{2m,l'}$ completely describes this propagation in the harmonic field. This is not true for $c_{2m,l'}$ because the Gouy phase of the excited harmonic field evolves faster than $A^h_{2m,l'}$ accounts for. This results in a phase change of $c_{2m,l'}$ between z and $z+\Delta z$ via Equation 4.10 such that any constructive interference in Equation 4.9 decays. This decay depends on the difference in the Gouy phase factors of each mode $\Delta\gamma_{p,l,p',l'} := \gamma_S - \gamma_{p',l'} = 2\gamma_{p,l} - \gamma_{p',l'}$, where $\gamma_S =: 2\gamma_{p,l}$ is the Gouy phase factor of the excited harmonic field, $\gamma_{p',l'}$ is the Gouy phase factor of the corresponding harmonic mode and $\Delta\gamma_{p,l,p',l'} > 0$, always. The decay also depends on the Rayleigh range, or the focusing parameter, as it is another factor in the Gouy phase term (see Eq. 2.4) and, for instance, does not occur in the limit of plane waves. Futhermore, a wavevector mismatch can slow down or speed up the decay and be used to (partly) restore a good phase matching for at least one of the excited harmonic modes.

The same applies to the HG basis with $\Delta\gamma_{m,n,m',n'} = 2\gamma_{m,n} - \gamma_{m',n'}$.

Change in harmonic power and the phase difference $\Delta\alpha$

A comparison between Equations 4.9 and 4.12 yields

$$c_{2m,l'}(z) = c_{p',l'}(z) = i\mathcal{C}_{p,l}(z) c'_{p',l'} e^{i\Delta\gamma_{p,l,p',l'}\Psi(z)} e^{i\Delta k z} \tag{4.13}$$

such that the optical power of each mode in the harmonic field changes between $z-\Delta z$ and z as follows

$$\begin{aligned} \Delta P^h_{p',l'}(z) &\propto \left| a_{p',l'}(z) \right|^2 - \left| a_{p',l'}(z-\Delta z) \right|^2 \\ &\propto \left| \mathcal{C}_{p,l}(z) c'_{p',l'} \right|^2 + 2 \left| a_{p',l'}(z-\Delta z) \mathcal{C}_{p,l}(z) c'_{p',l'} \right| \cos\left(\Delta\alpha_{p',l'}(z) \right) \end{aligned} \tag{4.14}$$

with the phase difference

$$\Delta\alpha_{p',l'}(z) = \alpha_{a,p',l'}(z - \Delta z) - \frac{\pi}{2} - \Delta\gamma_{p,l,p',l'}\Psi(z) - \Delta kz \tag{4.15}$$

where $\alpha_{a,p',l'}$ is the phase of $a_{p',l'}$ and $\pi/2$ corresponds to the factor i.

According to the second line of Equation 4.14, the change in power is given by two terms. The first is only relevant if there is no inital harmonic field A_2 yet. It quickly becomes negligible with a present harmonic field. Then, the second term determines the change in power with four individual influences:

1. $|a_{p',l'}(z - \Delta z)|$: the initial power present in the respective mode. Hence, the power change scales proportionally with the initial power in the harmonic power.

2. $\mathcal{C}_{p,l}(z)$: the amplitude of the excited harmonic field which includes the pump intensity. The pump intensity increases with a decreasing pump beam radius and is largest at the waist position. It is also larger if the power of the pump mode is confined to a smaller transverse area which, in general, implies a smaller mode order. These two effects are shown in Figure 4.2 for the pump modes $\mathrm{TEM}_{0,0}$ and $\mathrm{LG}_{3,3}$ depending on the focusing parameter $\xi = L/(2z_R)$, where L is the geometrical length of the crystal. A larger focusing parameter implies a smaller waist size and, thus, a higher maximum intensity at the waist position but also a stronger beam divergence. Hence, $\mathcal{C}_{p,l}(z)$ or $|\mathcal{C}_{p,l}(z)|^2$ changes more extremely for larger focusing parameters.

   With a comparison between Equations 4.3 and 4.12, a (pump) mode-dependent effective nonlinearity can be defined as

$$d_{p,l}(z) := d_{\mathrm{eff}}\mathcal{C}_{p,l}(z). \tag{4.16}$$

   The ratio $d_{p1,l1}/d_{p2,l2}$ for two different pump modes, e.g. $d_{0,0}/d_{3,3} = 2.64$, is z-, ξ- (assuming equal values for both modes) and medium-independent (d_{eff} cancels out) and directly quantifies the difference of the two pump modes in their intensity distributions as well as in their interaction with the nonlinear medium.

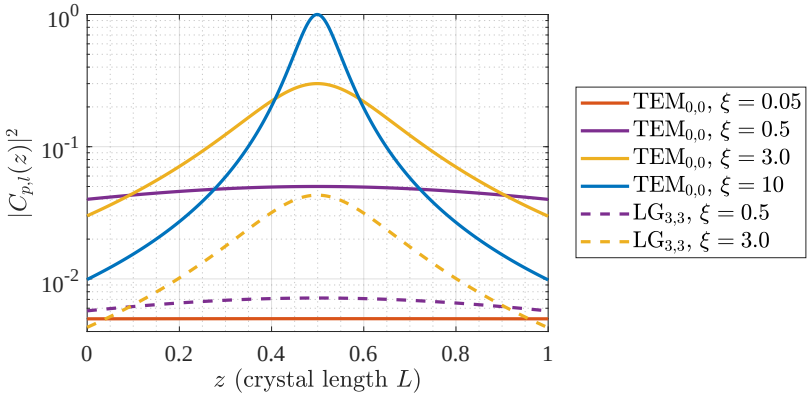

Figure 4.2: Evolution of the power contained in the excited harmonic field in terms of $|\mathcal{C}_{p,l}(z)|^2$ for different focusing parameters ξ along the crystal on a logarithmic scale, normalised to the maximum of $\mathrm{TEM}_{0,0}$, $\xi = 10$ [HVW20b]. The waist of the pump field is located at the centre of the crystal. The curves evolve in accordance with the pump intensities.

3. $c'_{p',l'}$: the fractional contribution of the respective mode in the excited harmonic field. This parameter is constant through the crystal.

4. $\Delta\alpha_{p',l'}(z)$: the phase difference between $a_{p',l'}(z-\Delta z)$ and $c_{p',l'}(z)$ which depends on the difference in the Gouy phase factors $\Delta\gamma_{p,l,p',l'}$ and on the wavevector mismatch Δk as expected. With no initial harmonic field, the phase term $\pi/2$ is imprinted on the phase of $a_{p',l'}$ in the first iteration step and is irrelevant for the phase matching. Furthermore, the phase $\alpha_{a,p',l'}$ of $a_{p',l'}$ adjusts to the phase of $c_{p',l'}$ in each iteration step via the interference; however, it will lag behind if the phase of $c_{p',l'}$ changes too quickly. According to the cosine in Equation 4.14, the phase difference will result in a power decrease if $|\Delta\alpha_{p',l'}(z)| > \pi/2$ and if the second term dominates the first one at this point. For a certain $|\Delta\alpha_{p',l'}(z)| \approx \pi/2$, the two terms cancel each other out and $c_{p',l'}$ merely affects the phase of $a_{p',l'}$ such that the harmonic power remains constant.

The following numerical simulations will show how the second harmonic generation and the conversion efficiencies of the individual excited modes depend on these four parameters.

4.1.2 Single-pass simulation for $TEM_{0,0}$ and $LG_{3,3}$

$TEM_{0,0}$ single-pass SHG

In general, the $TEM_{0,0}$ mode allows for the highest conversion efficiencies. It only excites one single harmonic mode, which implies the largest possible value for $c'_{p',l'} = c'_{0,0} = 1$, provides the highest pump intensity, that is the largest $\mathcal{C}_{p,l}$, and has the smallest possible difference in the Gouy phase factors $\Delta\gamma_{p,l,p',l'} = \Delta\gamma_{0,0,0,0} = 1$, such that $\Delta\gamma_{0,0,0,0}\Psi(z) = \text{atan}(z/z_R)$ in Equation 4.15. Figure 4.3[3] shows the simulation of the accumulated power in the harmonic $TEM_{0,0}$ mode through the nonlinear crystal in relation to the phase difference for different focusing parameters (see also Appendix A.1). It assumes the waist to be located at the centre of the crystal and is split up into the focusing regimes below (weak, left figure) and above (strong, right figure) optimum focusing, where optimum focusing corresponds to $\xi = 2.84$ [BK68]. The simulation produces the same relative results for any set of wavelengths $\lambda_{1,2}$, refractive indices $n_{1,2}$, effective nonlinearity d_{eff} and pump power if the pump field is treated as undepleted. Since the same pump power is assumed in each case, the ratios of the final harmonic powers at $z = L$ (refering to the figure axis) are equal to the ratios of the respective conversion efficiencies.

A detailed description of the results for the different focusing parameters can be found in [HVW20b]. In the following, the main aspects are summarised to understand the different limitations below and above the optimum focusing:

1. *Below optimum focusing*
   According to Figure 4.2, weak focusing implies a small pump intensity, that is a small $\mathcal{C}_{p,l}$ through the crystal. Hence, the pump field does only weakly interact with the nonlinear medium and cannot generate high levels of harmonic power.
   Weak focusing also implies a weak influence of the Gouy phase term $\Delta\gamma_{0,0,0,0}\Psi(z) = \text{atan}(z/z_R)$ on the phase difference. In this regime, very good

[3] The z range of the figure is $0 \leq z \leq L$ with respect to the crystal, while the range of the simulation is actually $-L/2 \leq z \leq L/2$ with respect to the waist position in the crystal centre.

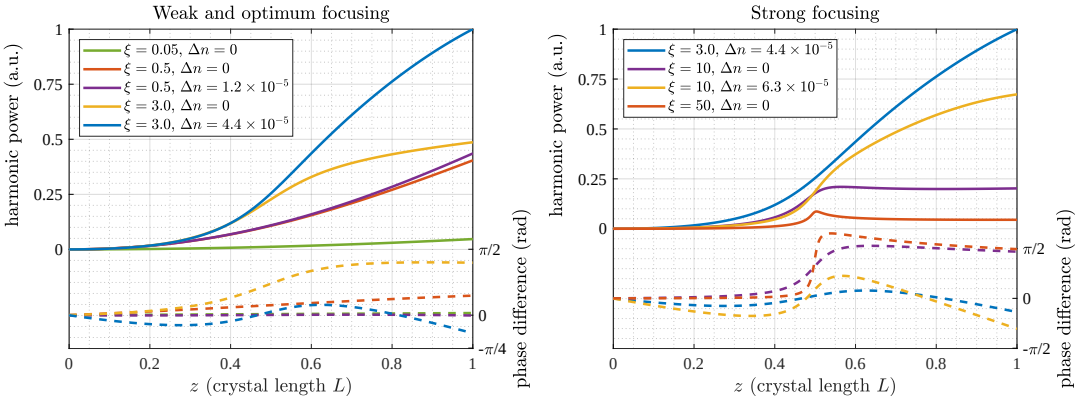

Figure 4.3: Numerical simulation of the SHG pumped by the $TEM_{0,0}$ mode for different focusing parameters ξ and wavevector mismatches Δn [HVW20b]. The waist is located at the centre of the crystal. The solid lines refer to the left y axis and show the accumulated harmonic power. The dashed lines refer to the right y axis and illustrate the phase difference between the harmonic field and the excited harmonic field for the harmonic $TEM_{0,0}$ mode.

phase matchings with $|\Delta\alpha_{0,0}| \approx 0$ through the crystal can be achieved with an appropriate wavevector mismatch. The compensation with the wavevector mismatch works, if needed at all, because only the linear part of the arctangent is relevant within the crystal. The good phase matching can, however, not compensate for the small pump intensity which is the main limiting factor in this regime.

2. *Above optimum focusing*
   According to Figure 4.2, strong focusing implies a strong divergence of the pump field such that significant conversion only occurs around the waist at the crystal centre. There, the extremely high pump intensity could theoretically still result in higher conversion efficiencies assuming the crystal is not damaged.
   However, the strong focusing also implies a steep slope in the $\operatorname{atan}(z/z_R)_{z=0}$ term. Around the waist, this term increases the phase difference up to the range where the accumulated harmonic power remains constant or even decreases. It cannot be properly compensated by the wavevector mismatch, anymore, because the wavevector mismatch is linear in z while the nonlinear part of the arctangent is now relevant within the crystal. The phase matching is the main limiting factor in this regime.

3. *Optimum focusing*
   The optimum focusing regime provides the best trade-off of the above mentioned limitations. The pump intensity is relatively high in the whole crystal, even though it is smaller around the waist than in the strong focusing regime and potentially smaller far from the waist than in the weak focusing regime. A phase matching as good as in the weak focusing regime is not possible due to the nonlinear part of the arctangent which cannot be perfectly compensated by the wavevector mismatch. But the phase difference can still be kept in the range where the interference is rather constructive. Hence, the highest conversion efficiency is achieved.

$LG_{3,3}$ single-pass SHG

The $LG_{3,3}$ mode excites the harmonic modes $LG_{0,6}$, $LG_{2,6}$, $LG_{4,6}$ and $LG_{6,6}$, and the achievable conversion efficiencies are fundamentally smaller than for the $TEM_{0,0}$ mode for the same focusing due to the more uniform intensity distribution which leads to a smaller pump intensity and thus $\mathcal{C}_{3,3}(z) < \mathcal{C}_{0,0}(z)$. This argument already holds if only the total harmonic power, i.e. the sum over all four excited harmonic modes, is considered. If the excited harmonic modes are analysed individually, their conversion efficiencies are additionally smaller because $c'_{p',6} < c'_{0,0}$ and $\Delta\gamma_{3,3,p',6} \geq \Delta\gamma_{0,0,0,0}$ as shown in Table 4.1. Figure 4.4 presents a simulation of the accumulated total harmonic power and the individually accumulated harmonic powers in the excited modes in relation to their individual phase differences for the same settings as in the $TEM_{0,0}$ case except for $\xi = 50$.

Table 4.1: Composition of the harmonic field excited by the $LG_{3,3}$ mode.

p', l'	$\lvert c'_{p',l'}\rvert^2$	$\Delta\gamma_{3,3,p',l'}$
0,6	0.2129	13
2,6	0.1342	9
4,6	0.1610	5
6,6	0.4919	1

Again, a more detailed description can be found in [HVW20b]. In the following, the main aspects and differences to the $TEM_{0,0}$ mode are summarised:

1. *The harmonic $LG_{6,6}$ mode*
   Since $\Delta\gamma_{3,3,6,6} = \Delta\gamma_{0,0,0,0} = 1$, this mode shows the same qualitative behaviour and dependence on the focusing, when pumped by the $LG_{3,3}$ mode, as the $TEM_{0,0}$ mode, when pumped by the $TEM_{0,0}$ mode. Hence, the optimum focusing would be $\xi = 2.84$. Its individual conversion efficiency is, however, significantly smaller due to the lower pump intensity and $|c'_{6,6}|^2 \approx 0.5 < 1 = |c'_{0,0}|^2$.

2. *The harmonic $LG_{0,6}$, $LG_{2,6}$ and $LG_{4,6}$ mode*
   Already in the weak focusing regime, the individual conversion efficiencies of these modes are smaller than the one of the $LG_{6,6}$ mode because, for them, $|c'_{p',6}|^2 < |c'_{6,6}|^2$. If the focusing additionally gets stronger, their larger $\Delta\gamma_{3,3,p',6}$ values further reduce their efficiencies compared to the $LG_{6,6}$ mode because the Gouy phase leads to completely destructive interferences and a maximum power decrease. A wavevector mismatch can still slightly improve the efficiency for the $LG_{4,6}$ which has a sufficiently small $\Delta\gamma_{3,3,p',6}$ value. For the $LG_{0,6}$ and $LG_{2,6}$ mode, the effect of the simulated wavevector mismatches is, however, insignificant.

3. *The total harmonic output field*
   The harmonic output field is given by the superposition of the four excited modes at $z = L$ (refering to the figure axis). The relations of their individually accumulated harmonic power at $z = L$ shows that the harmonic output field depends on the focusing, as well. The $LG_{6,6}$ mode is always dominating but the contributions of the other three modes are smallest around optimum focusing and larger in the very weak and very strong focusing regime.

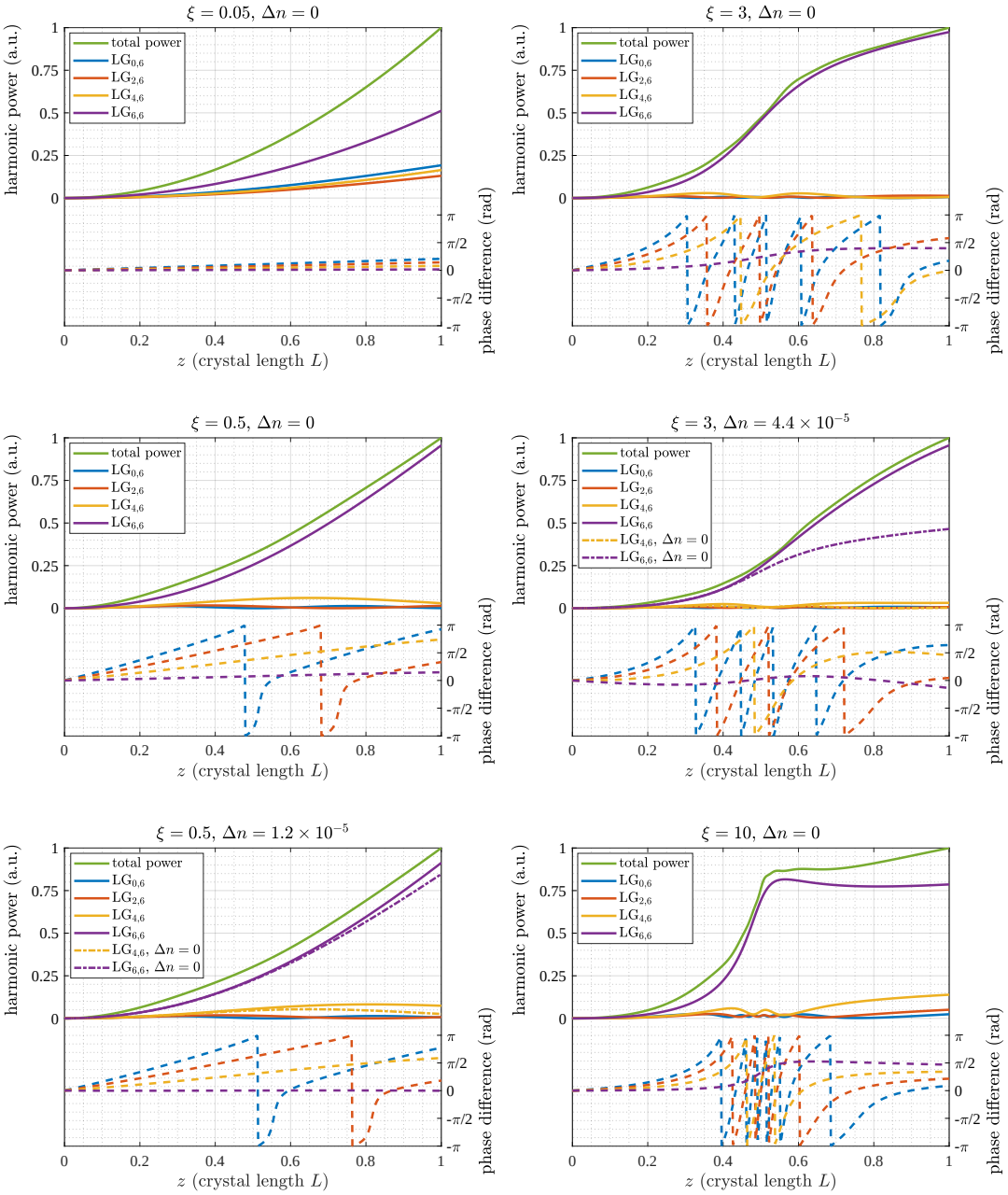

Figure 4.4: Numerical simulation of SHG pumped by the $LG_{3,3}$ mode for different focusing parameters ξ, and wavevector mismatches Δn [HVW20b]. The waist is located at the centre of the crystal. The solid lines refer to the left y axis and show the accumulated harmonic power. The dashed lines refer to the right y axis and illustrate the phase difference between the respective mode in the harmonic field and the excited harmonic field.

Conclusion for the single-pass simulations

The general ability of a pump mode to interact with a nonlinear medium and to generate a harmonic field depends on its intensity distribution and can be quantified by a pump-mode dependent effective nonlinearity $d_{p,l}$ (see Eq. 4.16). The ratio $d_{3,3}/d_{0,0} \approx 0.4$ means that the $LG_{3,3}$ mode only generates $0.4^2 \approx 1/7$th of the harmonic power which the $TEM_{0,0}$ mode generates in a finitely small segment of the nonlinear medium. This factor becomes potentially even smaller if the conversion along the whole crystal is considered. Except for the limit of plane waves, three of the four harmonic modes excited by the $LG_{3,3}$ mode will then have a significantly worse phase matching than the $TEM_{0,0}$ mode. Especially around the optimum focusing regime where the $LG_{6,6}$ mode clearly dominates the harmonic $LG_{3,3}$ output field, the factor thus reduces to $\left(d_{3,3}c'_{6,6}/d_{0,0}\right)^2 \approx 1/14$. Here, $d_{3,3}$ can be understood as weighted by the mode contributions in the final harmonic output field. This is illustrated in Figure 4.5 where the factor still remains at roughly $1/7$ for $\xi = 0.05$ but is close to $1/14$ for all other cases.

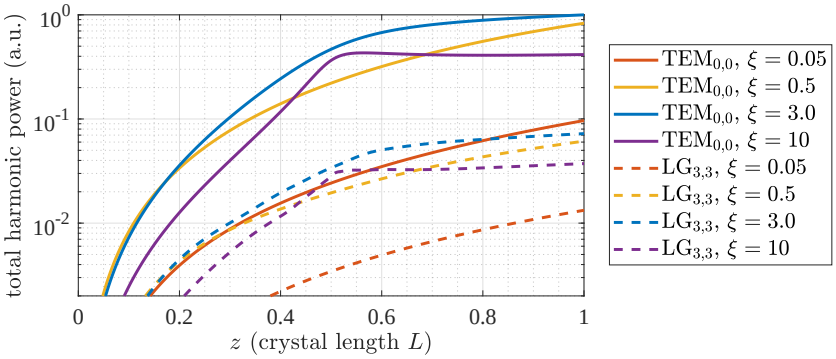

Figure 4.5: Comparison of the accumulated total harmonic power for different focusing parameters ξ and no wavevector mismatch ($\Delta n = 0$) [HVW20b]. The solid and dashed lines refer to the $TEM_{0,0}$ and $LG_{3,3}$ mode, respectively. The data are normalised to the final harmonic power of $TEM_{0,0}$, $\xi = 3$.

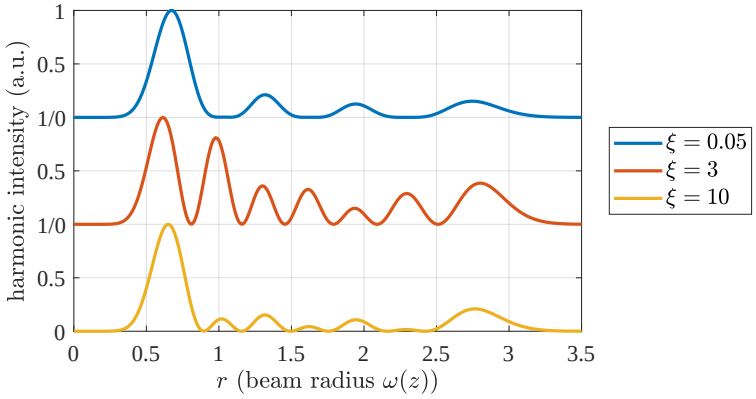

Figure 4.6: Normalised final harmonic intensity distribution in the far-field ($z = 100z_R$) for different focusing parameters ξ when pumped by the $LG_{3,3}$ mode [HVW20b].

Besides the conversion efficiencies, the dependence of the harmonic output field on the focusing is another important difference. While the $TEM_{0,0}$ mode only excites the harmonic $TEM_{0,0}$ mode, the harmonic $LG_{3,3}$ output field is a focusing-dependent

superposition of four modes (see Fig. 4.6). In the weak focusing regime, their relation roughly remains constant through the crystal and is more or less equal to $LG_{3,3}^2$ (compare with Fig. 4.1). In the optimum focusing regime, the harmonic output field can be approximated by the harmonic $LG_{6,6}$ mode. In the strong focusing regime, where the $LG_{6,6}$ mode has a significantly worse phase matching, the output field is a mixture of the two others.

The optimum choice of ξ for the single-pass $LG_{3,3}$ SHG depends on the goal. High conversion efficiencies require a focusing parameter close to 2.84 as for the $TEM_{0,0}$ mode. However, in this focusing regime, the harmonic modes $LG_{0,6}$, $LG_{2,6}$ and $LG_{4,6}$ are strongly suppressed in the harmonic field. If the goal is to obtain a harmonic output field with a good balance between all excited harmonic modes, the weak focusing regime is better suited. So far, this shall be understood as a general rule. The criteria which have to be fulfilled by the SHG as part of a higher-order mode squeezed light source require the theory outlined in Section 5.1.

4.1.3 Double-pass and cavity-enhanced configuration

This section will simulate the SHG in a cavity configuration equal to the design of the experiment in Section 4.2 to allow for a direct comparison between the simulation and the experimental measurements. In this experiment, the SHG is enhanced in a linear hemilithic cavity with $\xi \approx 0.5$ which is formed by an incoupling mirror and a curved end face of a nonlinear crystal (see Fig. 4.7). While the crystal end face is highly reflective for both the fundamental and harmonic wavelength, the incoupling mirror only reflects light at the fundamental wavelength to resonantly enhance the pump power. It does not reflect light at the harmonic wavelength such that the harmonic field does not resonate and is effectively generated in a double-pass configuration through the crystal. As in the single-pass configuration, the relative simulation results are again independent of the pump power; hence, its resonant enhancement can be ignored and the double-pass simulation can directly be applied to this specific cavity design. Furthermore, the pump field can still be approximated as undepleted even though conversion efficiencies close to 1 are possible and were achieved in the experiment. At this level of conversion efficiency, the simulated cavity has a power buildup factor of about 40 such that the circulating intra-cavity field is still only depleted by about 2.5 %.

The main difference of the double-pass simulation to the single-pass is that the fundamental and harmonic field usually experience different phase shifts under the reflection off the crystal end face. The phase shift values of the used crystal as indicated by Laseroptik GmbH are $\phi_{1064\,\mathrm{nm}} = 29.1^\circ$ and $\phi_{532\,\mathrm{nm}} = 1.3^\circ$ and their effect can be identified in Figure 4.7 as jumps in the phase difference by $2\phi_{1064\,\mathrm{nm}} - \phi_{532\,\mathrm{nm}} \approx \pi/3$ at $z = L$ (refering to the figure axis).

The accumulated harmonic power and phase differences in the simulation of the $LG_{3,3}$ double-pass follow the same rules as explained in Section 4.1.2. An additional simulation of the $TEM_{0,0}$ is omitted because it would again be qualitatively identical to the conversion from the $LG_{3,3}$ to the harmonic $LG_{6,6}$ mode. The double-pass simulation with $\xi \approx 0.5$ and without a wavevector mismatch predicts that the $LG_{6,6}$ mode dominates the harmonic output field by about 95 % and the same can be concluded for the assumed SHG cavity. As in the single-pass case, similar results apply to the regime around optimum focusing with $\xi \approx 3$ and if a wavevector mismatch is included. Hence, the ratio of the pump-mode dependent effective nonlinearities $d_{0,0}/d_{3,3}$, weighted by the mode contributions in the final harmonic output field

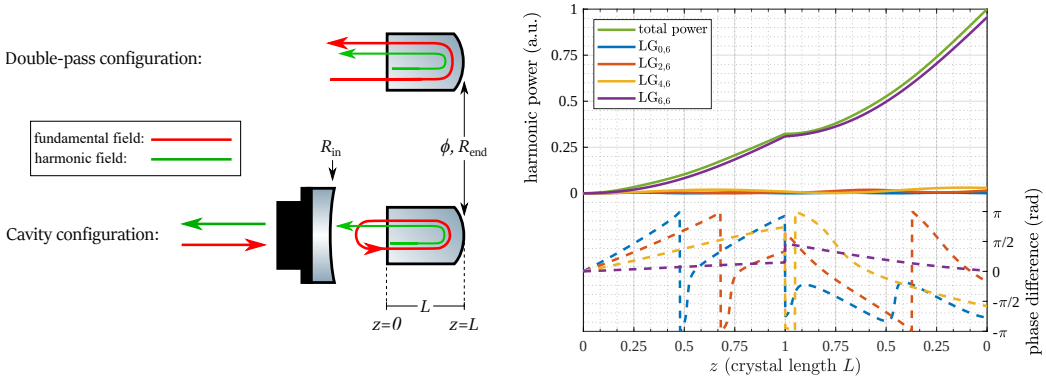

Figure 4.7: Left: Schematic of the double-pass and cavity configuration. In both cases, the crystal end face acts as the (cavity end) mirror. Right: Numerical simulation of a double-pass SHG pumped by the $LG_{3,3}$ mode for $\xi = 0.5$ and $\Delta n = 0$. The waist is located at the centre of the crystal. The solid lines refer to the left y axis and show the accumulated harmonic power. The dashed lines refer to the right y axis and illustrate the phase difference between the respective mode in the harmonic field and the excited harmonic field (based on [HVW20b]).

(see conclusion of previous section), is close to 3.77 where the exact value in an experiment will slightly differ due to a wavevector mismatch and the exact focusing parameter.[4]

These results and predictions are based on the assumption of equal $TEM_{0,0}$ and $LG_{3,3}$ pump power. For the cavity configuration, this refers to an equal circulating intra-cavity pump power. An equal intra-cavity pump power will, however, be achieved at different injected pump powers for the following reason. The same injected pump power leads to different double-pass conversion efficiencies due to the discussed fundamental differences in the $TEM_{0,0}$ and $LG_{3,3}$ mode SHG. The double-pass conversion efficiency, however, determines the intra-cavity loss of the fundamental field, thereby affecting the impedance matching of the cavity and the circulating pump power. Hence, the double-pass simulation is not sufficient to make practical predictions for the cavity configuration because, in the experiment, the injected pump power is measured rather than the intra-cavity power.

For practical predictions, the conversion efficiency can be simulated with respect to the injected pump power by the Non-Linear Cavity Simulator [Las10] given the cavity parameters of the experiment: $\lambda_1 = 1064\,\mathrm{nm}$, $n = 2.23$ (nominal refractive index for 7 % doped MgO:$LiNbO_3$), $\Delta n = 0$, $R_{end} = 0.999$ (at both wavelengths), $R_{in,1064\,nm} = 0.98$, $R_{in,532\,nm} = 0$, $L = 6.5\,\mathrm{mm}$ (geometric crystal length), $w_0 = 31.4\,\mu\mathrm{m}$ (pump waist size corresponding to $\xi = 0.5$) and $d_{eff} = 3\,\mathrm{pm\,V^{-1}}$ (typical effective nonlinearity for 7 % doped MgO:$LiNbO_3$). The $TEM_{0,0}$ and $LG_{3,3}$ mode can then be compared by setting $d_{eff,0,0} = d_{eff}$ and $d_{eff,3,3} = d_{eff,0,0}/3.7$ given the double-pass result that the $LG_{6,6}$ mode is dominating the harmonic $LG_{3,3}$ output field. The result of this simulation is shown in Figure 4.8. The assumption $d_{eff,0,0}/d_{eff,3,3} = 3.7$ translates into a factor of $3.7^2 \approx 14$ between the injected $TEM_{0,0}$ and $LG_{3,3}$ pump power where the same conversion efficiency is reached.

[4] The ratio is only independent of the focusing parameter in a finitely small segment of the crystal, i.e. without the influence of phase matching.

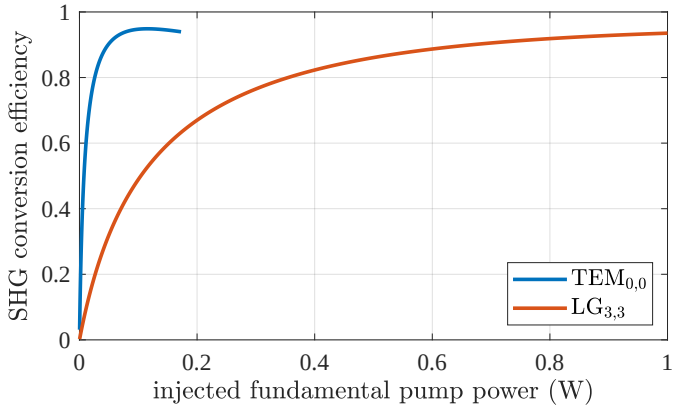

Figure 4.8: Numerical simulation of a cavity-enhanced SHG pumped by the $TEM_{0,0}$ and $LG_{3,3}$ mode for $\xi = 0.5$, $\Delta n = 0$ and $d_{\text{eff},0,0}/d_{\text{eff},3,3} = 3.7$ [HVW20b].

Conclusion for the cavity-enhanced simulation

A linear SHG cavity in which the harmonic field is not resonating can be treated as a double-pass configuration with enhanced pump power, and the main difference to the single-pass configuration is a jump in the phase difference at the reflection off the cavity end mirror. In the double-pass configuration, the conversion follows the same rules as outlined for the single-pass. In the focusing regime of $\xi \sim 0.5$ to 3 which the focusing parameter of the experiment in Section 4.2 can also be counted to, the $LG_{6,6}$ mode is predicted to dominate the harmonic $LG_{3,3}$ output field by roughly 95 % which then depends on the exact wavevector mismatch and focusing parameter. Inserting the double-pass results into the Non-Linear Cavity Simulator shows that the predicted ratio of $d_{0,0}/d_{3,3} \approx 3.7$ implies that the $LG_{3,3}$ mode requires about 14 times the injected pump power in comparison to the $TEM_{0,0}$ to achieve the same conversion efficiency.

4.2 Experiment

On the one hand, the goal of this experiment was to compare the conversion efficiencies of the $TEM_{0,0}$ and $LG_{3,3}$ mode in the same SHG cavity, and to measure their harmonic output fields in order to test the predictions from Section 4.1. Since the predictions on the conversion efficiencies mainly refer to the pump-mode dependent effective nonlinearities $d_{0,0}$ and $d_{3,3}$, which cannot directly be measured, the experimental data are compared to simulation results computed with the Non-Linear Cavity Simulator (NLCS) [Las10]. In this way, $d_{p,l}$ can be derived as a fitting parameter. On the other hand, a second goal was to investigate the influence of astigmatism on the conversion efficiency and on the harmonic output field of the $LG_{3,3}$ mode.

4.2.1 Setup

Figure 4.9 shows the experimental setup which allows to compare the second harmonic generation of the $TEM_{0,0}$ and $LG_{3,3}$ mode in the same SHG cavity. A non-planar ring laser (NPRO), which is protected against back-reflections by a Faraday isolator (FI), continuously emits light in the $TEM_{0,0}$ mode at a wavenlength of 1064 nm with an optical power of about 2 W. Then, two removable mirrors enable the switching between the $TEM_{0,0}$ and $LG_{3,3}$ operation. In the latter case, the beam propagates along the upper path where it is partly converted into the $LG_{3,3}$

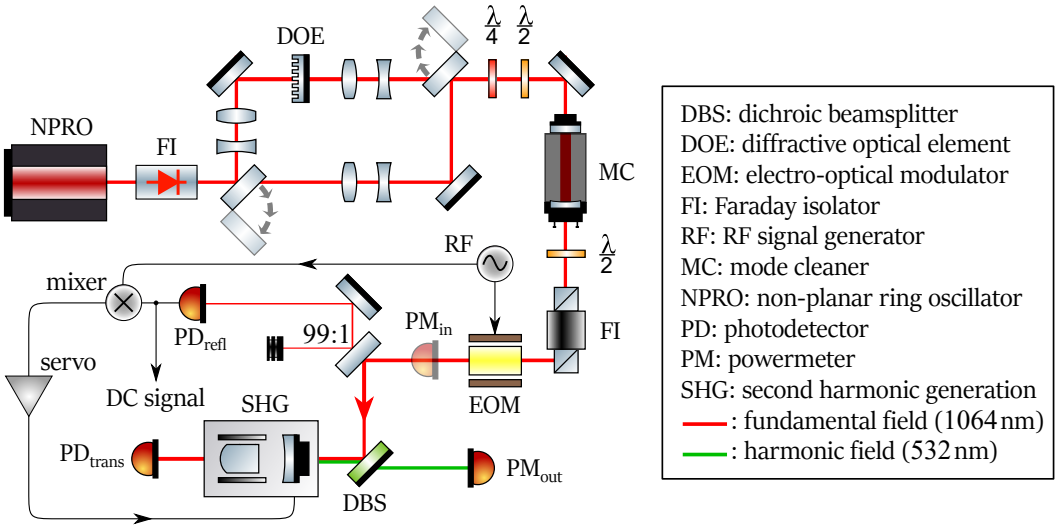

Figure 4.9: Schematic of the experimental setup (based on [HVW20a]). Two removable mirrors can switch between the $TEM_{0,0}$ and $LG_{3,3}$ operation. The mode-filtered pump field is coupled into the SHG cavity, the power is set via the right Faraday isolator and half-wave plate. Injected, reflected and transmitted fundamental power and the harmonic output power are measured by photodetectors and powermeters to infer the conversion efficiency and to correct for the effective pump mode matching. The SHG cavity length is stabilised via the Pound-Drever-Hall scheme. Not shown: electronics for the length stabilisation of the MC cavity.

mode by a diffractive optical element (DOE) (see also "Higher-order mode generation with a phase plate" in Sec. 2.3.3). The used DOE requires an incoming waist size of 3.5 mm; hence, the beam is first collimated with two lenses, accordingly. For the $TEM_{0,0}$ operation, the lower beam path is used. Since the beam radii evolve differently in the two beam paths, two individual sets of lenses are used for the mode matching of the beam to the corresponding eigenmode of the mode-cleaner cavity[5] (MC). Downstream the sets of lenses, the beam paths are recombined and a quarter- and half-wave plate set the electric field to s-polarisation.

The MC cavity is used to obtain a pure pump mode for the SHG, as described in Sec. 2.3.3, and its length is stabilised via the Pound-Drever-Hall (PDH) scheme [Bla01], accordingly (electronics not shown in Fig. 4.9). The subsequent Faraday isolator provides the proper polarisation for the SHG (s-polarisation), prevents optical cross-talk between the MC and SHG cavities and controls the SHG pump power in combination with the half-wave plate. Next, an electro-optical modulator (EOM), driven at a radio frequency (RF) of about 120 MHz, modulates the phase of the electric field for the length stabilisation of the SHG cavity, again using the PDH scheme. The corresponding error signal is generated by demodulating the signal from the photodetector PD_{refl} in reflection of the SHG cavity at the pick-off behind a mirror with a transmission of 1 %. Downstream from the EOM, the pump power can be measured with a portable powermeter (PM_{in}) and the pump field is then coupled into the SHG cavity which is stabilised to the resonance condition of the respective pump mode. PD_{trans} and PM_{out} measure the transmitted fundamental and harmonic output power, respectively. A dichroic beamsplitter (DBS) separates the harmonic field from the incoming fundamental pump field.

Figure 4.10 shows the hemilithic SHG cavity which is formed by the incoupling

[5] Finesse of about 300, linewidth (full width at half maximum) of about 2.3 MHz.

mirror and the curved face of the 7 % doped MgO:$LiNbO_3$ crystal, which measures $2.0 \times 2.5 \times 6.5\,\mathrm{mm}$ in x, y and z (propagation) direction, respectively. The reflectivities for the fundamental field are $R_{\mathrm{in},1064\,\mathrm{nm}} = 98.2\,\%$ (measured) and $R_{\mathrm{end},1064\,\mathrm{nm}} > 99.96\,\%$ (nominal) at the incoupling mirror and curved crystal face, respectively. For the harmonic field, the nominal values are $R_{\mathrm{in},532\,\mathrm{nm}} < 0.2\,\%$ and $R_{\mathrm{end},532\,\mathrm{nm}} = 99.9\,\%$. The plane crystal face is coated anti-reflective for both wavelengths and the radii of curvature are $R_{c,\mathrm{in}} = 25\,\mathrm{mm}$ and $R_{c,\mathrm{end}} = 12\,\mathrm{mm}$, setting the waist of the fundamental field's eigenmodes to about 30 µm in radius near the crystal centre. This corresponds to a focusing parameter of $\xi \approx 0.5$ (compare with Sec. 4.1). A peltier element stabilises the crystal temperature via a control loop for a maximum SHG conversion efficiency, i.e. phase matching (see Sec. 3.2.2), at each level of pump power.

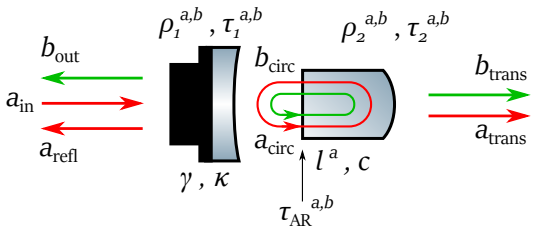

Figure 4.10: The hemilithic SHG cavity (based on [HVW20a]). The allocated parameters are used in Eqs. 4.17 and 4.18. b_{trans} is assumed to be negligible, the Peltier element is omitted.

4.2.2 Correcting for an imperfect pump mode matching

The *external* conversion efficiency $\eta_{\mathrm{ext}} = P_{\mathrm{out}}/P_{\mathrm{in}}^{\mathrm{ext}}$ indicates how much of the injected fundamental pump power is converted into the harmonic output field and can easily be measured with $\mathrm{PM}_{\mathrm{in}}$ and $\mathrm{PM}_{\mathrm{out}}$. However, an imperfect mode matching of the pump field to the corresponding SHG cavity eigenmode results in a fraction of the injected pump power which is not resonating in the stabilised SHG cavity but reflected even if the cavity is impedance-matched. Additionally, astigmatism can alter the cavity eigenmodes, especially the Laguerre-Gaussian ones (see Sec. 2.3.3), and further reduce the effective pump mode matching. The effectively used pump power is thus smaller than $P_{\mathrm{in}}^{\mathrm{ext}}$. It is reasonable to expect that this effect is not significant for the $\mathrm{TEM}_{0,0}$ case as mode matchings close to 100 % are feasible and since this mode can resonate in an astigmatic cavity. In the higher-order $\mathrm{LG}_{3,3}$ case, however, this effect is potentially much stronger due to astigmatism and also due to a higher sensitivity to spatial mismatches (see Sec. 2.3.3). Hence, the $\mathrm{LG}_{3,3}$ SHG conversion efficiency is likely to be significantly below of what is theoretically possible.

$\eta_{\mathrm{cor}} = P_{\mathrm{out}}/P_{\mathrm{in}}^{\mathrm{mat}}$ will be the *corrected* conversion efficiency which corrects the pump power in terms of the effective pump mode matching. Here, the *matched* fraction of the pump power is defined as $P_{\mathrm{in}}^{\mathrm{mat}} = |\kappa|^2 P_{\mathrm{in}}^{\mathrm{ext}}$ where the coupling coefficient $|\kappa|^2$ is the absolute value squared of the spatial overlap integral between the injected pump field and the resonating SHG cavity eigenmode. In the $\mathrm{TEM}_{0,0}$ case, $|\kappa|^2$ can directly be inferred from the transmission spectrum measured by $\mathrm{PD}_{\mathrm{trans}}$ while the length of the SHG cavity is scanned. This holds under the assumption that the transmission spectrum is not significantly affected by conversion during the length scan in which case the pump field would not properly build up. For the $\mathrm{TEM}_{0,0}$ mode, $|\kappa|^2 = 97.5(15)\,\%$ was measured independent of the pump power.

Inferring $|\kappa|^2$ in the $\mathrm{LG}_{3,3}$ case is more difficult. The level of astigmatism does not only depend on the mirror geometries of the SHG cavity but also on the microscopic crystal structure which is especially affected by any kind of heat impact (see Figure 4.11). On the one hand, this implies that the crystal temperature should not be adjusted to solely optimise the phase matching, as in the $\mathrm{TEM}_{0,0}$ case, but needs

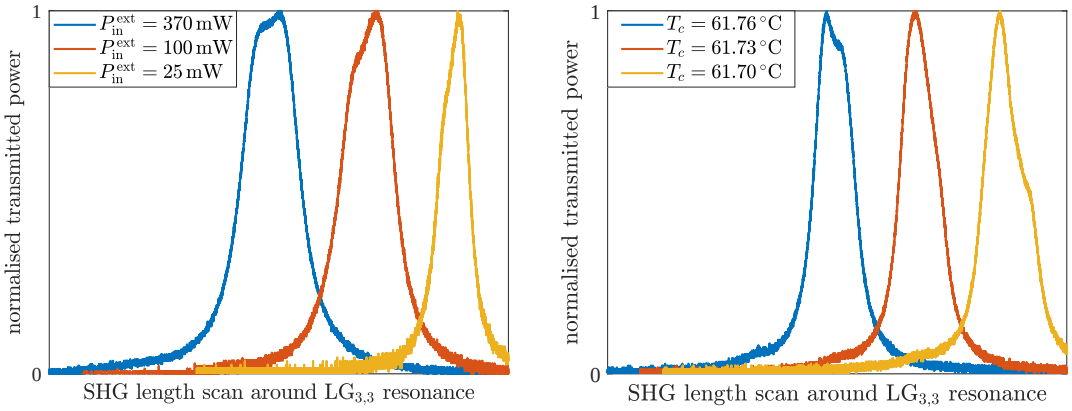

(a) Crystal temperature: $T_c = 61.73\,°C$. (b) Injected pump power: $P_{in}^{ext} = 100\,mW$.

Figure 4.11: Resonance peak of the injected $LG_{3,3}$ pump mode in the SHG cavity in terms of the transmitted power while the SHG cavity length is scanned. The deformation of the resonance peak is a measure for the astigmatism of the cavity. (a) demonstrates the influence of the pump power P_{in}^{ext} for a constant crystal temperature, while (b) demonstrates the influence of the crystal temperature T_c for a constant pump power. All of the peaks are normalised. The x axis of each individual peak measurement was adjusted for a clear figure.

to optimise the trade-off between maximum phase matching and minimum astigmatism. On the other hand, the astigmatism during the SHG length scan is likely to be different than the relevant astigmatism when the SHG length is stabilised, because the resonantly enhanced pump field leads to a higher absolute absorption in the crystal than during the length scan. Hence, the $LG_{3,3}$ measurement required a more elaborate scheme to infer $|\kappa|^2$ and η_{cor}.

While the SHG cavity is stabilised, PD_{trans} and PM_{out} measure the transmitted fundamental power P_{trans} (the transmitted harmonic power is negligible) and the harmonic output power P_{out}, respectively, while the reflected fundamental power P_{refl} can be inferred from the DC signal of PD_{refl}.[6] For each level of pump power, these three values can be inserted into the corresponding steady-state equations of the SHG cavity for the power reflection coefficient r_{refl} of the fundamental field, the power transmission coefficient r_{trans} of the fundamental field and η_{ext}. This set of three equations can then be solved for the single-pass power absorptions coefficient l^a of the fundamental field, the single-pass power conversion coefficient c, and the parameter of interest $|\kappa|^2$:

$$\begin{aligned} r_{refl} &:= \frac{P_{refl}}{P_{in}^{ext}} = 1 - \gamma\,|\kappa|^2 = 1 - \left[1 - |a_{refl}(l^a, c)|^2\right] |\kappa|^2 \\ r_{trans} &:= \frac{P_{trans}}{P_{in}^{ext}} = |a_{trans}(l^a, c)|^2\,|\kappa|^2 \\ \eta_{ext} &:= \frac{P_{out}}{P_{in}^{ext}} = |b_{out}(l^a, c)|^2\,|\kappa|^2 \end{aligned} \tag{4.17}$$

[6] P_{refl} is given by the ratio of the signal when the SHG cavity is stabilised to the maximum signal when its length is scanned, where the latter is equal to P_{in}^{ext}.

with

$$
\begin{aligned}
a_{\mathrm{refl}}(l^a, c) &= \rho_1^a - \frac{(\tau_1^a)^2(\tau_{\mathrm{AR}}^a)^2\rho_2^a(1-l^a-c)}{1-\rho_1^a\rho_2^a(\tau_{\mathrm{AR}}^a)^2(1-l^a-c)} \\
a_{\mathrm{trans}}(l^a, c) &= -\frac{\tau_1^a\tau_2^a\tau_{\mathrm{AR}}^a\sqrt{1-l^a-c}}{1-\rho_1^a\rho_2^a(\tau_{\mathrm{AR}}^a)^2(1-l^a-c)} \\
b_{\mathrm{out}}(l^a, c) &= -\frac{\tau_1^a\tau_{\mathrm{AR}}^a\tau_{\mathrm{AR}}^b\sqrt{c\left((\rho_2^b)^2+(1-l^a-c)(\rho_2^a)^2\right)}}{1-\rho_1^a\rho_2^a(\tau_{\mathrm{AR}}^a)^2(1-l^a-c)}
\end{aligned}
\tag{4.18}
$$

where γ is the power reflection coefficient due to the impedance condition of the SHG cavity; ρ and τ are amplitude reflection and tranmission coefficients, respectively; 1, 2 and AR refer to the incoupling mirror, crystal end face, and anti-reflective-coated crystal face, respectively; and a and b refer to the fundamental and harmonic field, respectively. These allocations are illustrated in Figure 4.10. The absorption and conversion of the fundamental field are assumed to be equal for both passes through the crystal during one roundtrip in the SHG cavity because the fundamental field is nearly undepleted after the first pass. Furthermore, the absorption of the harmonic field is neglected. The transmission and reflection coefficients of the incoupling mirror were measured separately and those of the crystal were taken as indicated from the manufacturer. In Equations 4.17 and 4.18, the uncertainty of the nominal value for ρ_2^a has the largest impact on the result for $|\kappa|^2$, and the uncertainty in the corrected conversion efficiency η_{cor} is in the order of $\pm 10\,\%$.

4.2.3 Results

The results are shown in Figure 4.12, where the x axis refers to $P_{\mathrm{in}}^{\mathrm{ext}}$ or $P_{\mathrm{in}}^{\mathrm{mat}}$ in case of the external and corrected conversion efficiency (left y axis), respectively. The conversion efficiency of the $\mathrm{TEM}_{0,0}$ mode reached a maximum of $\eta_{\mathrm{ext}} = 95.69(11)\,\%$ at $P_{\mathrm{in}}^{\mathrm{ext}} \approx 80\,\mathrm{mW}$ which is corrected to a maximum of $\eta_{\mathrm{cor}} = 98.7(15)\,\%$ at $P_{\mathrm{in}}^{\mathrm{mat}} \approx 78\,\mathrm{mW}$ using $|\kappa|^2 = 97.5(15)\,\%$. The steep increase within the pump power range below the maximum and the slow decrease above it, which both the external and corrected curves show, can be explained as follows: the impedance matching condition of the SHG cavity with respect to the fundamental pump field is given by the transmissivity coefficients of the incoupling mirror and curved crystal face as well as by the intra-cavity "losses" due to absorption and conversion. In general, the SHG cavity is highly over-coupled because the transmission through the curved crystal face is close to zero. Hence, a fraction of the injected pump field is effectively reflected by the SHG cavity even if the pump field is well mode-matched. However, the intra-cavity conversion increases with increasing pump power such that the SHG cavity transitions towards being impedance-matched. Consequently, less pump power is reflected and the external conversion efficiency approaches a maximum. If the pump power is further increased, the SHG cavity eventually transitions to being under-coupled and the external conversion efficiency decreases again.

In the $\mathrm{LG}_{3,3}$ case, the conversion efficiency reached a maximum of $\eta_{\mathrm{ext}} = 45.1(2)\,\%$ at $P_{\mathrm{in}}^{\mathrm{ext}} \approx 664\,\mathrm{mW}$ which corresponds to a harmonic output power of about 300 mW and is corrected to $\eta_{\mathrm{cor}} = 72(7)\,\%$ at $P_{\mathrm{in}}^{\mathrm{mat}} = 420(40)\,\mathrm{mW}$ using Equations 4.17 and 4.18. The corresponding values for $|\kappa|^2$ are also displayed in Figure 4.12, refering to the right y axis, and decrease from $0.71(11)$ to $0.63(6)$. Despite the large uncertainty, it is reasonable to assume that the coupling coefficient, and thus the effective pump mode matching, actually decreased with increasing pump

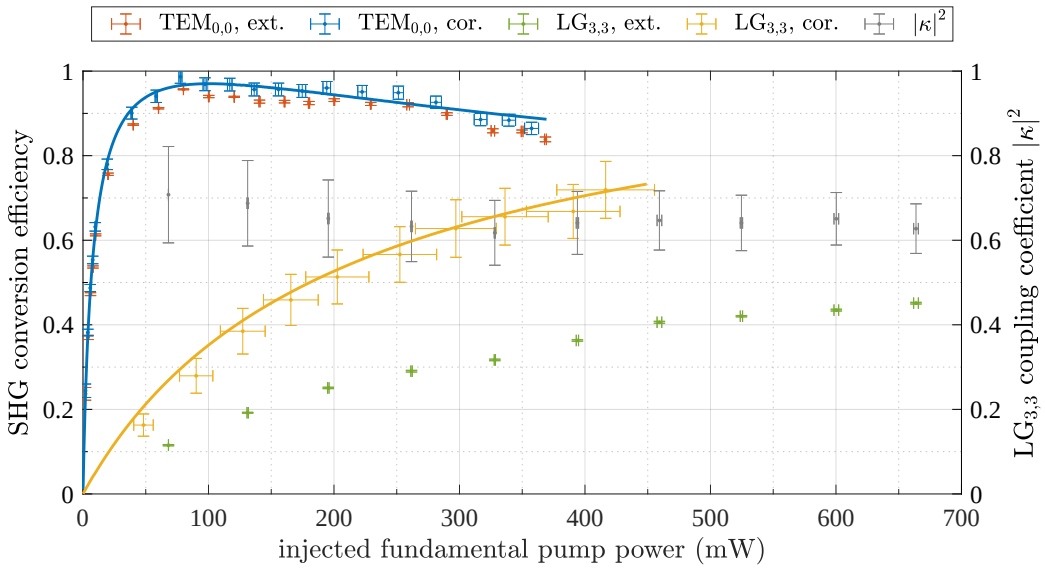

Figure 4.12: Measured external and corrected SHG conversion efficiencies (left y axis) of the $TEM_{0,0}$ and $LG_{3,3}$ mode, including the NLCS simulations for the corrected curves as solid lines (based on [HVW20a]). The x axis refers to the measured input power $P_{\text{in}}^{\text{ext}}$ in case of the external efficiencies as well as the coupling coefficient $|\kappa|^2$ (right y axis), and to the estimated matched pump power $P_{\text{in}}^{\text{mat}}$ in case of the corrected efficiencies.

power. This evolution correlates with a flattening of the external conversion efficiency curve which seems to approach a maximum around 50 % rather than close to 100 %. Another indication for a true decrease in $|\kappa|^2$ is the harmonic output field which is shown in Figure 4.13 for an injected pump power of about 130 mW and 660 mW. While both output fields are clearly distorted by the astigmatism of the SHG cavity, the one at maximum pump power is even less homogenous featuring larger ring segments with almost no intensity. Hence, the larger absolute absorption of the fundamental field in the crystal at higher pump power most likely caused a stronger astigmatism leading to a smaller effective pump mode matching, a decreasing slope in the conversion efficiency and an increasing distortion of the harmonic output field.

In Figures 4.13a and 4.13b, the seven-ring intensity structure of the $LG_{6,6}$ mode, which is expected to dominate the harmonic output field, is hard to identify by eye due to the additional astigmatic structures in the inner ring. The method to estimate the $LG_{6,6}$ mode purity via one charged coupled device (CCD) picture, which was used in [HVW20a], yielded about 71 % and 64 % for the Figures 4.13a and 4.13b, respectively, but is not conclusive (see. Sec. 4.4). Before using the incoupling mirror with $R_{\text{in},1064\,\text{nm}} = 98.2\,\%$, the same measurement was, however, conducted with another incoupling mirror of $R_{\text{in},1064\,\text{nm}} = 90\,\%$ and an NPRO laser with an output power of only 1 W. This mirror results in a smaller power buildup of the pump field in the SHG cavity and only a maximum conversion efficiency of about 0.5 % for $P_{\text{in}}^{\text{ext}} = 282\,\text{mW}$ could be achieved; hence, both components were changed afterwards. But the astigmatism of the SHG cavity was apparently weaker with the 90 % mirror and Figure 4.13c clearly confirms that the harmonic output field is dominated by a mode with seven intensity rings which shows a high overlap to a theoretical $LG_{6,6}$ intensity distribution.

To derive the pump-mode dependent effective nonlinearities $d_{0,0}$ and $d_{3,3}$ from

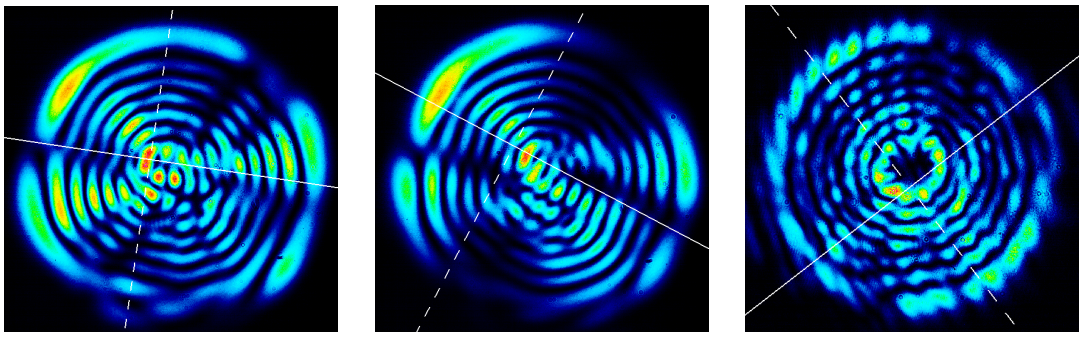

(a) Injected pump power: $P_{\text{in}}^{\text{ext}} = 130\,\text{mW}$.

(b) Injected pump power: $P_{\text{in}}^{\text{ext}} = 660\,\text{mW}$.

(c) Lower incoupling reflectivity: $R_{\text{in},1064\,\text{nm}} = 90\,\%$.

Figure 4.13: CCD pictures of the harmonic SHG output field when pumped by the $\text{LG}_{3,3}$ mode. For (a) and (b), the incoupling reflectivity was $R_{\text{in},1064\,\text{nm}} = 98.2\,\%$. Both pictures show the output field for different levels of pump power with distortions due to the astigmatism of the SHG cavity. The seven-ring intensity distribution of the expected $\text{LG}_{6,6}$ mode can hardly be identified conclusively. In (c), with a different incoupling mirror, the output field is less distorted and clearly shows seven intensity rings at a pump power of about 280 mW.

the measurement data, the NLCS tool [Las10] was used to simulate the corrected conversion efficiency η_{cor} as a function of the matched input power $P_{\text{in}}^{\text{mat}}$ with the parameters of the SHG cavity (solid lines in Fig. 4.12). As a free parameter, the effective nonlinearity can then be adjusted to optimise the match between the measurement data and the simulation. This procedure yielded $d_{0,0} = 2.6\,\text{pm/V}$, $d_{3,3} = 0.51\,\text{pm/V}$ and a ratio of $d_{0,0}/d_{3,3} = 5.1$ which is a factor of about 1.4 larger than $d_{0,0}/d_{3,3} \approx 3.7$ as predicted from Sec. 4.1.3. A less astigmatic SHG cavity would be required for a more significant comparison of theory and experiment in this regard.

Furthermore, the $\text{LG}_{3,3}$ measurement data revealed that the ratio r_{abs} of the power P_{abs}, which was absorbed by the crystal, to the injected power $P_{\text{in}}^{\text{ext}}$

$$r_{\text{abs}} := \frac{P_{\text{abs}}}{P_{\text{in}}^{\text{ext}}} \approx 1 - r_{\text{refl}} - r_{\text{trans}} - \eta_{\text{ext}} \tag{4.19}$$

was unexpectedly high. r_{abs} decreased from about 10 % to 2 % with increasing pump power. Still, such high values can very well be explained by Equation 4.17 with a single-pass power loss coefficient of $l^a \sim 10^{-4}$ which is reasonable for the used 7 % doped MgO:LiNbO_3 [Vah+08]. This high absorption loss in the crystal is likely to enhance the influence of the $\text{LG}_{3,3}$ pump field on the astigmatism of the crystal via heat transfer compared to the $\text{TEM}_{0,0}$ mode.

4.3 Summary

Section 4.1 described the theory behind second harmonic generation with an emphasis on higher-order spatial modes, and explained how they behave differently to the $\text{TEM}_{0,0}$ mode in a single-, double-pass and cavity-enhanced configuration via numerical simulations. The findings can be split up into two main differences. First, most higher-order modes excite several harmonic modes instead of just a single one. Due to the Gouy phase, these harmonic modes show different individual phase matchings and conversion efficiencies where the influence of the Gouy phase depends on the focusing parameter. Hence, the harmonic output field, as the final

superposition of all excited harmonic modes, depends on the focusing parameter as well. Second, higher-order modes require more pump power to achieve the same conversion efficiency as the $TEM_{0,0}$ mode in the same configuration. Their more uniform intensity distributions are a disadvantage in nonlinear processes if high efficiencies are the goal. One way to quantify this difference is to extend the effective nonlinearity of a nonlinear medium by including the influence of the used pump mode. Higher-order, and thus less efficient, pump modes can then be associated with an accordingly smaller pump-mode dependent effective nonlinearity $d_{p,l}$. For a focusing parameter regime of about 0.5 to 3 in a cavity-enhanced SHG, the simulation results for the $TEM_{0,0}$ and $LG_{3,3}$ mode predict a ratio of $d_{0,0}/d_{3,3} \approx 3.7$, independent of the nonlinear medium, and that the harmonic output field of the $LG_{3,3}$ mode consists of the $LG_{6,6}$ mode to more than 90 %.

In Section 4.2, these predictions were tested in a cavity configuration with a focusing parameter of $\xi \approx 0.5$. Conversion efficiencies of 96 % and 45 % could be achieved for the $TEM_{0,0}$ and the $LG_{3,3}$ mode, respectively. These results were especially a success because this level had not been demonstrated before for any higher-order mode [Zho+14; Cou+97]. Since the SHG cavity, nevertheless, showed to be astigmatic while the theoretical predictions assume an ideal cavity, an elaborate scheme to correct the $LG_{3,3}$ results, accordingly, had to be implemented for a reasonable comparison. A ratio of $d_{0,0}/d_{3,3} \sim 5$ was derived which agrees with the theoretical prediction within the uncertainties of the correction scheme. In a separate experiment with another SHG incoupling mirror and a weaker astigmatism, it could further be confirmed that the harmonic output field is dominated by the $LG_{6,6}$ mode as predicted.

The corrected ratio $d_{0,0}/d_{3,3} \sim 5$ implies that the $LG_{3,3}$ mode should require about 25 times the pump power compared to the $TEM_{0,0}$ mode to reach the same conversion efficiency in an ideal SHG cavity. However, this factor was in the order of 100 in the experiment due to astigmatism (compare the curves "$TEM_{0,0}$, ext" and "$LG_{3,3}$, ext" in Fig. 4.12) and would even be larger if the mode purity of the harmonic output field was taken into account. Hence, the results of this chapter second the findings of several other experiments [Bon+11; Hon+11; Sor+13] that astigmatism constitutes a huge challenge for Laguerre-Gaussian modes and their usage in high-precision applications like gravitational-wave detectors. Currently, there are no follow-up plans regarding a squeezed light source for gravitational-wave detectors in a Laguerre-Gaussian mode. Squeezed states in the $LG_{3,3}$ mode have already been generated, e.g. in [Ma+20], at low efficiency with a quantum noise reduction of about 1.2 dB.

The next chapter will turn to the more promising alternative to Laguerre-Gaussian modes and present a complete and efficient squeezed light source for Hermite-Gaussian modes.

4.4 Erratum

In [HVW20a], the output mode purity of the harmonic field with respect to the $LG_{6,6}$ mode was estimated via the intensity distribution measured by a CCD camera. If A_{out} is the output field, the CCD camera measures $|A_{\text{out}}|^2$. The idea was to approximate the output mode purity as follows:

$$\mu_{\text{out}} = \left| \int A_{6,6}^{*} A_{\text{out}} \, dxdy \right|^2 \approx \left| \int |A_{6,6}|^2 \, |A_{\text{out}}|^2 \, dxdy \right|^2 , \tag{4.20}$$

assuming that all fields and intensity distributions are normalised. Similar approaches to estimate mode purites were employed e.g. in [Ful+10] and [Car+13]. However, at least in [Ful+10], a more elaborate scheme with additional simulations was used. At the time of writing [HVW20a], we assumed that one CCD picture would suffice for a reasonable purity estimation. This method can, however, lead to large errors. These errors depend on the mode(s) which are associated with the impurity and their relative phases to the intended mode. In short, an "impurity mode" can be interpreted as a modulation of the intended mode which the CCD camera can sense if mainly the amplitude is modulated over the transverse plane (relative phase of about 0° or 180°). If mainly the phase is modulated (relative phase of about ±90°), the CCD camera will hardly sense this impurity. Simulating these errors for some LG and HG modes suggests that this problem is more severe for HG modes where an estimated purity of 98 % could already include an error of 20 % in an extreme case. The $LG_{6,6}$ mode seemed to be more robust in this regard; however, errors in the order of 20 % are still possible, especially given that the actual mode purity of the harmonic output field was only moderate in this experiment.

With this erratum, I want to clarify that the uncertainty of our method to estimate the mode purity of the harmonic output field is significantly larger than we indicated in [HVW20a]. Hence, I do not include the effective conversion efficiency in this thesis.

Chapter 5

Squeezed Light Source for Higher-Order Hermite-Gaussian Modes

This chapter is based on the publication [HWV22] and reports on the efficient generation of squeezed states of light in the Hermite-Gaussian modes $TEM_{0,0}$, $HG_{1,1}$, $HG_{2,2}$ and $HG_{3,3}$ and their characterisation with a balanced homodyne detector.

The scheme for the generation of squeezed states as outlined in Section 3.2.2 can be adapted to higher-order spatial modes in two distinct ways. In the indirect method, the squeezed states are first generated in the $TEM_{0,0}$ mode which allows for a very high efficiency [Vah+16]. Afterwards, the squeezed $TEM_{0,0}$ mode is converted into a higher-order mode. With the currently available mode conversion techniques, this step, however, adds optical loss to the squeezed field due to absorption and the partial conversion into unwanted modes [Car+13; Ast+21]. Hence, the results for this indirect method have remained below 3 dB of quantum noise reduction so far [Ma+20]. In the second method, the OPA directly generates squeezed states in a higher-order mode without the intermediate $TEM_{0,0}$ process. In practice, this method is more efficient because it does not require any spatial manipulation of the squeezed field. 5 dB in a first-order mode and 3 dB for higher mode orders have been the highest results for the direct generation of squeezing and entanglement so far [Ste+18; Guo+17; Las+06].

For this thesis, the more promising direct method has been chosen, and the next section discusses in more detail how to efficiently pump the direct generation of squeezed states in higher-order modes.

5.1 Pump field simulations for direct squeezed light generation

In general, the nonlinear process which is used in this thesis to generate squeezed states, parametric down-conversion, can be interpreted as a reversed second harmonic generation (SHG). The most important consequence is that every harmonic mode that is excited in the SHG of a given fundamental mode can, in turn, generate squeezed states in this mode. Employing this on Section 4.1, for instance, yields that an arbitrary superposition of the harmonic modes $LG_{0,6}$, $LG_{2,6}$, $LG_{4,6}$ and $LG_{6,6}$ will generate squeezing in the $LG_{3,3}$ mode. Of course, different superpositions are differently efficient and very similar considerations as for the SHG apply. This principle has already been mentioned and experimentally investigated e.g. in [Las+06] and [Guo+17], respectively. In the first article, the general possibility to pump the squeezing process of the $HG_{1,0}$ and $HG_{2,0}$ mode with several harmonic modes is

stated; nevertheless, they exclusively used the harmonic $\mathrm{TEM}_{0,0}$ mode in their experiment. In the latter article, a pump superposition of the harmonic modes $\mathrm{TEM}_{0,0}$ and $\mathrm{HG}_{2,0}$ could reduce the threshold power of a type-II optical parametric oscillator by 53.5 % compared to only using the harmonic $\mathrm{TEM}_{0,0}$ mode to generate entanglement in the $\mathrm{HG}_{1,0}$ mode. Since the threshold power corresponds to the pump power for which the highest squeezing level is obtained (in the absence of phase noise) [BK68; Las10], it can serve as a measure for the pump efficiency and should be minimised.

The article [BK68] only discusses the $\mathrm{TEM}_{0,0}$ mode and, thus, only states an equation for the $\mathrm{TEM}_{0,0}$ threshold power. This equation can, however, be generalised to an arbitrary squeezed mode. [BK68] start their calculation in Equation (3.3) where the time average power gain of the idler field ΔP_2 through the nonlinear medium is written as (Eq. (3.4) already inserted)

$$\Delta P_2 = -\mathrm{Im}\left(\frac{\omega_2}{2}\chi \int \mathbf{E}_2^*\left(\mathbf{r}\right)\mathbf{E}_1^*\left(\mathbf{r}\right)\mathbf{E}_3\left(\mathbf{r}\right)\,dV\right)\,. \tag{5.1}$$

1, 2 and 3 denote the signal, idler and harmonic field, respectively, $\mathbf{E}_{1,2,3}$ are the corresponding three-dimensional amplitude distributions and the integral is evaluated over the nonlinear medium. In the case of degenerate parametric down-conversion, the signal and idler field are degenerate and can both be described by the amplitude distribution of the squeezed field. To further keep the notation of this thesis, that 1 and 2 denote the fundamental and harmonic field and that A denotes an amplitude distribution instead of E, the following renaming can be done: $\Delta P_2 \rightarrow \Delta P_{i,s}$ where i and s denote the idler and signal field, respectively, $\omega_2 \rightarrow \omega_1$, $\mathbf{E}_{1,2} \rightarrow \mathbf{A}_{\mathrm{sqz}}$ and $\mathbf{E}_3 \rightarrow \mathbf{A}_{\mathrm{p}}$ where the subscript p denotes the pump field. Moreover, the negative imaginary part accounts for the influence of an arbitrary relative phase between the squeezed and pump field. Assuming the optimum relative phase, the negative imaginary part can be replaced by the absolute value, finally yielding

$$\Delta P_{i,s} \propto \left|\int \left[\mathbf{A}_{\mathrm{sqz}}^*\left(\mathbf{r}\right)\right]^2 \mathbf{A}_{\mathrm{p}}\left(\mathbf{r}\right)\,dV\right|\,, \tag{5.2}$$

which describes the power gain in the idler or signal field. Following the definitions of $\bar{H}$ in Equations (3.19) and (3.23), and of $\bar{h}$ in Equation (3.32) of [BK68], the spatial-mode dependence of the threshold power P_{thr} in Equation (3.34) can be generalised to

$$P_{\mathrm{thr}} \propto \left|\int \left[\mathbf{A}_{\mathrm{sqz}}^*\left(\mathbf{r}\right)\right]^2 \mathbf{A}_{\mathrm{p}}\left(\mathbf{r}\right)\,dV\right|^{-2}\,. \tag{5.3}$$

This volume integral $dV = dAdz$ can be split up into a surface integral, evaluated over the transverse plane, and a line integral, evaluated along the propagation axis. The surface integral computes the spatial overlap of the pump field to the square of the squeezed field which has to be non-zero for a finite threshold power, that is, for the generation of squeezed states. Hence, the surface integral determines which harmonic modes can generate squeezed states in a given fundamental $\mathrm{HG}_{m,n}$ mode, at all, and the general pump field can be written as an arbitrary superposition of them [Las+06]:

$$A_{\mathrm{p}}\left(\mathrm{HG}_{m,n}\right) = \sum_{k=0}^{m}\sum_{j=0}^{n} a_{2k,2j}\mathrm{HG}_{2k,2j}^{h}\,, \tag{5.4}$$

where the harmonic modes $\mathrm{HG}_{m,n}^{h}$ are denoted by the superscript h and have a reduced waist size ($w_0^h = w_0/\sqrt{2}$). According to this equation, the squeezing process

of the $HG_{m,n}$ includes $(m+1)(n+1)$ possible pump modes. More specifically, the general pump fields for the spatial modes in this thesis read

$$A_p(HG_{0,0}) = a_{0,0}HG^h_{0,0}$$

$$A_p(HG_{1,1}) = a_{0,0}HG^h_{0,0} + a_{2,0}HG^h_{2,0} + a_{0,2}HG^h_{0,2} + a_{2,2}HG^h_{2,2}$$

$$\begin{aligned} A_p(HG_{2,2}) = {} & a_{0,0}HG^h_{0,0} + a_{2,0}HG^h_{2,0} + a_{0,2}HG^h_{0,2} + a_{2,2}HG^h_{2,2} \\ & + a_{4,0}HG^h_{4,0} + a_{4,2}HG^h_{4,2} + a_{0,4}HG^h_{0,4} + a_{2,4}HG^h_{2,4} + a_{4,4}HG^h_{4,4} \end{aligned} \tag{5.5}$$

$$\begin{aligned} A_p(HG_{3,3}) = {} & a_{0,0}HG^h_{0,0} + a_{2,0}HG^h_{2,0} + a_{0,2}HG^h_{0,2} + a_{2,2}HG^h_{2,2} \\ & + a_{4,0}HG^h_{4,0} + a_{4,2}HG^h_{4,2} + a_{0,4}HG^h_{0,4} + a_{2,4}HG^h_{2,4} \\ & + a_{4,4}HG^h_{4,4} + a_{6,0}HG^h_{6,0} + a_{6,2}HG^h_{6,2} + a_{6,4}HG^h_{6,4} \\ & + a_{0,6}HG^h_{0,6} + a_{2,6}HG^h_{2,6} + a_{4,6}HG^h_{4,6} + a_{6,6}HG^h_{6,6} \,. \end{aligned}$$

The line integral in Equation 5.3, on the other hand, evaluates the phase matching between the squeezed and pump field.

Let us first assume a pump field which only consists of one of the harmonic modes from Equation 5.4. In this case, the optimum choice is the highest-order mode $HG^h_{2m,2n}$ which provides the highest spatial overlap as well as the best phase matching, thus, simultaneously maximises the surface and line integral and minimises the threshold power. This is in perfect agreement with the findings in Section 4.1 where the $LG_{3,3}$ SHG conversion was most efficient into the excited harmonic mode with the highest mode order ($LG_{6,6}$), as well. A comparison with Table 4.1 allows to associate the spatial overlap in Equation 5.3 with the c' parameter and, for both processes, a smaller difference $\Delta\gamma$ in the Gouy phase factors implies a better phase matching. $\Delta\gamma$ is always minimised and equal to 1 for the relation $HG_{m,n} \leftrightarrow HG^h_{2m,2n}$.

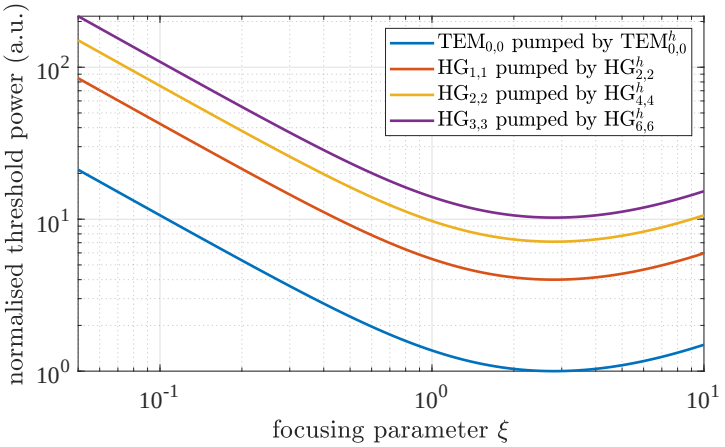

Figure 5.1: Calculated threshold power for the cases as indicated by the legend dependent on the focusing parameter. The curves are normalised to the $TEM_{0,0}$ minimum, their ratios are ξ-independent.

Figure 5.1 presents the threshold power calculated with Equation 5.3 for the $TEM_{0,0}$, $HG_{1,1}$, $HG_{2,2}$ and $HG_{3,3}$ mode, when pumped by the respective $HG^h_{2m,2n}$ mode, dependent on the focusing parameter ξ. For each value $0.05 \leq \xi \leq 10$, the

wavevector mismatch $\Delta k = 2k_{sqz} - k_p$ is optimised. The curves evolve qualitatively identically due to the identical $\Delta\gamma$ values, each having a single minimum at $\xi \approx 3$ which coincides with the focusing parameter for highest SHG conversion efficiency if $\Delta\gamma = 1$. The ratios of the curves, which result from the differently efficient pump intensity distributions and from the different spatial overlaps regarding the surface integral in Equation 5.3, amount to 4.0, 7.1 and 10.2 for the $HG_{1,1}$, $HG_{2,2}$ and $HG_{3,3}$ mode, respectively, compared to the $TEM_{0,0}$ mode. These ratios do not only imply that the threshold power of the $HG_{1,1}$ mode equals 4 times the threshold power of the $TEM_{0,0}$ mode but, generally, that the $HG_{1,1}$ mode requires 4 times the pump power in the $HG^h_{2,2}$ mode compared to the pump power the $TEM_{0,0}$ mode requires in the harmonic $TEM_{0,0}$ mode to achieve any given level of quantum noise reduction.

Proceeding from the most efficient single-mode pump field, additional modes can now be added. This will increase the spatial overlap between the pump and (square of the) squeezed field, at least up to a certain ratio of the relative amplitudes, but also deteriorate the phase matching. With this in mind, the additional modes can significantly improve the pump efficiency, especially if the next highest-order modes are added because they have the smallest effect on the phase matching. Since the parameter space for an arbitrary superposition as in Equation 5.4 is enormous and the influence of additional pump modes even depends on the focusing parameter, Figure 5.2 only presents some examples on how different pump superpositions affect the threshold power of the $HG_{1,1}$ mode. The focusing parameter is fixed at $\xi = 0.5$ because this value is close to the one of the squeezed light source presented in this thesis. Several main aspects are mentioned in the following.

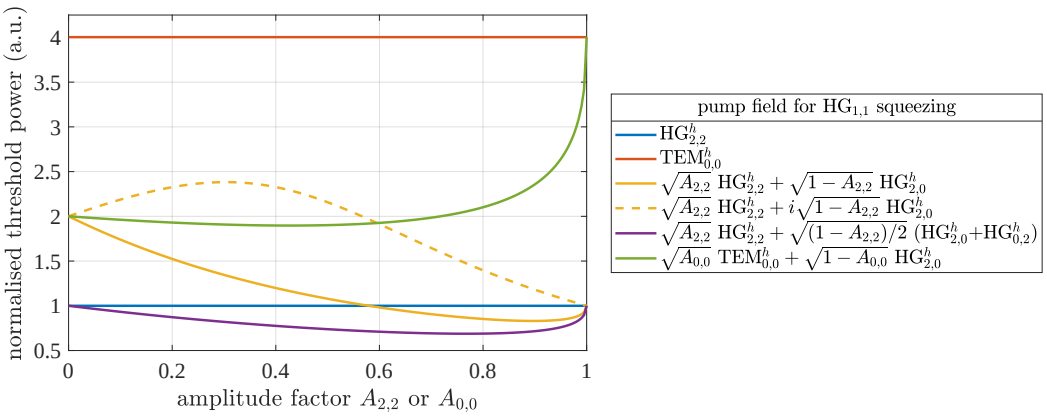

Figure 5.2: Calculated threshold power of the $HG_{1,1}$ mode at $\xi = 0.5$ for the pump fields as indicated by the legend dependent on the relative amplitude factor. The curves are normalised to the single-mode $HG_{2,2}$ pump field.

1. As a single pump mode, the $TEM_{0,0}$ mode is significantly less efficient than the $HG_{2,2}$ mode. The ratio of 4 solely results from the smaller spatial overlap while the worse phase matching is negligible for $\xi = 0.5$. The ratio increases, however, from 4 to 14 for $\xi = 3$.

2. The optimum superposition of the modes $TEM_{0,0}$ and $HG_{2,0}$ with zero relative phase between them can reduce the threshold power by about 54 % compared to only using the $TEM_{0,0}$ mode.

3. Adding the $HG_{2,0}$ to the $HG_{2,2}$ mode can reduce the threshold power by about 17 % compared to the $HG_{2,2}$ mode for a relative phase of zero. With a relative

phase factor of i, the threshold power increases independent of the relative amplitude due to a reduced spatial overlap. At $A_{2,2} = 0$, both curves approach 2 because the spatial overlap for the $HG_{2,0}$ mode is half the one of the $HG_{2,2}$ mode. The worse phase matching is again negligible for $\xi = 0.5$.

4. The $HG_{2,0}$ and $HG_{0,2}$ mode jointly increase the spatial overlap more than individually. Adding both to the $HG_{2,2}$ mode with relative phases of zero can reduce the threshold power by about 31 % compared to the $HG_{2,2}$ mode and results in a threshold power equal to the single-mode $HG_{2,2}$ case for $A_{2,2} = 0$.

5. The dependence on the focusing parameter becomes very clear with a comparison to $\xi = 3$. For this value, none of the above assumed superpositions can outperform the single $HG_{2,2}$ mode due to the increased influence of the Gouy phase and worse phase matching.

For a given OPA cavity, the optimum pump superposition could now be derived with Equation 5.3. There may, however, be limitations as to which pump superposition can be generated in a given setup. These limitations and the resulting choice of the pump field will be outlined for this thesis in the following.

In the squeezed light source presented in this thesis, a cavity-enhanced SHG first generates a harmonic field in the harmonic $TEM_{0,0}$ mode which is then optionally converted into a higher-order pump field by a phase-only spatial light modulator (SLM, compare with Section 2.3.3 and Appendix A.2). In general, this is not necessarily the most efficient order. If an experiment is operated in only one higher-order mode, a spatial light modulator could also first generate this mode which could then pump the corresponding higher-order mode SHG. In this case, the design of the SHG cavity could be optimised for a maximum conversion efficiency at the available pump power in the chosen spatial mode. Due to the similarity of the SHG and parametric down-conversion, it is a reasonable assumption that the pump field for the squeezing process would even be (close to) the optimum superposition, already, if the SHG focusing parameter would be identical to the one of the optical parametric amplifier. However, the optimum SHG cavity design, especially with respect to the reflectivity of the incoupling mirror, depends on the higher-order mode and its individual SHG pump efficiency. To decouple the SHG conversion efficiency from the spatial mode of operation in this thesis, the SHG is exclusively performed in the $TEM_{0,0}$ mode which is then optionally converted into a higher-order pump field by the SLM.

As shown above, certain pump superpositions can achieve higher pump efficiencies than a single-mode pump field. Let us thus investigate whether an SLM can theoretically generate a pump superposition with a sufficiently high conversion efficiency such that this benefit still holds, and whether this can be confirmed in practice. As an example, let us assume that we want to generate squeezed states in the $HG_{1,1}$ mode with the following pump superposition

$$A_\mathrm{p} = \sqrt{A_{2,2}}\,\mathrm{HG}^h_{2,2} + \sqrt{1 - A_{2,2}}\,\mathrm{HG}^h_{2,0}\,. \tag{5.6}$$

According to Figure 5.2, A_p should achieve the highest pump efficiency at $A_{2,2} \approx 0.9$. Next, we can apply the method to estimate the conversion efficiency of an SLM from Section 2.3.3 to A_p. In this case, the SLM generates the field

$$A_\mathrm{res}(x, y, z = 0) \propto I_{0,0}(x, y, 0)\Phi_\mathrm{p}(x, y, 0)\,, \tag{5.7}$$

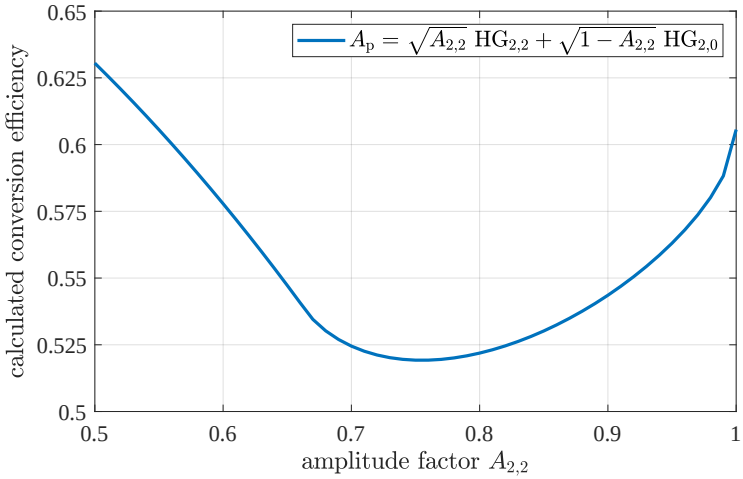

Figure 5.3: Calculated conversion efficiency of a spatial light modulator from the $\mathrm{TEM}_{0,0}$ mode into A_p (as indicated in the legend) for an incoming/outgoing waist ratio of 2.15. The phase plate is assumed to be at the waist position ($z = 0$).

where Φ_p is the phase distribution of A_p. Then, the conversion efficiency yields

$$\eta_\mathrm{conv} = \left| \int A_\mathrm{p}^*(x,y,0) A_\mathrm{res}(x,y,0)\, dxdy \right|^2 . \tag{5.8}$$

Figure 5.3 presents the results dependent on $A_{2,2}$ and assuming the optimum waist ratio for the $\mathrm{HG}_{2,2}$ mode of $w_\mathrm{in}/w_\mathrm{out} = 2.15$ (compare with Fig. 2.4). Evidently, the conversion efficiency significantly decreases when $A_{2,2}$ decreases from 1. At $A_{2,2} \approx 0.9$, this reduction amounts to about 10 %. Still, the reduction in the threshold power at $A_{2,2} \approx 0.9$ is about 17 %. Ideally, this should result in an effective reduction in the threshold power by $1 - 0.83/0.9 \approx 8\,\%$ for the combined system of SLM and OPA cavity.

Let us now compare this calculation with experimental results. For this thesis, different pump superpositions for the different squeezed modes, including the discussed A_p for the $\mathrm{HG}_{1,1}$ mode, were tested and compared with respect to the parametric gain ([Che07]) they could achieve in an OPA cavity for a given harmonic power. Here, the single $\mathrm{HG}^h_{2m,2n}$ always achieved the best results. This discrepancy to the calculation above could originate from technical imperfections in the mode generation. Furthermore, the actual focusing parameter of the OPA cavity could be slightly larger than 0.5 which would reduce the benefit of a pump superposition compared to a single-mode pump field. The exact reason for the discrepancy was not further investigated as sufficient pump power (at least, for the $\mathrm{HG}_{1,1}$ mode) was available, anyway. Consequently, only the $\mathrm{HG}^h_{2m,2n}$ mode is used to generate squeezed states in the $\mathrm{HG}_{m,n}$ mode in this thesis. In theory, a multi-mode pump field could more reliably be generated with two SLMs (or generally two phase plates) [Jes+08], or if the SHG is directly operated in a corresponding higher-order spatial mode, or if the pump field is split up into several paths, where each path generates an individual pump mode, which are then recombined. The latter approach was successfully implemented in [Guo+17].

The design of the OPA cavity

For gravitational-wave detectors (though not in GEO600), the OPAs are typically operated as a dual-resonant cavity, that is, the pump and squeezed field are simultaneously resonant and the pump field is used to stabilise the length of the OPA cavity [MV20; Tse+19]. If, however, the harmonic $\mathrm{HG}^{h}_{2m,2n}$ mode is used to generate squeezed states in the $\mathrm{HG}_{m,n}$ mode, the squeezed and corresponding pump mode do not share the same mode order (except for the $\mathrm{TEM}_{0,0}$ mode squeezing) and are, in general, non-degenerate in a cavity due to their different Gouy phase evolutions. This does not render the typical OPA design impossible but, given the goal to compare four modes with the same OPA cavity, a single-resonant cavity design is more practical to implement. In this design, the squeezed field is resonating while the incoupling mirror is completely transmissive for the pump field such that the latter cannot be used for the OPA length stabilisation. Hence, an auxiliary OPA control field at the fundamental frequency in the spatial mode which is squeezed is required (see Fig. 5.4). In the linear OPA cavity of this thesis (same general design as in Fig. 4.10, details given below), about 1 % of this control field is transmitted and causes a coherent amplitude in the squeezed field such that bright squeezed states in the respective HG modes are produced (see Sec. 3.2.4). Furthermore, the OPA control field requires an additional control loop to stabilise its relative phase to the pump field [Ebe13]. This loop keeps the OPA control field in the state of parametric deamplification in the OPA cavity and is also needed to properly control the measured squeezing quadrature angle.

5.2 Generation and detection of squeezed states in Hermite-Gaussian modes

This section presents the squeezed light source for the Hermite-Gaussian modes $\mathrm{TEM}_{0,0}$, $\mathrm{HG}_{1,1}$, $\mathrm{HG}_{2,2}$ and $\mathrm{HG}_{3,3}$ and characterises the individual performances by analysing and comparing the balanced homodyne detection of the generated states. It is taken from [HWV22] to a large extent.

5.2.1 Setup

Figure 5.4 shows a schematic of the experimental setup (see photgraphs in Fig. 5.5). It is operated with a 2 W non-planar ring laser (NPRO) continously emitting light in the $\mathrm{TEM}_{0,0}$ mode at a wavelength of 1064 nm. The quarter-wave plate minimises the elliptical polarisation and the half-wave plate in combination with the input polariser of the Faraday isolator (FI) determines the power injected into the whole experiment. A phase modulation at a frequency of 120 MHz, driven by the radio-frequency generator RF_1, is imprinted by the electro-optical modulator (EOM) for the length stabilisation of the SHG cavity and the mode cleaner[1] (MC) via the Pound-Drever-Hall scheme [Bla01]. The light field is then split up into two paths. The major fraction of the power propagates to the SHG for the generation of the harmonic pump field which is separated from the incoming field by a dichroic beamsplitter (DBS). Another combination of a half-wave plate and an FI controls the pump power sent to the OPA. Then, two removable mirrors can switch between bypassing the Hamamatsu LCOS spatial light modulator SLM_2 for the $\mathrm{TEM}_{0,0}$ squeezed light generation and converting the harmonic $\mathrm{TEM}_{0,0}$ mode into a higher-order pump mode

[1] Finesse of about 290, linewidth (full width at half maximum) of about 2.5 MHz.

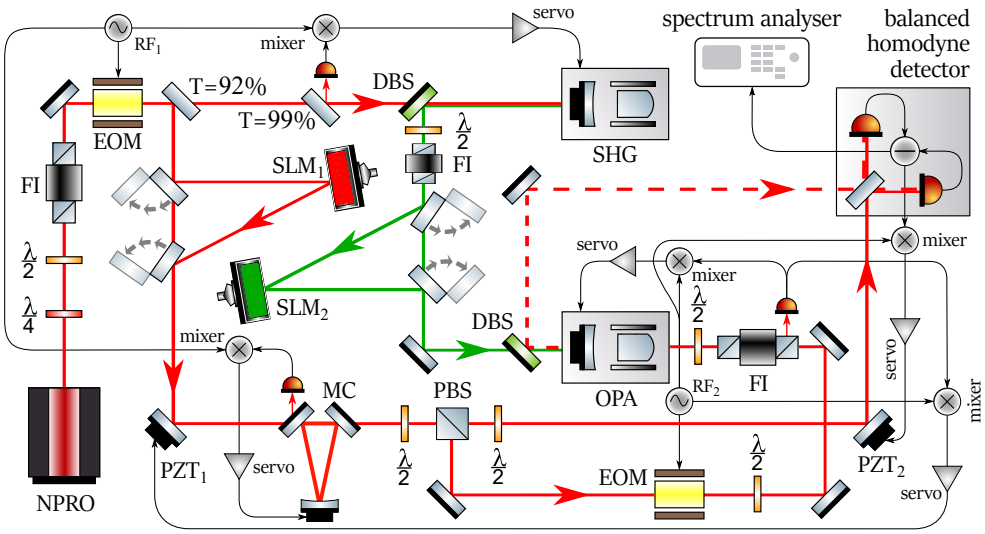

DBS: dichroic beamsplitter	OPA: optical parametric amplifier	SHG: second harmonic generation
EOM: electro-optical modulator	PBS: polarising beamsplitter	: fundamental field (1064 nm)
FI: Faraday isolator	PZT: piezo-electric transducer	: harmonic field (532 nm)
MC: mode cleaner	RF: RF signal generator	: squeezed field (1064 nm)
NPRO: non-planar ring oscillator	SLM: spatial light modulator	

Figure 5.4: Schematic of the experimental setup (based on [HWV22]). In the fundamental and harmonic beam path, two removable mirrors can each switch between the $TEM_{0,0}$ and higher-order mode operation where the latter includes the respective spatial light modulators for the mode generation. The mode-filtered fundamental field is used as a local oscillator at the balanced homodyne detector and as a control field to stabilise the OPA cavity length. The harmonic pump field is not mode-filtered and directly injected into the OPA cavity with a tunable power. The squeezed states are guided to the signal input port of the detector and the noise power spectrum is displayed by a spectrum analyser.

with SLM_2. In both cases, a harmonic power of up to 1 W at a wavelength of 532 nm is available downstream this stage. The pump field is injected into the OPA cavity and a second DBS separates the squeezed field (dashed line) from the pump field. The squeezed field is sent to the balanced homodyne detector and a spectrum analyser calculates the power spectrum of the detected signal with a resolution bandwidth of 300 kHz and a video bandwidth of 300 Hz in the frequency range of 1 MHz to 20 MHz ("full-span").

The lesser fraction of the infrared power in reflection of the $T = 92\,\%$ beamsplitter can also either bypass SLM_1 (same type as SLM_2) for the $TEM_{0,0}$ operation or be converted into a higher-order mode by SLM_1. The subsequent mirror can be controlled via a piezo-electric transducer (PZT) to stabilise the relative phase between the pump field and the OPA control field to the state of parametric deamplification of the control field in the OPA. The corresponding error signal is generated by demodulating the signal from the photodiode at the FI port (to the right of the OPA in Fig. 5.4). The length of the MC cavity is stabilised to the resonance condition for the respective mode that is squeezed to obtain an optimal local oscillator field (with respect to the mode purity) downstream. The subsequent half-wave plate determines how the transmitted power is then split up at the polarising beamsplitter (PBS). The transmitted fraction serves as the local oscillator field at the balanced homodyne detector and is set to a power of about 17 mW which enables an optimum use of the

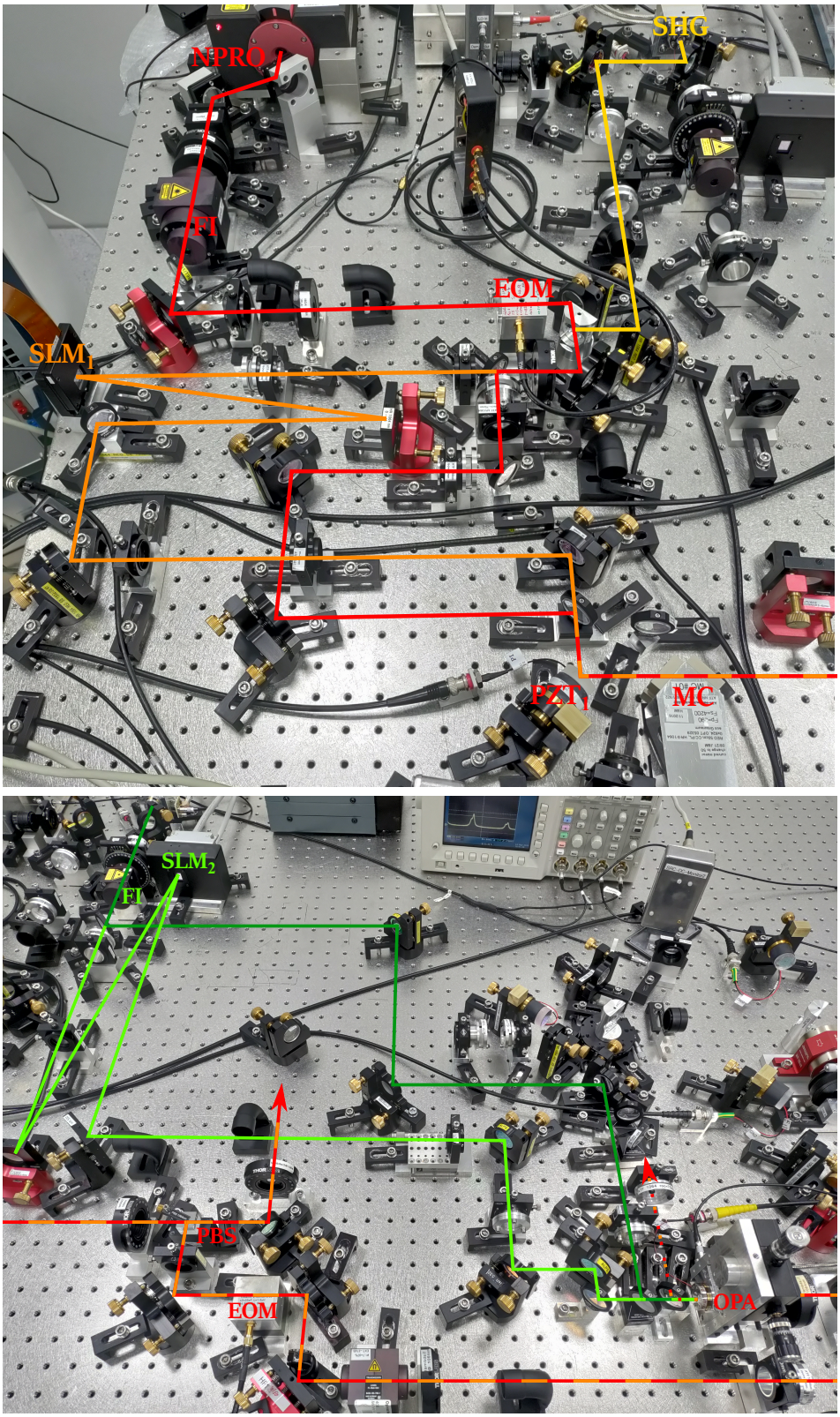

Figure 5.5: Squeezed light source. Top: beam paths of the fundamental field up to the mode cleaner on the bottom right (red: $TEM_{0,0}$ field, orange: higher-order mode field via SLM_1 on the very left, yellow: $TEM_{0,0}$ path to SHG). Bottom: beam paths of harmonic and fundamental field (dark green: $TEM_{0,0}$ pump field from SHG to OPA, bright green: same for the higher-order mode pump field via SLM_2 on the top left, red and orange: as in top figure, left arrow: LO beam path, right arrow: squeezed field path, bottom path: OPA control field).

dynamic range of the homodyne detector photodiodes. Another half-wave plate adjusts the polarisation of the local oscillator field to the one of the squeezed field. The PZT mirror in this path stabilises or scans the relative phase between the squeezed field and the local oscillator field to enable the measurement of the squeezing and anti-squeezing level. Here, the corresponding error signal results from demodulating the output signal of the homodyne detector. The part which is reflected by the PBS is the OPA control field. The second EOM imprints a phase modulation at a frequency of 45 MHz, driven by RF_2, which is used for the length stabilisation of the OPA cavity as well as for the two phase stabilisations mentioned above. The combination of the half-wave plate downstream from this EOM and the subsequent FI controls the power in the OPA control field. It was set to the minimum power of about 500 µW which still allowed to properly stabilise the OPA cavity length. The half-wave plate between the FI and the OPA adjusts the polarisation to the one of the squeezed field.

The hemilithic linear OPA cavity generally has the same design as the SHG cavity shown in Figure 4.10. It contains a periodically poled potassium titanyl phosphate (PPKTP) crystal which measures $1.0 \times 2.0 \times 9.3\,\mathrm{mm}$ in x, y and z (propagation) direction. The curved crystal face serves as a highly reflective end mirror, $R_{\mathrm{end},1064\,\mathrm{nm}} > 99.96\,\%$ and $R_{\mathrm{end},532\,\mathrm{nm}} = 99.9\,\%$, while the plane face is anti-reflective coated for both wavelengths. The nominal reflectivities of the incoupling mirror are $R_{\mathrm{in},1064\,\mathrm{nm}} = 92\,\%$ and $R_{\mathrm{in},532\,\mathrm{nm}} < 0.2\,\%$ such that the OPA's half width at half maximum (bandwidth) is about 25 MHz. The radii of curvature are $R_{c,\mathrm{in}} = 25\,\mathrm{mm}$ and $R_{c,\mathrm{end}} = 12\,\mathrm{mm}$, setting the waist of the squeezed field's eigenmodes to about 33 µm in radius near the crystal center. A peltier element stabilises the crystal temperature via a control loop and is used to optimise the phase matching. The SHG cavity in this setup has the same geometry and crystal but a reflectivity of the incoupling mirror of $R_{\mathrm{in},1064\,\mathrm{nm}} = 90\,\%$ to enable high conversion efficiencies at high fundamental input power.

5.2.2 Results

Figure 5.6 shows the results for a measurement frequency of 4 MHz dependent on the total harmonic power. The data points were deduced from individual full-span measurements as shown in Figure 5.7. Table 5.1 summarises the maximum squeezing levels for the four modes together with the corresponding total harmonic power. As seen in Figure 5.6, the higher-order modes require significantly more pump power than expected from Figure 5.1 to achieve the same squeezing levels as the $TEM_{0,0}$ mode for a combination of two reasons. First, the conversion efficiency of SLM_2 is not perfect and the generated higher-order pump field is not mode-filtered. The exact efficiency could not be measured but it can be estimated from SLM_1 under the assumption that both SLMs reach similar efficiencies due to the similarity of the models. The conversion efficiency of SLM_1 was measured for the $HG_{4,4}$ mode to be close to 29 %, i.e. 29 % of the $TEM_{0,0}$ power incident on SLM_1 could be detected in transmission of the MC cavity at the $HG_{4,4}$ resonance condition. Second, the mode matching of the pump mode to the OPA cavity rapidly decreases with increasing mode order (see Sec. 2.3.3, "Sensitivity to spatial mismatches"). Hence, the pump field effectively consists of the intended pump mode to less than 29 %. Figure 5.1 indicates the measured "total harmonic OPA pump power" that is injected into the OPA cavity (short: total harmonic power) instead of the effective pump power which is coupled to the intended OPA eigenmode. Nevertheless, the balanced homodyne

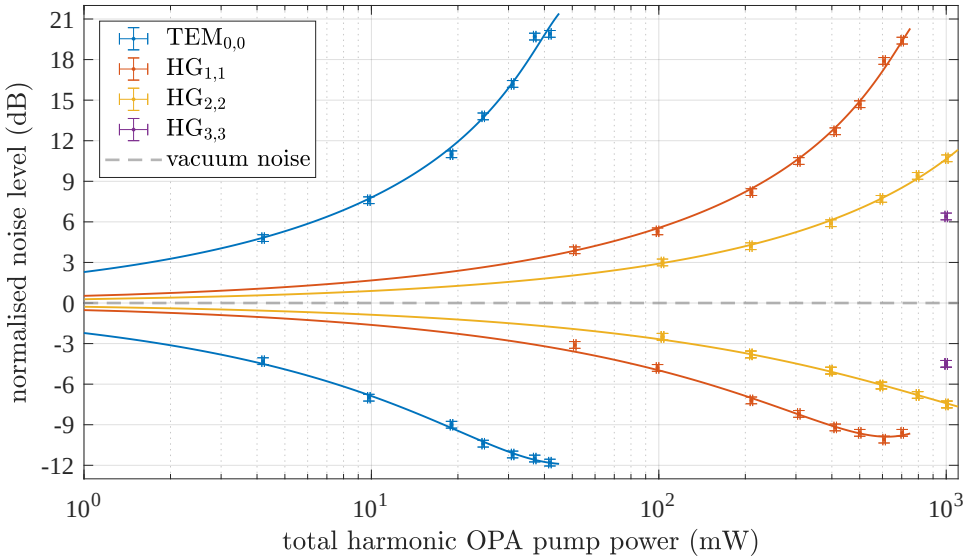

Figure 5.6: Squeezing and anti-squeezing results at a measurement frequency of 4 MHz, normalised to the noise level of the vacuum state [HWV22]. The measurement points were derived from individual full-span measurements (see Figure 5.7). Solid lines: theoretical model fitted to the measurement data.

detector only measures the vacuum/squeezed noise in the intended mode due to the mode-filtered local oscillator.

Table 5.1: Summary of the characterisation of the squeezed light source. n.c.: not conclusive.

	Maximum squeezing level (dB)	Total harmonic power (mW)	Homodyne contrast (%)	Expected detection efficiency (%)	Fitted detection efficiency (%)	Fitted phase noise (mrad)
$TEM_{0,0}$	11.8(3)	41.8(4)	98.5(5)	94.6(12)	94.4(3)	4 ($\leq$10)
$HG_{1,1}$	10.1(3)	608(6)	98.0(5)	93.6(12)	92.7(3)	16 ($\geq$15)
$HG_{2,2}$	7.5(3)	1005(10)	96.0(5)	89.8(12)	89.0(3)	n.c.
$HG_{3,3}$	4.5(3)	1000(10)	95.5(5)	88.8(12)	n.c.	n.c.

The measurement data are also compared to the theoretical model from Equation 3.44 by varying the detection efficiency, phase noise and threshold power to obtain the best match between this theoretical model and the measurement results (solid lines in Figure 5.6). The fitted parameters are shown in Table 5.1 apart from the threshold power because its value is misleading due to the discrepancy between the effective pump power and the total harmonic power.

The fitted detection efficiencies are in good agreement with the expectations which are derived from the expected total optical loss (see also Sec. 3.2.3). Included in the total optical loss are the OPA escape efficiency, which is at 99.0(5) %, the quantum efficiency of the homodyne detector's photodiodes, which is at 99.0(5) %, and loss from optics in the path of the squeezed field with 0.4(2) %. These three values are assumed to be equal for the four modes. Finally, the homodyne detector only measures the quantum noise reduction in the fraction of the squeezed field which is mode-matched to the local oscillator field. The corresponding homodyne contrast was measured as described in Sec. 3.2.3 with the LO and OPA control field. The results can also be found in Table 5.1. A high homodyne contrast becomes more challenging with increasing mode order (see again Sec. 2.3.3).

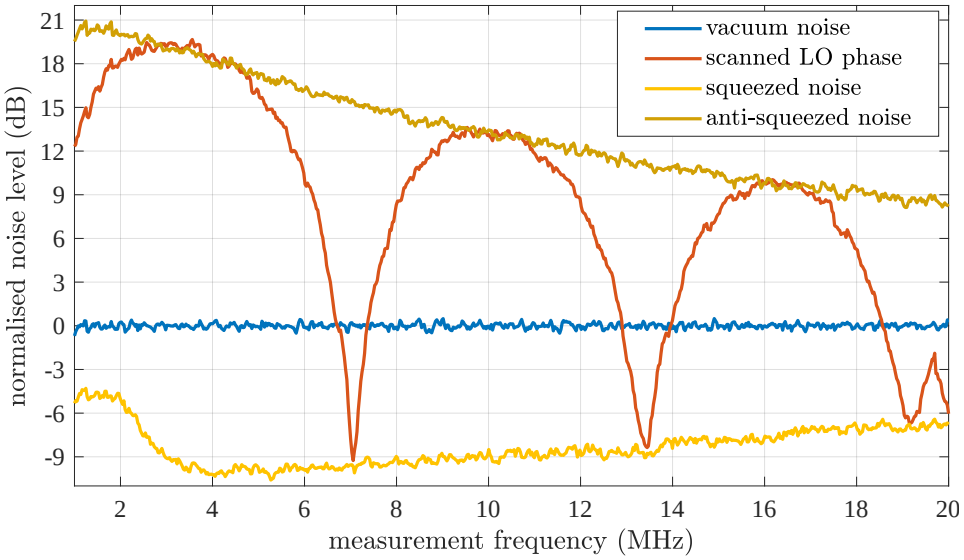

Figure 5.7: Measurement result for the $HG_{1,1}$ mode at a total harmonic power of 610 mW, normalised to the vacuum state noise level [HWV22]. LO: local oscillator field. Resolution bandwidth: 300 kHz, video bandwidth: 300 Hz, electronic dark noise (not shown): about −25 dB over full span and not subtracted from the data.

The effect of phase noise only becomes clearly visible in the regime of high anti-squeezing. If this regime is reached, phase noise distinctly increases the frequency where the maximum quantum noise reduction is observed (see Fig. 3.10). If this regime is not reached and if technical laser noise additionally dominates at lower frequencies, the effect of phase noise cannot be conclusively distinguished from the effect of a reduced detection efficiency. For the $HG_{2,2}$ and $HG_{3,3}$ mode, the available harmonic pump power was not sufficient to reach the regime of sufficiently high anti-squeezing. In the range of the expected detection efficiency for the $HG_{2,2}$ measurement, the theoretical model can only derive an upper limit for the phase noise of 50 mrad. For the $HG_{3,3}$ mode, the harmonic power did not suffice to take enough data points for a reasonable fit in Figure 5.6. The single conducted $HG_{3,3}$ full-span measurement can be explained with a detection efficiency of 87(6) % and a phase noise of 80(70) mrad. Due to these large uncertainties, both parameters cannot be properly inferred from the theoretical model, even though the expected detection efficiency is within the range of the fitted value. There is, however, a clear difference of at least 5 mrad in the fitted phase noise of the $TEM_{0,0}$ and $HG_{1,1}$ measurements. Since the only differences in the setups for these two modes are the two SLMs, they are the most likely cause for the higher phase noise. However, the exact mechanism has to be further investigated.

Furthermore, the low $TEM_{0,0}$ phase noise of about 4 mrad, which is not significantly larger than e.g. in [Vah+16], indicates that the residual technical laser noise of the bright squeezed field (see Sec. 3.2.4) was negligible at a measurement frequency of 4 MHz. Otherwise, it would have led to higher fitted phase noise values. Since the coherent power in the squeezed field was mode-independent, the same applies to the higher-order modes.

Figure 5.7 shows one $HG_{1,1}$ full-span measurement with a squeezing level of 10 dB at 4 MHz for a total harmonic power of about 610 mW. For the squeezing and anti-squeezing curves, the relative phase between the squeezed field and local oscillator field was stabilised, accordingly. Both curves decrease towards higher frequencies in agreement with effects due to the OPA bandwidth. For the “scanned

LO phase" curve, this relative phase was scanned over more than two cycles during the scan time of the spectrum analyser which results in the oscillation between the squeezing and anti-squeezing levels. The increased noise in the squeezing curve at low frequencies is the residual technical laser noise of the fraction of the OPA control field which is transmitted through the OPA and also measured by the balanced homodyne detector.

5.3 Summary

Section 5.1 discussed the main aspects of the theory behind an efficient pump field for the direct generation of squeezed states in higher-order modes. The squeezing process of any higher-order Hermite-Gaussian mode can be pumped with an arbitrary superposition of a corresponding set of harmonic modes. Different superpositions provide different spatial overlaps to the squeezed field and different phase matchings, and the optimum superposition for a given OPA cavity can be derived either via the equation for the threshold power or via experimental testing.

In this thesis, the pump field was limited to the most efficient single pump mode due to the limited ability of the used spatial light modulator to generate superpositions of different pump modes. Furthermore, the pump field was not mode-filtered and effectively included at least 70 % of "wasted" pump power. If a pump field with both higher pump efficiency and higher purity is available, the required pump power will be significantly smaller than in the presented squeezed light source. A reduction in the order of 75 % is theoretically possible. The required pump power could further be reduced via an OPA incoupling mirror with higher power reflectivity. For this thesis, such an incoupling mirror was, however, not immediately available.

The characterisation of the squeezed light source in Section 5.2 showed that squeezed states in higher-order modes were generated and detected with high and unprecedented squeezing levels. Previous results for higher-order modes were limited to a maximum quantum noise reduction of 5 dB [Ste+18], measured in a first-order mode. Hence, 10 dB in the $HG_{1,1}$ mode, 7.5 dB in the $HG_{2,2}$ mode and 4.5 dB in the $HG_{3,3}$ mode represent a new milestone and could, for the first time, significantly reduce the gap to the $TEM_{0,0}$ mode (here, 12 dB). The fitted detection efficiencies are in good agreement with the expected optical loss budgets and the spatial light modulators used to generate the higher-order modes most likely increased the phase noise in the higher-order mode measurements. The $HG_{2,2}$ and $HG_{3,3}$ results were primarily limited by the available pump power.

These results demonstrate the general feasibility of experiments which require a high quantum noise reduction in higher-order spatial modes. The adaptation of this scheme to other frequency bands (e.g. the audio-band for gravitational-wave detectors) and the generation of squeezed vacuum states are now technical steps which can be carried out in the same way as for the $TEM_{0,0}$ mode [Che+07; Vah+10]. In the GEO600 detector, for instance, the OPA cavity length is stabilised using an auxiliary control field in the polarisation orthogonal to the one of the squeezed field, where a degenerate resonance condition with the squeezed field is obtained via a variable frequency shift of the control field [Vah+10]. In this way, the control field does not introduce technical laser noise in the squeezed field and the squeezed light source generates squeezed vacuum states.

The next chapter presents the application of the presented squeezed light source in a tabletop Michelson interferometer.

Chapter 6

Quantum-enhanced Michelson Interferometer in Higher-Order Hermite-Gaussian Modes

The previous chapter presented the squeezed light source and aimed to demonstrate that high levels of quantum noise reduction, comparable with those in the $TEM_{0,0}$ mode, can be achieved in higher-order Hermite-Gaussian modes. This was done in a pure "squeezed light generation" setup. This chapter, first of all, targets the same demonstration but in an actual measurement application, that is, in a Michelson interferometer with an injected signal. Second of all, this chapter also follows a specific goal for the $TEM_{0,0}$ mode: the first demonstration of a 10 dB sensitivity improvement of a shot-noise limited Michelson interferometer via squeezed states of light, as targeted for the future gravitational-wave detectors.

This chapter first provides a rationale for implementing the balanced homodyne detection scheme instead of the direct readout scheme in the Michelson interferometer. Then, the setup and results are discussed. The Sections 6.2 and 6.3 are taken from the publication [Hei+22] to a large extent.

6.1 Direct vs. balanced homodyne readout

6.1.1 Regarding advanced gravitational-wave detectors

Direct readout

During the joint observation run O3 in 2019 and 2020, the Advanced LIGO, Advanced Virgo, KAGRA and GEO600 detectors employed the direct readout scheme, also referred to as *DC readout* (see Fig. 6.1). This is a special kind of homodyne detection where the GW detector is set to an offset from the dark fringe. Hence, the interferometer output provides a static local oscillator field whose amplitude can be adjusted via the dark fringe offset and which co-propagates with the signal field such that it is automatically mode-matched to it. This detection scheme, however, has several disadvantes which are, for instance, discussed in [FEF14; ET 20].

First of all, the dark fringe offset enables a direct coupling of laser power noise, which is imprinted on the static LO field, from the interferometer input field to the gravitational-wave readout. Furthermore, the operation of Advanced LIGO revealed that the offset in the differential arm length, which is required for the DC readout, enables a coupling channel from the residual motion of the signal recycling cavity length to the GW readout [FEF14]. This constitutes a sensitivity limitation at low signal frequencies. The DC readout also increases the requirements on the laser noise because the arm cavities are operated slightly off their resonance condition.

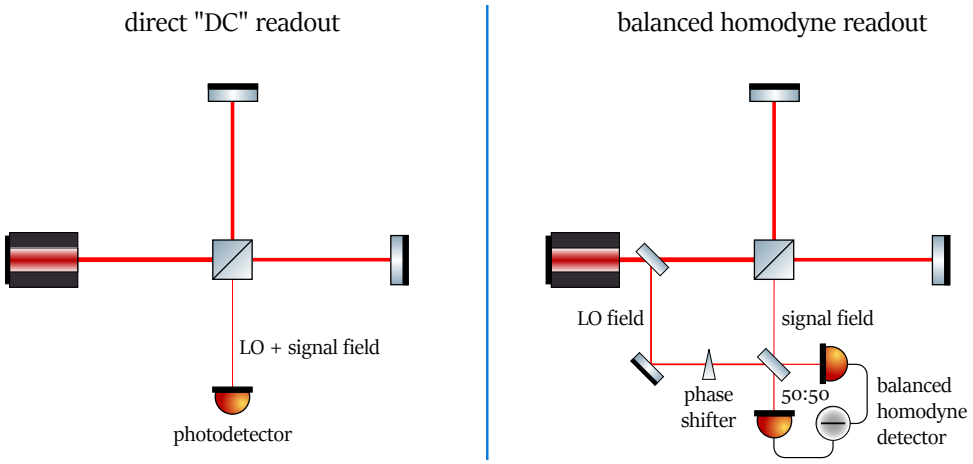

Figure 6.1: Simplified schematics for the direct and balanced homodyne readout. Left: an offset from the dark fringe provides a static local oscillator (LO) field which co-propagates with the signal field until being detected by a photodetector. Right: a separate local oscillator field is superimposed with the signal field at the 50:50 beamsplitter of the balanced homodyne detector. Via a phase shifter in the LO beam path, the readout quadrature can be set freely. This is only one example for how the LO field can be obtained. The interferometer is set to the dark fringe.

This asymmetry results in a stronger coupling from the laser power fluctuations to the gravitational-wave readout via radiation pressure [CB11].

An additional challenging aspect is the constant co-propagation of the local oscillator (LO) and signal field. As one consequence, a fraction of the LO field can be sent back into the interferometer, unintentionally via backscattering or intentionally due to the signal recycling, which can lead to increased noise in the gravitational-wave readout. Furthermore, the constant LO field influences the interferometer alignment control scheme whose error signals are derived from measuring samples of the interferometer output field [FEF14].

A final drawback of the DC readout is the inability to freely set the readout quadrature, i.e. the relative phase between the LO and signal field. This degree of freedom will, however, be critical for new quantum nondemolition readout schemes which may be implemented in the detectors at some point in the future [FEF14].

Balanced homodyne readout

The balanced homodyne detection scheme as also shown in Figure 6.1 works very similar to the characterisation of squeezed states via a balanced homodyne detector as discussed in Section 3.2.3 and used in Section 5.2. Here, the interferometer signal field is only superimposed with a separate local oscillator field at the detection stage. Thus, an offset from the dark fringe is not required and the associated issues do not arise, or are at least strongly suppressed. Additional advantages are the theoretical insensitivity to noise in the LO field in case of a high common mode rejection and the ability to freely choose the readout quadrature as the phase of the LO field can be controlled individually. With respect to the application of squeezed light, the balanced homodyne readout also has an advantage because it allows for slightly higher levels of quantum noise reduction. Due to the symmetry of the interferometer, minimising or, theoretically, completely avoiding the static leakage field in the interferometer output also minimises the fraction of the squeezed field which leaks

towards the interferometer input and cannot be used for a quantum noise reduction in the output.

The balanced homodyne readout has an own set of challenges. For example, the LO field has to be stabilised with respect to amplitude noise and path length fluctuations [Ste+15], and the LO field also needs to be stably mode-matched to the signal field [Zha+17]. Nevertheless, the third-generation detectors as well as the upgrades to the Advanced LIGO detectors, LIGO-LF [Yu+18] and LIGO Voyager [Adh+20], plan to implement the balaned homodyne readout scheme.

6.1.2 Regarding the presented tabletop interferometer

For the tabletop Michelson interferometer in this thesis, the balanced homodyne detector has an additional advantage over the DC readout because no output mode cleaner is implemented. This is explained in the following.

In general, the local oscillator (LO) field A_{LO} can be in an arbitrary superposition of spatial modes (compare with Sec. 3.2.3)

$$A_{\mathrm{LO}} \propto \sum_i c_i A_i \qquad \text{with} \qquad \sum_i |c_i|^2 = 1 \tag{6.1}$$

such that it beats with the vacuum fluctuations in all of these modes. Hence, the vacuum fluctuations in a given mode A_i significantly contribute to the measured shot noise in the interferometer output for a sufficiently large $|c_i|^2$. If the squeezed field has zero spatial overlap to this mode, it cannot reduce this mode's contribution to the measured shot noise and a fraction $|c_i|^2$ of the squeezed field is effectively lost. Thus, a maximum spatial overlap between the LO and squeezed field is necessary for a minimum effective optical loss and a high shot noise reduction.

Let us now assume a simple Michelson interferometer as shown in Figure 6.2 with a 50:50 beamsplitter, using the convention where a transmitted field experiences a phase shift of 90° (compare with Sec. 1.2.2). Let us further assume that the sensing field, injected through the interferometer input port, as well as the field in the north arm are in the same pure, normalised spatial mode of operation A_{SMOP} with respect to a given eigenbasis. However, the field in the east arm that returns to the beamsplitter is not purely in the mode A_{SMOP}, e.g. due to some misalignment or imperfect mirror parameters. For normalised unit input power, it is:

$$\begin{aligned} a_N &= \sqrt{\frac{1}{2}} A_{\mathrm{SMOP}} \,, \\ a_E &= i\sqrt{\frac{1}{2}} \left(\sqrt{\mu} A_{\mathrm{SMOP}} + \sqrt{1-\mu} A_{\mathrm{mis}} \right) e^{i\varphi} \,, \end{aligned} \tag{6.2}$$

where $a_{N/E}$ are the fields from the north and east arm just before recombination, μ is the spatial overlap between these two fields, A_{mis} is the normalised field contribution associated with the spatial mismatch (no spatial overlap to A_{SMOP}) and φ is the relative phase between the recombining fields which is here completely assigned to a_E. The output field in the interferometer south port, which is the local oscillator field in the DC readout scheme, yields

$$A_{\mathrm{LO}}(\mu, \varphi) = \frac{i}{2} \left[\left(1 + \sqrt{\mu} e^{i\varphi} \right) A_{\mathrm{SMOP}} + \sqrt{1-\mu} A_{\mathrm{mis}} e^{i\varphi} \right] . \tag{6.3}$$

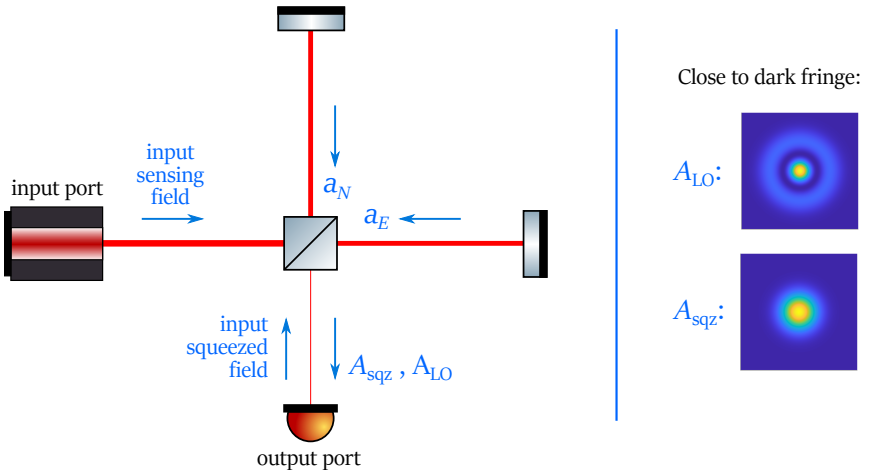

Figure 6.2: Simple quantum-enhanced Michelson interferometer at the dark fringe including a contrast defect. The coherent sensing field and the squeezed field are injected through the east (input) and south (output) port, respectively. Assumptions: they are perfectly mode-matched to each other, but the recombining arm fields a_N and a_E are not. Close to the dark fringe with respect to the sensing field at the output port, the sensing field's leakage field A_{LO} and the reflected squeezed field A_{sqz} will then have a reduced spatial overlap as the plots of the intensity distributions on the right show (assuming a waist size mismatch and that the interferometer is operated in the $\mathrm{TEM}_{0,0}$ mode).

Repeating this calculation for the squeezed field which is both injected and detected at the output yields:

$$A_{\mathrm{sqz}}(\mu,\varphi) = \frac{1}{2}\left[\left(\sqrt{\mu}e^{i\varphi}-1\right)A_{\mathrm{SMOP}} + \sqrt{1-\mu}A_{\mathrm{mis}}e^{i\varphi}\right] , \tag{6.4}$$

assuming that the squeezed field is perfectly mode-matched to the sensing field in the north and east arm, respectively.

In the DC readout scheme, two optical loss contributions for the squeezed field arise from these equations. First, a fraction of the squeezed field is lost towards the interferometer input port if the interferometer is operated at a dark fringe offset (with respect to the sensing field at the output port). The remaining fraction r_{sqz} of the squeezed field which is reflected back to the output port can be computed as

$$r_{\mathrm{sqz}}(\mu,\varphi) = \int \left|A_{\mathrm{sqz}}(\mu,\varphi)\right|^2 dxdy = \frac{1}{4}\left(\left|\sqrt{\mu}e^{i\varphi}-1\right|^2 + 1 - \mu\right) . \tag{6.5}$$

The second loss contribution arises due to the imperfect spatial overlap between the local oscillator and squeezed field. Close to the dark fringe at $\varphi = \pi$, it is

$$\begin{aligned} A_{\mathrm{LO}}(\mu,\varphi\approx\pi) &\approx \frac{i}{2}\left[(1-\sqrt{\mu})\,A_{\mathrm{SMOP}} - \sqrt{1-\mu}A_{\mathrm{mis}}\right] \\ A_{\mathrm{sqz}}(\mu,\varphi\approx\pi) &\approx -\frac{1}{2}\left[(1+\sqrt{\mu})\,A_{\mathrm{SMOP}} + \sqrt{1-\mu}A_{\mathrm{mis}}\right] \end{aligned} \tag{6.6}$$

Hence, for small contrast defects $\mu \approx 1$, we have $A_{\mathrm{sqz}} \approx -A_{\mathrm{SMOP}}$ while the local oscillator field has a significant contribution from A_{mis} (see Fig. 6.2). The spatial overlap between the sensing and squeezed field in the output, normalised to their

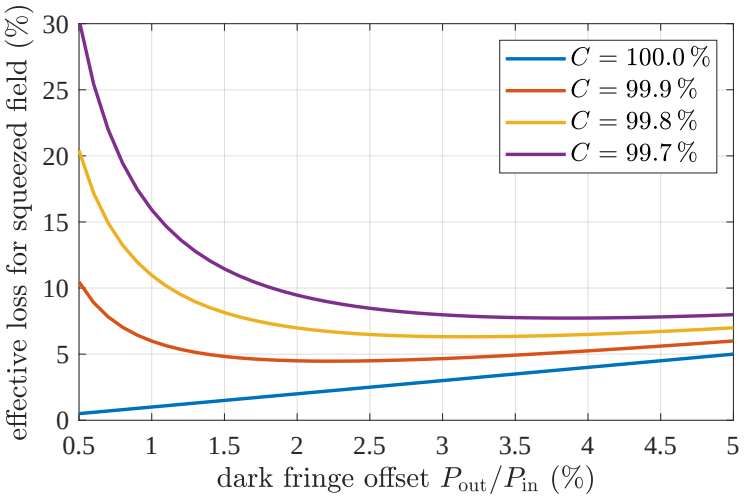

Figure 6.3: DC readout in a simple Michelson interferometer: small contrast defects (C: contrast) due to an imperfect spatial overlap of the recombined beams can lead to a large effective optical loss for the squeezed field. In addition to the leakage loss towards the interferometer input due to the dark fringe offset (blue curve, $C = 100\,\%$), a highly reduced spatial overlap between the squeezed and local oscillator field is the reason. P_{in}: optical power in the coherent sensing field injected into the interferometer input port, P_{out}: the sensing field's leakage power in the interferometer output port.

fractions which reach the output port, can be computed as

$$\mu_{out}(\mu,\varphi) = \frac{\left|\int A^{*}_{sqz}(\mu,\varphi) A_{LO}(\mu,\varphi)\, dxdy\right|^2}{r_{sqz}(\mu,\varphi) \times \int |A_{LO}(\mu,\varphi)|^2\, dxdy}\,. \tag{6.7}$$

In conclusion, a fraction r_{sqz} of the squeezed field is reflected back to the interferometer output and a fraction μ_{out} of r_{sqz} is matched to the local oscillator field. Hence, a fraction $r_{sqz}\,\mu_{out}$ of the squeezed field can effectively be used for the quantum noise reduction such that the total effective optical loss from these two loss sources amounts to

$$L_{total}(\mu,\varphi) = 1 - \mu_{out}(\mu,\varphi) r_{sqz}(\mu,\varphi)\,. \tag{6.8}$$

This effective optical loss is shown in Figure 6.3 dependent on the dark fringe offset which is indicated as the ratio of the input and output power of the sensing field. For $\mu = 1$, the interferometer contrast is $C = \sqrt{\mu} = 100\,\%$[1] and the leakage towards the interferometer input is the only loss source for the squeezed field. In this case, the loss is equal to the dark fringe offset due to the symmetry of the interferometer. For a decreasing interferometer contrast, the reduced spatial overlap of the squeezed and LO field becomes increasingly important. Especially at small dark fringe offsets where the A_{mis} contribution in the LO field is large, this can cause several tens of percent more loss even for relatively small contrast defects of a few 0.1 %. In practice, the interferometer contrast always shows some defects (see e.g. Tab. 6.1).

L_{total} could be significantly reduced with an output mode cleaner which would

[1] Assuming that the contrast only depends on μ for an otherwise ideal lossless interferometer.

filter out the A_{mis} contributions.[2] In this case, $\mu_{\mathrm{out}}(\mu, \varphi) = 1$ such that the loss contribution from the contrast defect would ideally vanish. However, such an output mode cleaner is not implemented in the tabletop interferometer presented below. In this case, using the balanced homodyne detection scheme has a similar effect. Here, the separate LO field is not affected by the interferometer contrast defects and ideally remains in the pure spatial mode of operation A_{SMOP} such that $\mu_{\mathrm{out}}(\mu, \varphi) \approx 1$ for $A_{\mathrm{sqz}} \approx -A_{\mathrm{SMOP}}$, which should hold close to and at the dark fringe. In addition, the loss towards the interferometer input is also minimised because the interferometer is operated directly at the dark fringe in the balanced homodyne readout scheme.

6.2 Setup

6.2.1 Overview of the complete setup

The setup as shown in Figure 6.4 (schematic) and 6.5 (photograph) operates with a 2 W non-planar ring laser (NPRO) which continuously emits light in the $\mathrm{TEM}_{0,0}$ mode at a wavelength of 1064 nm. The major fraction of the light field is directed towards the squeezed light source where the cavity-enhanced second harmonic generation (SHG) converts the incoming field to a wavelength of 532 nm to provide the pump field for the parametric down-conversion in a type-I optical parametric amplifier (OPA). The SHG is exclusively performed in the $\mathrm{TEM}_{0,0}$ mode and the harmonic field then either bypasses the Hamamatsu LCOS spatial light modulator SLM_2 or is converted into a higher-order pump mode via SLM_2 (see Section 2.3.3) for a $\mathrm{TEM}_{0,0}$ or a higher-order mode operation of the OPA, respectively. The OPA cavity then generates squeezed states in the respective spatial mode of operation (SMOP) which are injected into the interferometer's output port. Further details on the squeezed light source can be found in Chapter 5.

The fraction of the 1064 nm field which is transmitted by the first mirror either bypasses SLM_1 (same type as SLM_2) to remain in the $\mathrm{TEM}_{0,0}$ mode or is converted by SLM_1 into the SMOP. The subsequent input mode cleaner (IMC) is stabilised to the resonance condition of the SMOP to provide a mode-filtered beam for a threefold downstream application. First, about 500 µW are reflected to the squeezed light source for the length stabilisation of the OPA cavity to the resonance condition of the SMOP. Second, 7 mW are directly guided to the balanced homodyne detector as the local oscillator field. Third, 2 mW enter the interferometer through the input port. The Michelson interferometer consists of a 50:50 beamsplitter and two highly-reflective end mirrors with attached piezo-electric transducers (PZT) and has an arm length of 10 cm. PZT_1 is driven at a radio-frequency (rf) of 100 kHz and generates phase-modulation sidebands whose beat note with the interfered carrier fields from both interferometer arms is detected by the photodetector in reflection of the interferometer. With the demodulated signal, the interferometer is stabilised to the dark fringe with respect to the output port (further explained in Sec. 6.2.2). PZT_2 can optionally inject a signal, which will be called *GW signal*. The frequency of this GW signal is matched to the frequency of highest observed quantum noise reduction: 4 MHz for the $\mathrm{HG}_{1,1}$ and $\mathrm{HG}_{2,2}$ mode and 5 MHz for the $\mathrm{TEM}_{0,0}$ mode. The interferometer output field propagates to the balanced homodyne detector and is superimposed with the local oscillator field on a 50:50 beamsplitter. PZT_3 optimises the readout quadrature via the local oscillator phase for a maximum detected GW

[2] An output mode cleaner could, however, also cause effective optical loss for the squeezed field due to an imperfect mode matching to the cavity and a limited linewidth.

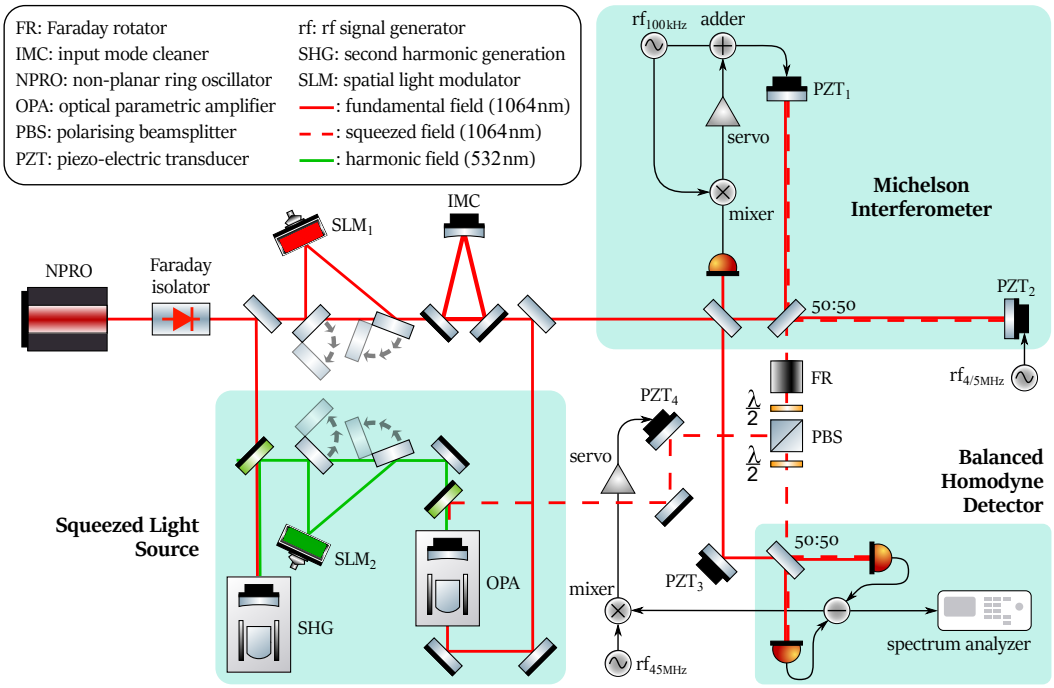

Figure 6.4: Schematic of the experimental setup (based on [Hei+22]). The Michelson interferometer can be operated in the $TEM_{0,0}$ or a higher-order spatial mode generated by SLM_1. It is stabilised to the dark fringe with respect to the output port via a 100 kHz beat note which arises from a modulation by PZT_1 and is detected in reflection of the interferometer. PZT_2 can inject an artificial signal at megahertz frequencies. The squeezed states (source discussed in Chapter 5) are injected into the interferometer output port via a polarising beamsplitter. Using the Faraday rotator, the squeezed field co-propagates with the signal field to the balanced homodyne detector where both are superimposed with the local oscillator field. PZT_3 optimises the readout quadrature for a maximum detected signal and PZT_4 controls the phase of the squeezed field via a beat note in the detector output signal for the measurement of the squeezing and anti-squeezing level.

signal. A spectrum analyser then measures the power spectrum of the subtracted photodetector signals.

The combination of the polarising beamsplitter (PBS) and Faraday rotator (FR) first injects the squeezed field into the interferometer and then transmits it towards the balanced homodyne detector after being effectively reflected by the interferometer. Phase-modulation sidebands, which remain in the squeezed field from the length stabilisation of the OPA cavity, provide a 45 MHz beat note in the detector signal. This beat note is used to stabilise the relative phase between the squeezed and local oscillator field via PZT_4 for the controlled measurement of the squeezing and anti-squeezing levels.

6.2.2 Stabilisation to the dark fringe

The Michelson interferometer is stabilised to the dark fringe via one of the arm end mirrors which can be actuated by an attached piezo-electric transducer (PZT) (see Fig. 6.6). First, this PZT modulates the phase of the light field in the north arm at a frequency of $\Omega = 100\,\text{kHz}$. Omitting the oscillation at the optical carrier frequency,

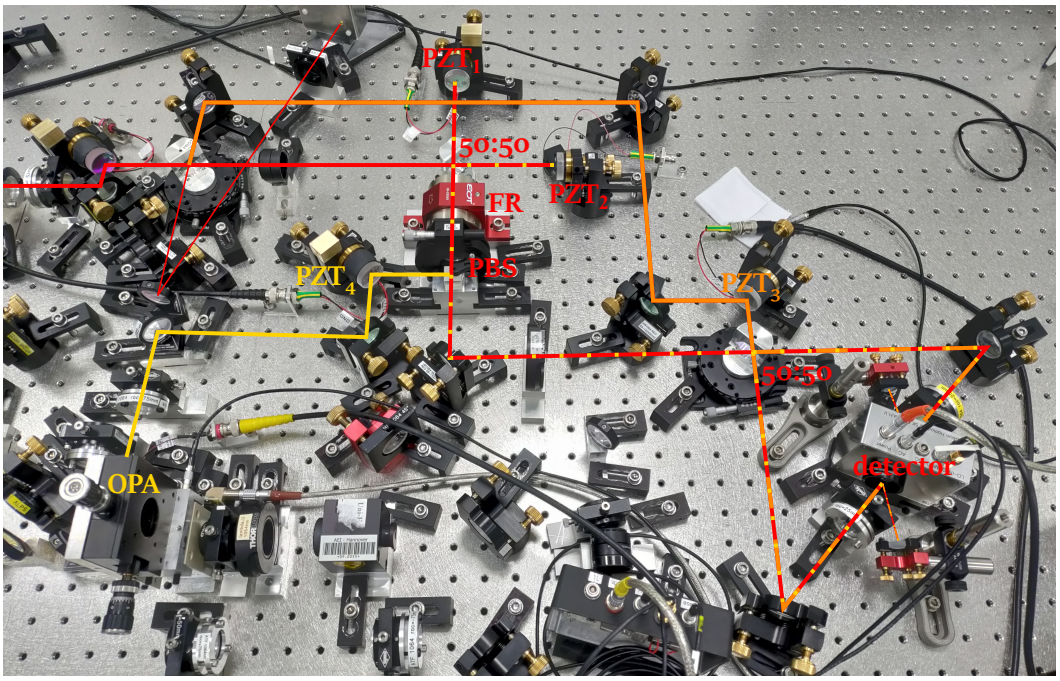

Figure 6.5: Photograph of the Michelson interferometer (centre top) with the OPA cavity (bottom left) and the balaned homodyne detector including retro-reflectors (bottom right). Red: interferometer input and signal field, thin red on top left: field detected for stabilisation to dark fringe, orange: local oscillator field, yellow and yellow dotted: squeezed field.

the north arm field just before the point of recombination is given by

$$\begin{aligned} a_N &= \frac{a_{\text{in}}}{\sqrt{2}} e^{i\beta\cos(\Omega t)} \\ &\approx \frac{a_{\text{in}}}{\sqrt{2}} \left(1 + i\frac{\beta}{2}e^{i\Omega t} + i\frac{\beta}{2}e^{-i\Omega t}\right) , \end{aligned} \tag{6.9}$$

where the phase modulation is expressed in terms of Bessel functions and approximated according to [Bla01]. β is the modulation index.

The east arm field just before the point of recombination is

$$a_E = i\frac{a_{\text{in}}}{\sqrt{2}} e^{i\varphi} , \tag{6.10}$$

where the relative phase φ is again completely assigned to a_E. Hence, the reflected field and power are

$$\begin{aligned} a_{\text{refl}} &= \frac{a_N}{\sqrt{2}} + i\frac{a_E}{\sqrt{2}} = \frac{a_{\text{in}}}{2}\left(1 + i\frac{\beta}{2}e^{i\Omega t} + i\frac{\beta}{2}e^{-i\Omega t} - e^{i\varphi}\right) \\ P_{\text{refl}} &= |a_{\text{refl}}|^2 . \end{aligned} \tag{6.11}$$

P_{refl} is detected by the photodetector, then demodulated at the frequency Ω by the mixer and low-pass filtered. Thus, terms in P_{refl} which are constant or evolve with

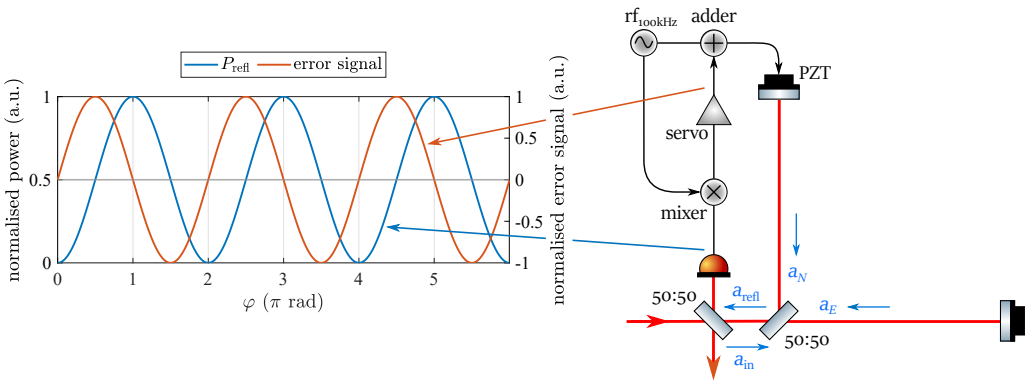

Figure 6.6: Dark fringe stabilisation: the piezo-electric transducer (PZT) modulates the phase of the light field in the north arm at a radio frequency (rf) of 100 kHz. After demodulation and low-pass filtering, the obtained error signal has zero-crossings at the bright and dark fringe.

2Ω can be neglected:

$$\begin{aligned} P_{\text{refl}} &\propto i\frac{\beta}{2}\left[-e^{i(\Omega t-\varphi)} - e^{-i(\Omega t+\varphi)} + e^{-i(\Omega t-\varphi)} + e^{i(\Omega t+\varphi)}\right] + \mathcal{O}(0\Omega) + \mathcal{O}(2\Omega) \\ &\propto \sin(\Omega t-\varphi) - \sin(\Omega t+\varphi) + \mathcal{O}(0\Omega) + \mathcal{O}(2\Omega) \end{aligned} \tag{6.12}$$

Then, the demodulation at Ω is mathematically expressed as a multiplication with $\sin(\Omega t+\varphi_{\text{demod}})$ including a demodulation phase φ_{demod}. Applying this to P_{refl} at $\varphi_{\text{demod}} = 90^\circ$ and taking the low-pass filter into account results in the following error signal

$$\epsilon(\varphi) = P_{\text{ref}} \times \sin(\Omega t + 90^\circ) \overset{\text{low-pass filter}}{\propto} \sin\varphi\,. \tag{6.13}$$

This error signal can be used to stabilise the interferometer to the bright fringe (at $\varphi = 0, 2\pi, \dots$) with respect to the photodetector in reflection, which coincides with the dark fringe with respect to the output port, because $\epsilon(0, 2\pi, \dots) = 0$ and $\frac{\mathrm{d}\,\epsilon(\varphi)}{\mathrm{d}\,\varphi}\Big|_{\varphi=(0,2\pi,\dots)} \neq 0$. This is also shown in Figure 6.6.

6.3 Results

Figure 6.7 presents the measured power spectra of the interferometer output field in the signal (phase) quadrature with and without injected squeezed states ("squeezed noise" and "vacuum noise", respectively). A maximum quantum shot noise reduction of 10.0(3) dB at a measurement frequency of 5 MHz and a harmonic OPA pump power of 55 mW could be observed in the $\text{TEM}_{0,0}$ mode. At a measurement frequency of 4 MHz, 8.8(3) dB at a pump power of 550 mW and 7.5(3) dB at a pump power of 800 mW in the $\text{HG}_{1,1}$ and $\text{HG}_{2,2}$ mode were achieved, respectively. In each case, the injected GW signal had an amplitude of about -5.3 dB and could hardly be detected in the vacuum state related noise floor. However, it appears as a distinct peak in the squeezed state related noise curves. See Section 5.2 regarding the significantly different levels of pump power.

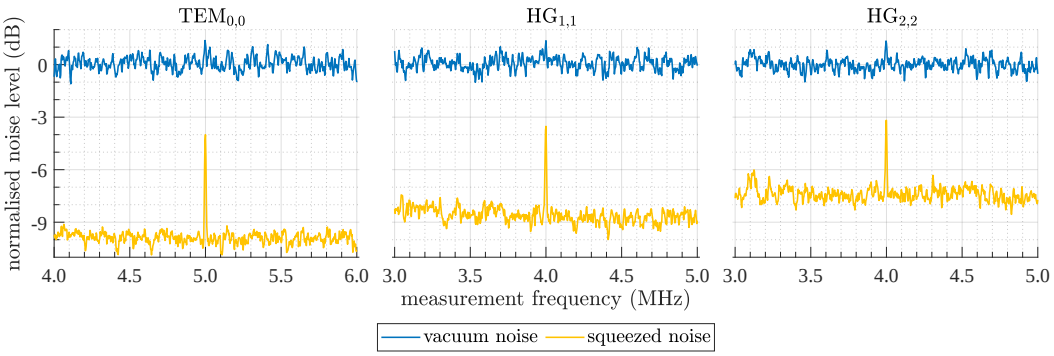

Figure 6.7: Highest measured quantum noise reduction in the $TEM_{0,0}$, $HG_{1,1}$ and $HG_{2,2}$ mode with an injected GW signal, normalised to the noise level of the vacuum state [Hei+22]. Resolution bandwidth: 10 kHz, video bandwidth: 10 Hz, electronic dark noise (not shown): about −22 dB and subtracted from the data. Anti-squeezing levels (not shown): about 18 dB ($TEM_{0,0}$), 16 dB ($HG_{1,1}$) and 15 dB ($HG_{2,2}$).

6.3.1 Technical laser noise and phase noise

In Section 5.2, technical laser noise only arose due to the residual OPA control field which was transmitted through the OPA cavity and caused a coherent amplitude in the detected squeezed field. At the measurement frequency of 4 MHz (and above), technical laser noise had no significant contribution which the fit of the theoretical model confirmed via small phase noise values. However, technical laser noise affected the measurement of the quantum noise reduction in the presented Michelson interferometer at and even above 4 MHz.

The contribution of the residual OPA control field was the same as in Sec. 5.2 since the control field was injected into the OPA cavity with the same optical power. In transmission of the OPA cavity and including the parametric deamplification, when the pump field is also injected, about 2 µW remained as a coherent amplitude in the squeezed field. The Michelson interferometer was, however, a second source for a coherent amplitude in the detected field at the homodyne detector due to contrast defects and a possible small dark fringe offset. Hence, there was always some leakage power in the output even at the dark, or darkest possible, fringe (see Tab. 6.1). This interferometer leakage power is highly sensitive to the interferometer alignment and was typically 2.5 ($TEM_{0,0}$) to 4 ($HG_{2,2}$) times as large as the power in the residual OPA control field. Since this contribution from the interferometer leakage field dominated over the power in the OPA control field, the total coherent power in the detected field was always larger than in Sec. 5.2, even if the two coherent amplitudes interfered destructively. The charateristics of the technical laser noise can be identified in the squeezed noise of each mode at low frequencies in Figure 6.9, where the noise peak in the $HG_{1,1}$ measurement was atypically large and affected the squeezing level up to a frequency of 6 MHz. This $HG_{1,1}$ measurement was prepared with the same care as the others and shows how sensitive the setup is with respect to the interferometer alignment and resulting leakage power. The preparation procedure for each measurement was done in the following order: adjusting the interferometer contrast via the PZT_1 and PZT_2 mirrors, adjusting the alignment between the squeezed field and coherent interferometer field via mirrors around PZT_4, adjusting the alignment between the squeezed field from the north arm and the LO field via mirrors around PZT_3 and adjusting the alignment between

the squeezed field from the east arm and the LO field via PZT_2. The last step is theoretically redundant and was only used as a final alignment check. Still, for the $HG_{1,1}$ measurement in Figure 6.9, this last step may have reduced the interferometer contrast unintentionally. The measurement is shown, nonetheless, for demonstration purposes.

Table 6.1: Parameters of the Michelson interferometer setup. In the category "optical loss source", the values indicate the optical loss (not efficiency) associated with the sources in the left column.

Optical loss source	$TEM_{0,0}$	$HG_{1,1}$	$HG_{2,2}$
OPA escape efficiency (%)	1.0(5)	1.0(5)	1.0(5)
Optics in path of squeezed field (%)	3.0(5)	4.0(5)	4.5(5)
Leakage to interferometer input port (%)	0.3(1)	0.3(1)	0.4(1)
Homodyne contrast (%)	2.2(6)	2.8(6)	6.0(6)
Detector's quantum efficiency (%)	0.7(4)	0.7(4)	0.7(4)
Expected detection efficiency (%)	92.8(10)	91.2(10)	87.4(10)
Fitted detection efficiency (%)	92.6(10)	91.4(10)	87.7(10)
Maximum interferometer contrast (%)	99.92(2)	99.87(2)	99.74(2)
Interferometer leakage power (µW)	5(2)	6(2)	8(2)

The larger coherent amplitude in the detected field has two consequences (as further explained in Sec. 3.2.4). First, the technical noise peak at low frequencies is larger than in Sec. 5.2 and can significantly affect the quantum noise reduction up to a frequency of 5 MHz, dependent on the achieved squeezing level. For the $HG_{1,1}$ and $HG_{2,2}$ measurement, the highest quantum noise reduction could still be observed at 4 MHz; however, the $TEM_{0,0}$ measurement reached a level where the technical laser noise limited the squeezing at 4 MHz to below 10 dB, thereby shifting the frequency of highest observed quantum noise reduction to 5 MHz. A corresponding (small) rising slope in the squeezed state related noise curves in Figure 6.7 can be identified on the left side of each signal peak. Second, the coherent amplitude in the detected field reduces the squeezing level over the whole frequency band because it beats with the vacuum fluctuations entering from the local oscillator port of the detector. In general, this leads to an effective pseudo-dark noise floor (when only the local oscillator port of the detector is blocked) that was typically observed to be 1 dB to 2 dB above the actual electronic dark noise (when both detector input ports are blocked). This effect can reduce the measured squeezing level by about 0.2 dB at 10 dB for an electronic dark noise floor of −22 dB, and only the actual electronic dark noise was subtracted in all presented measurements. This effect also appeared in the measurements in Chapter 5 but was negligible due to the smaller coherent amplitude in the detected field.

With the technical laser noise and the amplification of the LO field's vacuum fluctuations, the reduction in the squeezing level due to the coherent amplitude in the detected field dominated and masked the effect of phase noise. The latter can, thus, not be conclusively inferred for this setup. To additionally confirm that the phase noise had no significant contribution to the measurement results, the quantum noise reduction for the $TEM_{0,0}$ mode was measured at a level of 8 dB without an electronic stabilisation of the interferometer. By setting the interferometer to the dark fringe "by hand", measurements with and without the 100 kHz modulation from PZT_1 could be conducted. This modulation increases the phase noise as it causes deterministic phase jitter in one of the interferometer arms. For this comparison, the

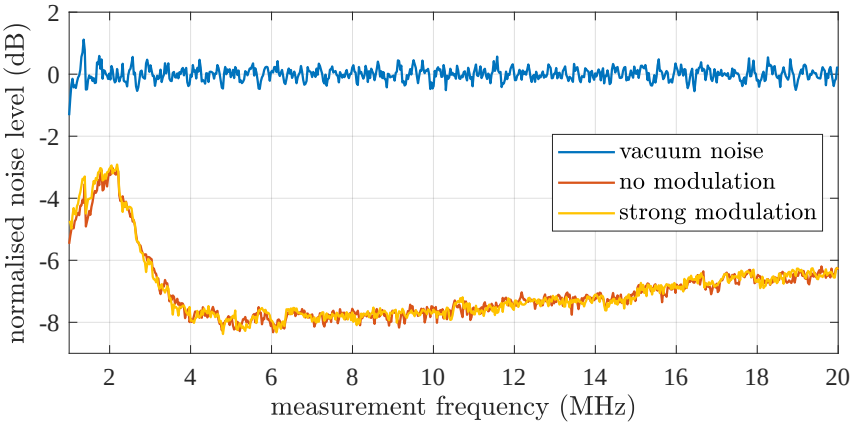

Figure 6.8: The squeezed-light reduced power spectra of the quantum noise for the $TEM_{0,0}$ mode are compared for the cases of no 100 kHz modulation via PZT_1 and a 100 kHz modulation with an amplitude five times larger than used for the results in Fig. 6.7.

modulation amplitude was increased to five times the amplitude which was used for the results in Figure 6.7; however, both measurements showed no significant differences. This indicates that the effects due to the technical laser noise dominate the effects due to phase noise. Please note, however, that the validity of this test is slightly reduced because the interferometer leakage power is likely to be larger if the interferometer is not electronically stabilised to the dark fringe. To reduce this influence, the "min hold" function of the spectrum analyser was used for both of these measurements. With this function, the spectrum analyser displays the minimum value that was measured at each frequency in several frequency scans during the total measurement time of about 10 s, thereby selecting the data points which were taken when the interferometer was closest to the dark fringe. This kind of measurement is not suited to characterise the experiment but still allows for a reasonable comparison between these two measurements.

6.3.2 Detection efficiency

The detection efficiency for the squeezed states is reduced due to a combined effect from the OPA escape efficiency, loss from optics in the path of the squeezed field, the homodyne contrast between the local oscillator and squeezed field, leakage towards the interferometer input port and the homodyne detector's quantum efficiency. The individual values for the three spatial modes are indicated in Table 6.1. The OPA escape efficiency is equal to the one in Sec. 5.2. The loss from the optics in the path of the squeezed field was determined by using a strong OPA control field and comparing the power upstream the injecting PBS to the maximum power upstream from the lenses that focus the laser beam onto the homodyne detector photodiodes when the interferometer was scanned through the fringes via PZT_1. Among the optics, the Faraday rotator in combination with the PBS causes the highest loss which amounted to about 1 % to 1.5 % per single pass and increased with the mode order due to additional clipping loss (aperture radius: about 2.5 mm, beam radius: about 1 mm). The imperfect homodyne contrast includes several influences (see Sec. 2.3.3, "Astigmatism and mode degeneracy" and "Sensitivity to spatial mismatches"): beam misalignments and mismatches in the waist size and waist position are always present in practice and cause a larger reduction in the homodyne

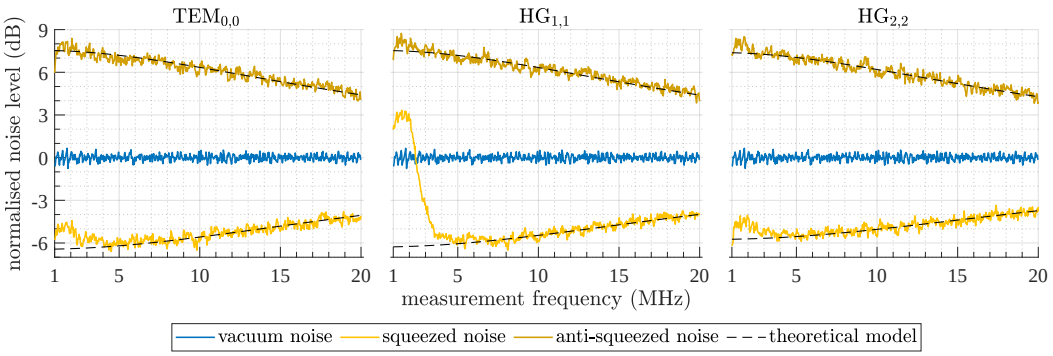

Figure 6.9: Noise power spectra for the $TEM_{0,0}$, $HG_{1,1}$ and $HG_{2,2}$ mode for low levels of anti-squeezing and no injected GW signal, normalised to the noise level of the vacuum state [Hei+22]. The results correspond to a harmonic OPA pump power of about 10 mW, 100 mW and 150 mW, respectively. Resolution bandwidth: 300 kHz, video bandwidth: 300 Hz, electronic dark noise (not shown): about −22 dB and subtracted from the data.

contrast with increasing mode order; possible rotations around the optical axis can reduce the contrast for the higher-order HG modes; and mode degeneracies are also potentially more severe for the higher-order modes. While the homodyne contrasts of the different modes were not analysed with respect to these influences, the differences between the contrasts can theoretically be explained by the first influence alone (increasing mismatch sensitivity). Specific issues with rotations or degeneracies were not observed. The leakage loss of the squeezed field towards the interferometer input port was assumed to be equal to the interferometer leakage power of the sensing field in the output port: 5 µW to 8 µW relative to the injected 1.9 mW. Finally, the quantum efficiency of the homodyne detector's photodiodes was slightly larger than in Sec. 5.2 because retro-reflectors were used to recycle the light which is reflected by the anti-reflective coated photodiodes. The resulting expected detection efficiency is also indicated in Table 6.1.

If the squeezing and anti-squeezing levels are compared to the theoretical model from Equation 3.43 at low harmonic OPA pump power and up to a measurement frequency of 20 MHz, the expected detection efficiencies can be checked against the measurement data in a regime where the measurement does not show significant disturbances from either technical laser or phase noise (see Fig. 6.9). The parameters η_{det} and P_{thr} can be varied until the optimum match between the model and the measurement data is obtained (dashed lines in Fig. 6.9). The derived values for the detection efficiencies are indicated in Tab. 6.1 and agree well with the expectations.

6.4 Summary

This chapter presented the application of squeezed states of light in higher-order Hermite-Gaussian modes in a tabletop Michelson interferometer with balanced homodyne detection, which is proposed for future gravitational-wave detectors. First, Section 6.1 explained the choice of the detection scheme and compared it to the currently used direct readout scheme. These schemes differ in how the local oscillator field is obtained. While the balanced homodyne scheme is not without challenges, it can avoid some disadvantages of the direct scheme, for instance, by suppressing the coupling of some noise sources (e.g. laser power noise) to the gravitational-wave readout. The proposed change to the balanced homodyne readout scheme in future

GWDs demands for the investigation of the quantum noise reduction in a Michelson interferometer with the balanced homodyne detection topology.

In Sections 6.2 and 6.3, a simple tabletop Michelson interferometer with an arm length of 10 cm was studied in the shot-noise limited frequency range of 4 MHz to 20 MHz. Here, the sensitivity could be improved by up to 10 dB, 8.8 dB and 7.5 dB when the interferometer was operated in the spatial modes $TEM_{0,0}$, $HG_{1,1}$ and $HG_{2,2}$, respectively. This is, to my knowledge, the first demonstration of a quantum noise reduction of 10 dB, as targeted by future gravitational-wave detectors, in any Michelson interferometer topology. So far, a squeezed-light sensitivity enhancement of 10 dB could only be achieved in a tabletop Mach-Zehnder interferometer [Zan21] which fundamentally implies less optical loss because the injection of the squeezed light does not require a Faraday rotator unit. The highest quantum noise reduction via squeezed light including a Faraday rotator unit had been 8.2 dB in a tabletop zero-area Sagnac interferometer operated in the $TEM_{0,0}$ mode [Ebe+10].

In the presented Michelson interferometer, optical loss from such a Faraday rotator unit and loss associated with the homodyne contrast primarily limited the detection efficiency for the squeezed light. Furthermore, technical laser noise, which becomes relevant due to a coherent amplitude in the detected field, further reduced the squeezing level below measurement frequencies of 5 MHz and also affected the frequency at which the highest quantum noise reduction was observed.

If a quantum noise reduction of 10 dB via squeezed light could not be achieved in a tabletop Michelson interferometer, this target would very likely not be realised in the advanced GW detectors, as well. Hence, the presented results constitute an important demonstration towards the quantum noise target in future GW detectors.

The findings, moreover, represent an unprecedented milestone for the efficient usage of nonclassical states of light in higher-order spatial modes in a measurement application. The quantum noise reduction in the $HG_{1,1}$ of 8.8 dB mode is a great achievement and could even exceed the $TEM_{0,0}$ result of 8.2 dB in [Ebe+10] even though the presented Michelson topology does not imply fundamentally less optical loss than a zero-area Sagnac topology.

Chapter 7

Summary and outlook

This thesis investigated how squeezed states of light in higher-order spatial laser modes can be efficiently generated and used in quantum metrology. While the main motivation was the proposed usage of higher-order modes for a better thermal noise reduction in future gravitational-wave (GW) detectors, these modes also offer potential benefits over the fundamental Gaussian $TEM_{0,0}$ mode in various other optical disciplines like imaging techniques and quantum communication.

Theoretically and given a spherical mirror geometry, a better thermal noise reduction in GW detectors can be achieved with both higher-order Laguerre- (LG) and Hermite-Gaussian (HG) modes. However, several experiments and theoretical studies revealed that the LG modes are highly sensitive to any kind of astigmatism in an optical system. Hence, they appear to be too challenging for their application in GW detectors and an experiment on the second harmonic generation of the $LG_{3,3}$ mode in Chapter 4 confirmed this conclusion.

Previously published results on squeezed states in higher-order spatial modes were limited to a minimum noise power level of 3 dB or 5 dB below that of a vacuum state, dependent on the implemented method. In Chapter 5, the observation of a quantum noise reduction of 10 dB in the Hermite-Gaussian $HG_{1,1}$ mode at a wavelength of 1064 nm and a measurement frequency of 4 MHz thus represents a new benchmark and significantly reduces the gap to commonly achieved squeezing levels in the $TEM_{0,0}$ mode. In the future, the presented squeezed light source could be adapted to produce squeezed vacuum states in the audio-band, e.g. by implementing control schemes similar to the squeezed light source of the GEO600 detector.

The main limitation for the detection efficiency was the increased sensitivity of higher-order modes to spatial mismatches, thereby reducing the homodyne contrast at the balanced homodyne detector. In addition, the spatial light modulators which generated the higher-order modes in the fundamental and harmonic field most likely increased the phase noise. These findings suggest that properly counteracting these two effects, e.g. via electronic control schemes and/or a different higher-order mode generation technique, will further enhance the squeezing.

In Chapter 6, the generated squeezed states were applied in a tabletop Michelson interferometer, including the more complex but also more versatile balanced homodyne detection scheme which is planned for the future GW detectors. In the $TEM_{0,0}$ operation, the first 10 dB quantum noise reduction in the Michelson topology, as targeted by the future GW detectors, could be demonstrated. Moreover, similarly strong sensitivity enhancements could be demonstrated when the interferometer was operated in the $HG_{1,1}$ and $HG_{2,2}$ mode, respectively. Here, the achieved 8.8 dB in the $HG_{1,1}$ were especially a success as they even exceed the highest previously published result for the $TEM_{0,0}$ mode in a topology with a comparable optical loss budget (zero-area Sagnac topology) by about 0.6 dB.

These results are a strong argument for an improved thermal noise mitigation in future GW detectors via higher-order spatial modes and greatly motivate further research in this field. Especially because squeezing measurements are very sensitive to several kinds of imperfections, e.g. mode impurities, spatial mismatches and beam jitter, this work is a general statement that higher-order modes can be handled with high efficiency and precision. This is in spite of the fact that these modes, taken by themelves, are already more sensitive to such spatial mismatches compared to the $TEM_{0,0}$ mode. As a next step, the tabletop Michelson interferometer could be advanced gradually towards a dual-recycled version with arm cavities, alignment control schemes and quantum enhancement in the audio-band via squeezed vacuum states. If high quantum noise reduction levels can then still be achieved in higher-order modes, these results will have a huge significance—and future GW detectors may be operated in a higher-order spatial laser mode, after all.

Appendix A

Matlab scripts

A.1 Numerical simulation of the $LG_{3,3}$ SHG

The same script was used for the $TEM_{0,0}$ mode in an adapted version.

```
clear all

focparam = ; %focusing parameter
dk = ; %wavevector mismatch

n = ; %refractive index
lambda = ; %wavelength of fund. field
L = ; % half crystal length
omega0 = sqrt( 2 * L * lambda / 2 / pi / focparam / n ); %waist fund. field
zR = pi * n * omega0^2 / lambda; %Rayleigh range of fund. field

zresolution = ; %data points along propagation axis
dz = 2 * L / ( zresolution - 1 ); %step size along propagation axis
rresolution = ; %data points in radial direction
dg06 = 13; %difference in Gouy phase factors for LG06
dg26 = 9; %...
dg46 = 5; %...
dg66 = 1; %...
frac06 = sqrt( 0.2129 ); %spatial overlap with LG33^2 for LG06
frac26 = sqrt( 0.1342 ); %...
frac46 = sqrt( 0.1610 ); %...
frac66 = sqrt( 0.4919 ); %...
fac = 1 * dz;

%obejcts for values of crys. polarisation corr. to LG06, LG26, LG46 and LG66
c06List = zeros( zresolution , 3 );
c26List = zeros( zresolution , 3 );
c46List = zeros( zresolution , 3 );
c66List = zeros( zresolution , 3 );

%objects for values of harm. field corresponding to LG06, LG26, LG46 and LG66
a06List = zeros( zresolution , 3 );
a26List = zeros( zresolution , 3 );
a46List = zeros( zresolution , 3 );
a66List = zeros( zresolution , 3 );
```

```
%objects for phase difference (and change in harmonic power)
%corresponding to LG06, LG26, LG46 and LG66
phaseDifference06 = zeros( zresolution , 2 );
phaseDifference26 = zeros( zresolution , 2 );
phaseDifference46 = zeros( zresolution , 2 );
phaseDifference66 = zeros( zresolution , 2 );

%objects for total harmonic power
PtotalList = zeros( zresolution , 1 );

m = 1; %count for iteration steps
z = -L; %initial z position

while z < L + dz %while loop through crystal

omega = omega0 * sqrt( 1 + ( z / zR )^2 ); %beam radius
%at crystal front and rear side
radius = 5 * omega; %sufficiently large radius for transverse integration
dr = radius / ( rresolution - 1 ); %step size in radial direction
r = 0 : dr : radius; %radial coordinate

%radial amplitude distribution of pump field squared at z
S = LGmode1D( 3 , 3 , omega0 , radius , rresolution , n , z , lambda );
S = S.^2;
s_abs = sqrt( abs( 2 * pi * sum( r .* conj( S ) .* S ) * dr ) );

%phase values of crystal polarisation
c06_phase = exp( 1i * dg06 * atan( z / zR ) ) * exp( 1i * dk * z );
c26_phase = exp( 1i * dg26 * atan( z / zR ) ) * exp( 1i * dk * z );
c46_phase = exp( 1i * dg46 * atan( z / zR ) ) * exp( 1i * dk * z );
c66_phase = exp( 1i * dg66 * atan( z / zR ) ) * exp( 1i * dk * z );

%full crystal polarisation term
c06 = -1i * fac * frac06 * s_abs * c06_phase;
c26 = -1i * fac * frac26 * s_abs * c26_phase;
c46 = -1i * fac * frac46 * s_abs * c46_phase;
c66 = -1i * fac * frac66 * s_abs * c66_phase;

%allocation to objects
c06List( m , 1 ) = c06;
c26List( m , 1 ) = c26;
c46List( m , 1 ) = c46;
c66List( m , 1 ) = c66;

c06List( m , 2 ) = abs( c06 )^2;
c26List( m , 2 ) = abs( c26 )^2;
c46List( m , 2 ) = abs( c46 )^2;
c66List( m , 2 ) = abs( c66 )^2;

c06List( m , 3 ) = angle( c06 );
```

```
c26List( m , 3 ) = angle( c26 );
c46List( m , 3 ) = angle( c46 );
c66List( m , 3 ) = angle( c66 );

if m == 1 %inital iteration step
%harmonic field amplitude equals crystal polarisation
a06List( m , 1 ) = c06;
a26List( m , 1 ) = c26;
a46List( m , 1 ) = c46;
a66List( m , 1 ) = c66;

%power change is equal to total harmonic power (no phase difference)
phaseDifference06( m , 2 ) = abs( a06List( m , 1 ) )^2;
phaseDifference26( m , 2 ) = abs( a26List( m , 1 ) )^2;
phaseDifference46( m , 2 ) = abs( a46List( m , 1 ) )^2;
phaseDifference66( m , 2 ) = abs( a66List( m , 1 ) )^2;

else %any other iteration step
%phase difference between harmonic field and crystal polarisation
phaseDifference06( m , 1 ) = angle( conj( a06List( m - 1 , 1 ) ) * c06 );
phaseDifference26( m , 1 ) = angle( conj( a26List( m - 1 , 1 ) ) * c26 );
phaseDifference46( m , 1 ) = angle( conj( a46List( m - 1 , 1 ) ) * c46 );
phaseDifference66( m , 1 ) = angle( conj( a66List( m - 1 , 1 ) ) * c66 );

%interference of harmonic field and crystal polarisation
a06List( m , 1 ) = a06List( m - 1 , 1 ) + c06;
a26List( m , 1 ) = a26List( m - 1 , 1 ) + c26;
a46List( m , 1 ) = a46List( m - 1 , 1 ) + c46;
a66List( m , 1 ) = a66List( m - 1 , 1 ) + c66;

%power change
phaseDifference06( m , 2 ) = abs( a06List( m , 1 ) )^2 -...
abs( a06List( m - 1 , 1 ) )^2;
phaseDifference26( m , 2 ) = abs( a26List( m , 1 ) )^2 -...
abs( a26List( m - 1 , 1 ) )^2;
phaseDifference46( m , 2 ) = abs( a46List( m , 1 ) )^2 -...
abs( a46List( m - 1 , 1 ) )^2;
phaseDifference66( m , 2 ) = abs( a66List( m , 1 ) )^2 -...
abs( a66List( m - 1 , 1 ) )^2;
end

%harmonic field amplitude converted to power
a06List( m , 2 ) = abs( a06List( m , 1 ) )^2;
a26List( m , 2 ) = abs( a26List( m , 1 ) )^2;
a46List( m , 2 ) = abs( a46List( m , 1 ) )^2;
a66List( m , 2 ) = abs( a66List( m , 1 ) )^2;

%harmonic field amplitude converted to phase
a06List( m , 3 ) = angle( a06List( m , 1 ) );
a26List( m , 3 ) = angle( a26List( m , 1 ) );
a46List( m , 3 ) = angle( a46List( m , 1 ) );
```

```
a66List( m , 3 ) = angle( a66List( m , 1 ) );

%total harmonic power as sum over all harmonic modes
PtotalList( m ) = a06List( m , 2 ) + a26List( m , 2 ) +...
a46List( m , 2 ) + a66List( m , 2 );

m = m + 1;
z = z + dz;

end
```

The function for the normalised 1D LG mode amplitude distribution:

```
function LG = LGmode1D(p,l,omega0,radius,resolution,n,z,lambda)

r = 0:radius/(resolution-1):radius;

zR = n*pi*omega0^2/lambda; %Rayleigh range
omega = omega0.*sqrt(1+(z./zR).^2); %beam radius
gouy = atan(z./zR); %part of Gouy phase term
q = z+1i*zR; % complex beam parameter
k = 2*n*pi/lambda; %wavevector

LG = 1./omega .* ...
sqrt(2*factorial(p)/(pi*factorial(abs(l)+p))) .* ...
exp(1i.*(2*p+abs(l)+1).*gouy) .* ...
(sqrt(2).*r./omega).^(abs(l)) .* ...
laguerreL(p,abs(l),2.*r.^2./omega.^2) .* ...
exp(-1i.*k.*r.^2./2./q) .* ...
exp(-1i.*k.*z);

end
```

A.2 SLM control

This is the script by which the spatial light modulator in the fundamental beam path was controlled (Hamamatsu LCOS-SLM X15213-03). The conversion from the mode's phase distribution to the SLM output image, however, differs dependent on the SLM model and was also slightly more complex for the spatial light modulator in the harmonic beam path (Hamamatsu LCOS-SLM X13138-09).

```
clear all

%% set properties of SLM model and desired mode output

%SLM parameters
xresolution = 1272;
```

```
yresolution = 1024;
xLength = 15.9e-3;
yLength = 12.8e-3;

%mode parameters
wavelength = ;
x = ; %mode index corr. to horizontal axis
y = ; %mode index corr. to vertical axis
waist = ; %desired waist of outgoing beam

%% import flatness correction and phase modulation data

correctionData = double( imread( '.bmp' ) );
convertValue = 217;

LCOS_SLM_correction = mod( correctionData , 256 );
LCOS_SLM_correction = LCOS_SLM_correction .* convertValue ./ 255;
LCOS_SLM_correction = uint8( LCOS_SLM_correction );

%% convert desired amplitude distribution into LCOS_SLM_mode image

%generate the mode's amplitude distribution
desiredMode = HGmode( x , y , waist , xresolution , yresolution ,...
xLength , yLength , wavelength );
disp( 'Mode has been successfully created!' )

%generate the mode's phase distribution
mode_phase = angle( desiredMode );
mode_inputValues = mode_phase .* 128 ./ pi;

%generate SLM phase image
LCOS_SLM_mode = mod( mode_inputValues , 256 );
LCOS_SLM_mode = LCOS_SLM_mode .* convertValue ./ 255;
LCOS_SLM_mode = uint8( LCOS_SLM_mode );
disp( 'LCOS_SLM_mode has been successfully created!' )


%% combine correction and desired data to LCOS_SLM output

output_inputValues = mode_inputValues + correctionData;

LCOS_SLM_output = mod( output_inputValues , 256 );
LCOS_SLM_output = LCOS_SLM_output .* convertValue ./ 255;
LCOS_SLM_output = uint8( LCOS_SLM_output );
disp( 'LCOS_SLM_output has been successfully created!' )
```

The function for the 2D HG mode amplitude distribution:

```
function HG = HGmode(m,n,omega0,radius,resolution,nr,z,lambda)
```

```
zR = nr*pi*omega0^2/lambda; %Rayleigh range
R = z*(1+(zR/z)^2); %wavefront radius of curvature
omega = omega0*sqrt(1+(z/zR)^2); %beam radius
gouy = atan(z/zR); %part of Gouy phase term
k = 2*nr*pi/lambda; %wavevector

%generate meshgrid from Cartesian coordinates
x = -radius:2*radius/(resolution-1):radius;
y = -radius:2*radius/(resolution-1):radius;
[x1,y1] = meshgrid(x,y);
r = sqrt(x1.^2+y1.^2);
dx = 2*radius/(resolution-1);

%generate corr. meshgrid from Hermite polynomials
hermiteH_x = hermiteH(m,sqrt(2).*x./omega);
hermiteH_y = hermiteH(n,sqrt(2).*y./omega);
[H_x,H_y] = meshgrid(hermiteH_x,hermiteH_y);

HG = omega0./omega .*...
H_x.*H_y.*...
exp(1i.*(m+n+1).*gouy).*...
exp(-r.^2./omega^2).*...
exp(-1i.*k.*r.^2./(2.*R)).*...
exp(-1i.*k.*z);

end
```

Acknowledgements

At long last, I would like to thank a great number of people who supported me over the years of my PhD at the Albert Einstein Institute.

First of all, I would like to thank Karsten Danzmann. Creating and leading an institute with such a magnificient work environment, impressive technical and financial support is an achievement just as valuable as the detection of a gravitational wave. I am greatful that I could become one of its many, many parts!

I deeply enjoyed five and a half years in the "Lasers and Squeezed Light Group" from a student assistant to the last page of this thesis. Special thanks go to Benno Willke for offering me the opportunity to work in this group on a topic which I found evermore fascinating day by day. Thank you for your trust, great input, advice and supervision, and, last but not least, for making this awesome group—in a scientific but also social regard—what it is!

My deepest gratitude also goes to Henning Vahlbruch for his excellent supervision. I consider myself truly lucky that I could learn from your expertise and could always count on your support. Working with you was much fun and our discussions were highly inspiring and encouraging. *Servus, Grüezi und Hallo!*

Next, I want to thank Team LASER and the Kranoleum gang, especially Jasper, Nina, Marina, Fabian, Nicole, Kanioar, Benjamin, Qazal, Marc, Malte, Marie, Chris and Martin. Not only for the professional discussions and support, but especially for the joyous atmosphere. I am deeply greatful that our times at the institute coincided. I'm going to miss the chats in the tea kitchen (wenn es earlte), the group activities and barbecues (even with heavy rain), the cakes (of which there were too few), the ping-pong matches ("Construction!") and so much more!

For proof-reading parts of this thesis, I would like to thank Henning, Marina, Jasper and Fabian. Thank you for your helpful suggestions which improved this thesis by up to 10 dB above the trivial-facts noise floor!

Getting an experiment to work heavily relies on proper electronics and mechanical assemblies. I would like to thank all members of the electronic and mechanical workshop. You do a fantastic job! The same holds for the IT and administration; the institute could not function without you!

I thank Alexander Franzen for providing the component library on which all schematic figures are based.

Lastly, I want to thank my family, friends and especially Hanna for all your support!

Bibliography

[Abb+16] B. P. Abbott, R. Abbott, T. D. Abbott, M. R. Abernathy, F. Acernese, K. Ackley, C. Adams, T. Adams, P. Addesso, R. X. Adhikari, et al. "Observation of Gravitational Waves from a Binary Black Hole Merger". *Phys. Rev. Lett.* 116 (6 2016), p. 061102. DOI: 10.1103/PhysRevLett.116.061102.

[Abe+18] M. Abernathy, G. Harry, J. Newport, H. Fair, M. Kinley-Hanlon, S. Hickey, I. Jiffar, A. Gretarsson, S. Penn, R. Bassiri, et al. "Bulk and shear mechanical loss of titania-doped tantala". *Phys. Lett. A* 382.33 (2018). Special Issue in memory of Professor V.B. Braginsky, pp. 2282–2288. ISSN: 0375-9601. DOI: https://doi.org/10.1016/j.physleta.2017.08.007.

[Ace+20] F. Acernese, M. Agathos, L. Aiello, A. Ain, A. Allocca, A. Amato, S. Ansoldi, S. Antier, M. Arène, N. Arnaud, et al. "Quantum Backaction on kg-Scale Mirrors: Observation of Radiation Pressure Noise in the Advanced Virgo Detector". *Phys. Rev. Lett.* 125 (13 2020), p. 131101. DOI: 10.1103/PhysRevLett.125.131101.

[Adh14] R. X. Adhikari. "Gravitational radiation detection with laser interferometry". *Rev. Mod. Phys.* 86 (1 2014), pp. 121–151. DOI: 10.1103/RevModPhys.86.121.

[Adh+20] R. X. Adhikari, K Arai, A. F. Brooks, C Wipf, O Aguiar, P Altin, B Barr, L Barsotti, R Bassiri, A Bell, et al. "A cryogenic silicon interferometer for gravitational-wave detection". *Class. Quantum Grav.* 37.16 (2020), p. 165003. DOI: 10.1088/1361-6382/ab9143.

[Aku+19] T Akutsu, M Ando, K Arai, Y Arai, S Araki, A Araya, N Aritomi, H Asada, Y Aso, S Atsuta, et al. "First cryogenic test operation of underground km-scale gravitational-wave observatory KAGRA". *Class. Quantum Grav.* 36.16 (2019), p. 165008. DOI: 10.1088/1361-6382/ab28a9.

[Aku+20] T Akutsu, M Ando, K Arai, Y Arai, S Araki, A Araya, N Aritomi, Y Aso, S Bae, Y Bae, et al. "Overview of KAGRA: Detector design and construction history". *Prog. Theor. Exp. Phys.* 2021.5 (2020), p. 125. DOI: 10.1093/ptep/ptaa125.

[Aku+21] T. Akutsu, M. Ando, K. Arai, Y. Arai, S. Araki, A. Araya, N. Aritomi, H. Asada, Y. Aso, S. Bae, et al. "Overview of KAGRA: KAGRA science". *Prog. Theor. Exp. Phys.* 2021.5 (2021), p. 120. DOI: 10.1093/ptep/ptaa120.

[Ara13] K. Arai. Tech. rep. LIGO-T1300189–v1. LIGO Scientific Collaboration, 2013.

[Ast+21] S. Ast, S. Di Pace, J. Millo, M. Pichot, M. Turconi, N. Christensen, and W. Chaibi. "Higher-order Hermite-Gauss modes for gravitational waves detection". *Phys. Rev. D* 103 (4 2021), p. 042008. DOI: 10.1103/PhysRevD.103.042008.

[Bai+21] M. Bailes, B. K. Berger, P. R. Brady, M. Branchesi, K. Danzmann, M. Evans, K. Holley-Bockelmann, B. R. Iyer, T. Kajita, S. Katsanevas, et al. "Gravitational-wave physics and astronomy in the 2020s and 2030s". *Nat. Rev. Phys.* 3 (2021), pp. 344–366. DOI: 10.1038/s42254-021-00303-8.

[Bas14] M. Bassan, ed. *Advanced Interferometers and the Search for Gravitational Waves: Lectures from the First VESF School on Advanced Detectors for Gravitational Waves*. Vol. 404. Springer, 2014.

[Ber+21] D. Bersanetti, B. Patricelli, O. J. Piccinni, F. Piergiovanni, F. Salemi, and V. Sequino. "Advanced Virgo: Status of the Detector, Latest Results and Future Prospects". *Universe* 7.9 (2021), p. 322. DOI: 10.3390/universe7090322.

[BGV00] V. B. Braginsky, M. L. Gorodetsky, and S. P. Vyatchanin. "Thermo-refractive noise in gravitational wave antennae". *Phys. Lett. A* 271.5-6 (2000), pp. 303–307. DOI: 10.1016/S0375-9601(00)00389-3.

[BHV98] F. Bondu, P. Hello, and J.-Y. Vinet. "Thermal noise in mirrors of interferometric gravitational wave antennas". *Phys. Lett. A* 246.3 (1998), pp. 227–236. ISSN: 0375-9601. DOI: https://doi.org/10.1016/S0375-9601(98)00450-2.

[BK68] G. D. Boyd and D. A. Kleinmann. "Parametric Interaction of Focused Gaussian Light Beams". *J. Appl. Phys.* 39 (1968), p. 3597. DOI: 10.1063/1.1656831.

[Bla01] E. D. Black. "An introduction to Pound-Drever-Hall laser frequency stabilization". *Am. J. Phys.* (2001). DOI: 10.1119/1.1286663.

[Bod+20] N. Bode, J. Briggs, X. Chen, M. Frede, P. Fritschel, M. Fyffe, E. Gustafson, M. Heintze, P. King, J. Liu, et al. "Advanced LIGO Laser Systems for O3 and Future Observation Runs". *Galaxies* 8.4 (2020). ISSN: 2075-4434. DOI: 10.3390/galaxies8040084.

[Bon+11] C. Bond, P. Fulda, L. Carbone, K. Kokeyama, and A. Freise. "Higher order Laguerre-Gauss mode degeneracy in realistic, high finesse cavities". *Phys. Rev. D* 84 (10 2011), p. 102002. DOI: 10.1103/PhysRevD.84.102002.

[Boy03] R. W. Boyd. *Nonlinear optics*. Academic Press, 2003.

[BTL08] P. Buchhave and P. Tidemand-Lichtenberg. "Generation of higher order Gauss-Laguerre modes in single-pass 2nd harmonic generation". *Opt. Express* 16.22 (2008), pp. 17952–17961. DOI: 10.1364/OE.16.017952.

[Bui+20] A. Buikema, C. Cahillane, G. L. Mansell, C. D. Blair, R. Abbott, C. Adams, R. X. Adhikari, A. Ananyeva, S. Appert, K. Arai, et al. "Sensitivity and performance of the Advanced LIGO detectors in the third observing run". *Phys. Rev. D* 102 (6 2020), p. 062003. DOI: 10.1103/PhysRevD.102.062003.

[BV03] V. B. Braginsky and S. P. Vyatchanin. "Thermodynamical fluctuations in optical mirror coatings". *Phys. Lett. A* 312.3-4 (2003), pp. 244–255. DOI: 10.1016/S0375-9601(03)00473-0.

[Car+13] L. Carbone, C. Bogan, P. Fulda, A. Freise, and B. Willke. "Generation of High-Purity Higher-Order Laguerre-Gauss Beams at High Laser Power". *Phys. Rev. Lett.* 110 (25 2013), p. 251101. DOI: 10.1103/PhysRevLett.110.251101.

[Cav81] C. M. Caves. "Quantum-mechanical noise in an interferometer". *Phys. Rev. D* 23 (8 1981), pp. 1693–1708. DOI: 10.1103/PhysRevD.23.1693.

[CB11] W. Chaibi and F. Bondu. "Optomechanical issues in the gravitational wave detector Advanced VIRGO". *C. Re. Phys.* 12.9 (2011). Nano- and micro-optomechanical systems, pp. 888–897. ISSN: 1631-0705. DOI: 10.1016/j.crhy.2011.07.004.

[Che07] S. Chelkowski. "Squeezed Light and Laser InterferometricGravitational Wave Detectors". PhD thesis. Gottfried Wilhelm Leibniz Universität Hannover, 2007. DOI: 10.15488/6848.

[Che+07] S. Chelkowski, H. Vahlbruch, K. Danzmann, and R. Schnabel. "Coherent control of broadband vacuum squeezing". *Phys. Rev. A* 75 (4 2007), p. 043814. DOI: 10.1103/PhysRevA.75.043814.

[CM04] T. Corbitt and N. Mavalvala. "Review: Quantum noise in gravitational-wave interferometers". *Journal of Optics B: Quantum and Semiclassical Optics* 6.8 (2004), S675–S683. DOI: 10.1088/1464-4266/6/8/008.

[CM22] N. Christensen and R. Meyer. "Parameter estimation with gravitational waves". *Rev. Mod. Phys.* 94 (2 2022), p. 025001. DOI: 10.1103/RevModPhys.94.025001.

[Cou+97] J. Courtial, K. Dholakia, L. Allen, and M. J. Padgett. "Second-harmonic generation and the conservation of orbital angular momentum with high-order Laguerre-Gaussian modes". *Phys. Rev. A* 56 (5 1997), pp. 4193–4196. DOI: 10.1103/PhysRevA.56.4193.

[CW51] H. B. Callen and T. A. Welton. "Irreversibility and Generalized Noise". *Phys. Rev.* 83 (1 1951), pp. 34–40. DOI: 10.1103/PhysRev.83.34.

[D'A03] E. D'Ambrosio. "Nonspherical mirrors to reduce thermoelastic noise in advanced gravitational wave interferometers". *Phys. Rev. D* 67 (10 2003), p. 102004. DOI: 10.1103/PhysRevD.67.102004.

[Del+07] V. Delaubert, M. Lassen, D. Pulford, H. A. Bachor, and C. C. Harb. "Spatial mode discrimination using second harmonic generation". *Opt. Express* 15.9 (2007), pp. 5815–5826. DOI: 10.1364/OE.15.005815.

[Dho+96] K. Dholakia, N. B. Simpson, M. J. Padgett, and L. Allen. "Second-harmonic generation and the orbital angular momentum of light". *Phys. Rev. A* 54 (5 1996), R3742–R3745. DOI: 10.1103/PhysRevA.54.R3742.

[Dic21] J. Dickmann. "Thermal noise computation of arbitrary masses in optical interferometers from first principles". *Opt. Express* 29.22 (2021), pp. 36546–36558. DOI: 10.1364/OE.438507.

[DKM19] S. L. Danilishin, F. Y. Khalili, and H. Miao. "Advanced quantum techniques for future gravitational-wave detectors". *Living Rev. Relativ.* 22 (2019). DOI: 10.1007/s41114-019-0018-y.

[Dre96] R. W. P. Drever. "Concepts for extending the ultimate sensitivity of interferometricgravitational wave detectors using non-transmissive optics withdiractive or holographic coupling". *Proceedings of the Seventh Marcel Grossman Meeting on general relativity* (1996).

[Ebe+10] T. Eberle, S. Steinlechner, J. Bauchrowitz, V. Händchen, H. Vahlbruch, M. Mehmet, H. Müller-Ebhardt, and R. Schnabel. "Quantum Enhancement of the Zero-Area Sagnac Interferometer Topology for Gravitational Wave Detection". *Phys. Rev. Lett.* 104 (25 2010), p. 251102. DOI: 10.1103/PhysRevLett.104.251102.

[Ebe13] T. Eberle. "Realization of Finite-Size Quantum Key Distribution based on Einstein-Podolsky-Rosen Entangled Light". PhD thesis. Gottfried Wilhelm Leibniz Universität Hannover, 2013. DOI: 10.15488/8040.

[Ein14] A. Einstein. "Die formale Grundlage der allgemeinen Relativitätstheorie". *Sitzungsber. Preuss. Akad. Wiss. Berlin* (1914), p. 1030.

[Ein18] A. Einstein. "Über Gravitationswellen". *Sitzungsber. Preuss. Akad. Wiss. Berlin* (1918), p. 154.

[ET 20] ET Steering Committee. *ET Design Report Update 2020*. http://www.et-gw.eu/index.php/relevant-et-documents. Accessed: 2022-04-02. 2020.

[Eur] European Gravitational Observatory. *ET sensitivities page*. http://www.et-gw.eu/index.php/etsensitivities. Accessed: 2022-04-12.

[Eva+08] M. Evans, S. Ballmer, M. Fejer, P. Fritschel, G. Harry, and G. Ogin. "Thermo-optic noise in coated mirrors for high-precision optical measurements". *Phys. Rev. D* 78 (10 2008), p. 102003. DOI: 10.1103/PhysRevD.78.102003.

[Eva+21] M. Evans, R. X. Adhikari, C. Afle, S. W. Ballmer, S. Biscoveanu, S. Borhanian, D. A. Brown, Y. Chen, R. Eisenstein, A. Gruson, et al. "A Horizon Study for Cosmic Explorer: Science, Observatories, and Community". *arXiv:2109.09882* (2021). DOI: 10.48550/arXiv.2109.09882.

[FEF14] P. Fritschel, M. Evans, and V. Frolov. "Balanced homodyne readout for quantum limited gravitational wave detectors". *Opt. Express* 22.4 (2014), pp. 4224–4234. DOI: 10.1364/OE.22.004224.

[Fox06] M. Fox. *Quantum Optics: An Introduction*. Oxford University Press, 2006.

[Ful+10] P. Fulda, K. Kokeyama, S. Chelkowski, and A. Freise. "Experimental demonstration of higher-order Laguerre-Gauss mode interferometry". *Phys. Rev. D* 82 (1 2010), p. 012002. DOI: 10.1103/PhysRevD.82.012002.

[Ful12] P. Fulda. "Precision Interferometry in a new shape: Higher-Order Laguerre-Gauss modes for gravitational-wave detectors". PhD thesis. University of Birmingham, 2012.

[Ful+17] P. Fulda, D. Voss, C. Mueller, L. F. Ortega, G. Ciani, G. Mueller, and D. B. Tanner. "Alignment sensing for optical cavities using radio-frequency jitter modulation". *Appl. Opt.* 56.13 (2017), pp. 3879–3888. DOI: 10.1364/AO.56.003879.

[Gat+14] A. Gatto, M. Tacca, F. Kéfélian, C. Buy, and M. Barsuglia. "Fabry-Pérot-Michelson interferometer using higher-order Laguerre-Gauss modes". *Phys. Rev. D* 90 (12 2014), p. 122011. DOI: 10.1103/PhysRevD.90.122011.

[GK05] C. C. Gerry and P. L. Knight. *Introductory Quantum Optics*. Cambridge University Press, 2005.

[Gon00] G. Gonzáles. "Suspension thermal noise in the LIGO gravitational wave detector". *Class. Quantum Grav.* 17.21 (2000), p. 4409. DOI: 10.1088/0264-9381/17/21/305.

[Goß+10] S Goßler, A Bertolini, M Born, Y Chen, K Dahl, D Gering, C Gräf, G Heinzel, S Hild, F Kawazoe, et al. "The AEI 10 m prototype interferometer". *Class. Quantum Grav.* 27.8 (2010), p. 084023. DOI: 10.1088/0264-9381/27/8/084023.

[GP63] M. Gertsenshtein and V. Pustovoit. "On the Detection of Low Frequency Gravitational Waves". *Sov. Phys. JETP* 16.2 (1963), p. 433.

[Gra+98] M. B. Gray, A. J. Stevenson, H.-A. Bachor, and D. E. McClelland. "Broadband and tuned signal recycling with a simple Michelson interferometer". *Appl. Opt.* 37.25 (1998), pp. 5886–5893. DOI: 10.1364/AO.37.005886.

[Guo+17] J. Guo, C. Cai, L. Ma, K. Liu, H. Sun, and J. Gao. "Higher order mode entanglement in a type II optical parametric oscillator". *Opt. Express* 25.5 (2017), pp. 4985–4993. DOI: 10.1364/OE.25.004985.

[Gur+11] A. G. Gurkovsky, D. Heinert, S. Hild, R. Nawrodt, K. Somiya, S. P. Vyatchanin, and H. Wittel. "Reducing thermal noise in future gravitational wave detectors by employing Khalili etalons". *Phys. Lett. A* 375.46 (2011), pp. 4147–4157. ISSN: 0375-9601. DOI: https://doi.org/10.1016/j.physleta.2011.07.063.

[Hal] E. Hall. *pygwinc*. https://git.ligo.org/gwinc/pygwinc. Accessed: 2022-04-01.

[Hal+09] J. Hallam, S. Chelkowski, A. Freise, S. Hild, B. Barr, K. A. Strain, O. Burmeister, and R. Schnabel. "Coupling of lateral grating displacement to the output ports of a diffractive Fabry–Perot cavity". *Journal of Optics A: Pure and Applied Optics* 11.8 (2009), p. 085502. DOI: 10.1088/1464-4258/11/8/085502.

[Har+16] M. J. Hart, R. Bassiri, K. B. Borisenko, M. Véron, E. F. Rauch, I. W. Martin, S. Rowan, M. M. Fejer, and I. MacLaren. "Medium range structural order in amorphous tantala spatially resolved with changes to atomic structure by thermal annealing". *J. Non. Cryst. Solids.* 438 (2016), pp. 10–17. ISSN: 0022-3093. DOI: https://doi.org/10.1016/j.jnoncrysol.2016.02.005.

[Hei+22] J. Heinze, K. Danzmann, B. Willke, and H. Vahlbruch. "10 dB Quantum-Enhanced Michelson Interferometer with Balanced Homodyne Detection". *Phys. Rev. Lett.* 129 (3 2022), p. 031101. DOI: 10.1103/PhysRevLett.129.031101.

[Heu18] M. Heurs. "Gravitational wave detection using laser interferometry beyond the standard quantum limit". *Phil. Trans. R. Soc. A* 376.20170289 (2018). DOI: 10.1098/rsta.2017.0289.

[HL18] T. D. Huang and T. H. Lu. "Large astigmatic laser cavity modes and astigmatic compensation". *Appl. Phys. B* 124.72 (2018). DOI: 10.1007/s00340-018-6943-8.

[Hon+11] T. Hong, J. Miller, H. Yamamoto, Y. Chen, and R. Adhikari. "Effects of mirror aberrations on Laguerre-Gaussian beams in interferometric gravitational-wave detectors". *Phys. Rev. D* 84 (10 2011), p. 102001. DOI: 10.1103/PhysRevD.84.102001.

[Hon+13] T. Hong, H. Yang, E. K. Gustafson, R. X. Adhikari, and Y. Chen. "Brownian thermal noise in multilayer coated mirrors". *Phys. Rev. D* 87 (8 2013), p. 082001. DOI: 10.1103/PhysRevD.87.082001.

[HT75] R. A. Hulse and J. H. Taylor. "Discovery of a pulsar in a binary system". *Astrophys. J.* 195.2 (1975), pp. L51–L53. DOI: 10.1086/181708.

[HVW20a] J. Heinze, H. Vahlbruch, and B. Willke. "Frequency-doubling of continuous laser light in the Laguerre-Gaussian modes $LG_{0,0}$ and $LG_{3,3}$". *Opt. Lett.* 45.18 (2020), pp. 5262–5265. DOI: 10.1364/OL.402371.

[HVW20b] J. Heinze, H. Vahlbruch, and B. Willke. "Numerical analysis of $LG_{3,3}$ second harmonic generation in comparison to the $LG_{0,0}$ case". *Opt. Express* 28.24 (2020), pp. 35816–35832. DOI: 10.1364/OE.409507.

[HWV22] J. Heinze, B. Willke, and H. Vahlbruch. "Observation of Squeezed States of Light in Higher-Order Hermite-Gaussian Modes with a Quantum Noise Reduction of up to 10 dB". *Phys. Rev. Lett.* 128 (8 2022), p. 083606. DOI: 10.1103/PhysRevLett.128.083606.

[Jes+08] A. Jesacher, C. Maurer, A. Schwaighofer, S. Bernet, and M. Ritsch-Mart1. "Near-perfect hologram reconstruction with a spatial light modulator". *Opt. Express* 16.4 (2008), pp. 2597–2603. DOI: 10.1364/OE.16.002597.

[JF20] A. W. Jones and A. Freise. "Increased sensitivity of higher-order laser beams to mode mismatches". *Opt. Lett.* 45.20 (2020), pp. 5876–5878. DOI: 10.1364/OL.403802.

[KAG22] KAGRA Collaboration. "Performance of the KAGRA detector during the first joint observation with GEO 600 (O3GK)". *arXiv:2203.07011* (2022). DOI: 10.48550/arXiv.2203.07011.

[Kha05] F. Y. Khalili. "Reducing the mirrors coating noise in laser gravitational-wave antennae by means of double mirrors". *Phys. Lett. A* 334.1 (2005), pp. 67–72. ISSN: 0375-9601. DOI: https://doi.org/10.1016/j.physleta.2004.10.078.

[KW08] P. Kwee and B. Willke. "Automatic laser beam characterization of monolithic Nd:YAG nonplanar ring lasers". *Appl. Opt.* 47.32 (2008), pp. 6022–6032. DOI: 10.1364/AO.47.006022.

[Kwe+07] P. Kwee, F. Seifert, B. Willke, and K. Danzmann. "Laser beam quality and pointing measurement with an optical resonator". *Rev. Sci. Instrum.* 78 (2007), p. 073103. DOI: 10.1063/1.2754400.

[Kwe+14] P. Kwee, J. Miller, T. Isogai, L. Barsotti, and M. Evans. "Decoherence and degradation of squeezed states in quantum filter cavities". *Phys. Rev. D* 90 (6 2014), p. 062006. DOI: 10.1103/PhysRevD.90.062006.

[Las+06] M. Lassen, V. Delaubert, C. C. Harb, P. K. Lam, N. Treps, and H.-A. Bachor. "Generation of squeezing in higher order Hermite-Gaussian modes with an optical parametric amplifier". *J. Eur. Opt. Soc.* 1 (2006), p. 06003. DOI: 10.2971/jeos.2006.06003.

[Las+07] M. Lassen, V. Delaubert, J. Janousek, K. Wagner, H.-A. Bachor, P. K. Lam, N. Treps, P. Buchhave, C. Fabre, and C. C. Harb. "Tools for Multi-mode Quantum Information: Modulation, Detection, and Spatial Quantum Correlations". *Phys. Rev. Lett.* 98 (8 2007), p. 083602. DOI: 10.1103/PhysRevLett.98.083602.

[Las10] N. Lastzka. "Numerical modelling of classical and quantum effects in non-linear optical systems". PhD thesis. Gottfried Wilhelm Leibniz Universität Hannover, 2010. DOI: 10.15488/7447.

[Lev98] Y. Levin. "Internal thermal noise in the LIGO test masses: A direct approach". *Phys. Rev. D* 57 (2 1998), pp. 659–663. DOI: 10.1103/PhysRevD.57.659.

[Lou+21] J. Lough, E. Schreiber, F. Bergamin, H. Grote, M. Mehmet, H. Vahlbruch, C. Affeldt, M. Brinkmann, A. Bisht, V. Kringel, et al. "First Demonstration of 6 dB Quantum Noise Reduction in a Kilometer Scale Gravitational Wave Observatory". *Phys. Rev. Lett.* 126 (4 2021), p. 041102. DOI: 10.1103/PhysRevLett.126.041102.

[LS07] N. Lastzka and R. Schnabel. "The Gouy phase shift in nonlinear interactions of waves". *Opt. Express* 15.12 (2007), pp. 7211–7217. DOI: 10.1364/OE.15.007211.

[LT00] Y. T. Liu and K. S. Thorne. "Thermoelastic noise and homogeneous thermal noise in finite sized gravitational-wave test masses". *Phys. Rev. D* 62 (12 2000), p. 122002. DOI: 10.1103/PhysRevD.62.122002.

[M. 10] M. Lorenzini on behalf of the Virgo Collaboration. "The monolithic suspension for the Virgo interferometer". *Classical and Quantum Gravity* 27.8 (2010), p. 084021. DOI: 10.1088/0264-9381/27/8/084021.

[Ma+20] L. Ma, H. Guo, H. Sun, K. Liu, B. Su, and J. Gao. "Generation of squeezed states of light in arbitrary complex amplitude transverse distribution". *Photon. Res.* 8.9 (2020), pp. 1422–1427. DOI: 10.1364/PRJ.388956.

[Mal06] M. Malec. "Commissioning of advanced, dual-recycled gravitational-wave detectors: simulations of complex optical systems guided by the phasor picture". PhD thesis. Gottfried Wilhelm Leibniz Universität Hannover, 2006. DOI: 10.15488/6761.

[McG+78] D. F. McGuigan, C. C. Lam, R. Q. Gram, A. W. Hoffman, D. H. Douglass, and H. W. Gutche. "Measurements of the mechanical Q of single-crystal silicon at low temperatures". *J. Low Temp. Phys.* 30.5-6 (1978), pp. 621–629.

[Meh12] M. Mehmet. "Squeezed light at 1064 nm and 1550 nm with a nonclassical noise suppression beyond 10 dB". PhD thesis. Gottfried Wilhelm Leibniz Universität Hannover, 2012. DOI: 10.15488/7913.

[Miz+93] J. Mizuno, K. A. Strain, P. G. Nelson, J. M. Chen, R. Schilling, A. Rüdiger, W. Winkler, and K. Danzmann. "Resonant sideband extraction: a new configuration for interferometric gravitational wave detectors". *Physics Letters A* 175.5 (1993), pp. 273–276. ISSN: 0375-9601. DOI: https://doi.org/10.1016/0375-9601(93)90620-F.

[MTV06] B. Mours, E. Tournefier, and J.-Y. Vinet. "Thermal noise reduction in interferometric gravitational wave antennas: using high order TEM modes". *Class. Quantum Grav.* 23.20 (2006), pp. 5777–5784. DOI: 10.1088/0264-9381/23/20/001.

[MTW73] C. W. Misner, K. S. Thorne, and J. A. Wheeler. *Gravitation*. W. H. Freeman and Company, 1973.

[MV20] M. Mehmet and H. Vahlbruch. "The Squeezed Light Source for the Advanced Virgo Detector in the Observation Run O3". *Galaxies* 8.4 (2020), p. 79. DOI: 10.3390/galaxies8040079.

[MW22] F. Meylahn and B. Willke. "Characterization of Laser Systems at 1550 nm Wavelength for Future Gravitational Wave Detectors". *Instruments* 6.1 (2022). ISSN: 2410-390X. DOI: 10.3390/instruments6010015.

[NBW17] A. Noack, C. Bogan, and B. Willke. "Higher-order Laguerre-Gauss modes in (non-) planar four-mirror cavities for future gravitational wave detectors". *Opt. Lett.* 42.4 (2017), pp. 751–754. DOI: 10.1364/OL.42.000751.

[Nit+21] A. H. Nitz, S. Kumar, Y.-F. Wang, S. Kastha, S. Wu, M. Schäfer, R. Dhurkunde, and C. D. Capano. "4-OGC: Catalog of gravitational waves from compact-binary mergers". *arXiv:2112.06878* (2021). DOI: 10.48550/arXiv.2112.06878.

[PCK92] E. S. Polzik, J. Carri, and H. J. Kimble. "Atomic spectroscopy with squeezed light for sensitivity beyond the vacuum-state limit". *Appl. Phys. B* 55 (1992), pp. 279–290. DOI: 10.1007/BF00325016.

[Pli+98] M. V. Plissi, K. A. Strain, C. I. Torrie, N. A. Robertson, S. Killbourn, S. Rowan, S. M. Twyford, H. Ward, K. D. Skeldon, and J. Hough. "Aspects of the suspension system for GEO 600". *Rev. Sci. Instrum.* 69 (1998), p. 3055. DOI: 10.1063/1.1149054.

[Pol21] E. Polini. "Broadband quantum noise reduction via frequency dependent squeezing for Advanced Virgo Plus". *Physica Scripta* 96.8 (2021), p. 084003. DOI: 10.1088/1402-4896/abfef0.

[RGR21] C. Roh, G. Gwak, and Y.-S. Ra. "Robust squeezed light against mode mismatch using a self imaging optical parametric oscillator". *Sci. Rep.* 11 (2021), p. 18991. DOI: 10.1038/s41598-021-98328-7.

[RM16] S. Reid and I. W. Martin. "Development of Mirror Coatings for Gravitational Wave Detectors". *Coatings* 6.4 (2016). ISSN: 2079-6412. DOI: 10.3390/coatings6040061.

[Sat13] B. S. Sathyaprakash. "Gravitational waves and astrophysical sources". *C. R. Phys.* 14.4 (2013), pp. 272–287. DOI: 10.1016/j.crhy.2013.01.005.

[Sau90] P. R. Saulson. "Thermal noise in mechanical experiments". *Phys. Rev. D* 42 (8 1990), pp. 2437–2445. DOI: 10.1103/PhysRevD.42.2437.

[Sau94] P. R. Saulson. *Fundamentals if Interferometric Gravitational Wave Detectors*. World Scientific, 1994. DOI: 10.1142/2410.

[SG16] A. Saha and S. Gangopadhyay. "Resonant detectors of gravitational wave as a possible probe of the noncommutative structure of space". *Class. Quantum Grav.* 33.20 (2016), p. 205006. DOI: 10.1088/0264-9381/33/20/205006.

[Sie86] A. E. Siegman. *Lasers*. University Science Books, 1986.

[Sor+13] B Sorazu, P. J. Fulda, B. W. Barr, A. S. Bell, C Bond, L Carbone, A Freise, S Hild, S. H. Huttner, J Macarthur, et al. "Experimental test of higher-order Laguerre-Gauss modes in the 10 m Glasgow prototype interferometer". *Class. Quantum Grav.* 30.3 (2013), p. 035004. DOI: 10.1088/0264-9381/30/3/035004.

[Ste+15] S. Steinlechner, B. W. Barr, A. S. Bell, S. L. Danilishin, A. Gläfke, C. Gräf, J.-S. Hennig, E. A. Houston, S. H. Huttner, S. S. Leavey, et al. "Local-oscillator noise coupling in balanced homodyne readout for advanced gravitational wave detectors". *Phys. Rev. D* 92 (7 2015), p. 072009. DOI: 10.1103/PhysRevD.92.072009.

[Ste18] J. Steinlechner. "Development of mirror coatings for gravitational-wave detectors". *Phil. Trans. R. Soc. A* 376 (2018), p. 0282. DOI: 10.1098/rsta.2017.0282.

[Ste+18] S. Steinlechner, N.-O. Rohweder, M. Korobko, D. Töyrä, A. Freise, and R. Schnabel. "Mitigating Mode-Matching Loss in Nonclassical Laser Interferometry". *Phys. Rev. Lett.* 121 (26 2018), p. 263602. DOI: 10.1103/PhysRevLett.121.263602.

[Tao+21a] L. Tao, P. Fulda, A. Green, and J. Kelley-Derzon. "Alignment and mode mismatch sensing for higher-order Hermite-Gauss modes in interferometric gravitational wave detectors". In: *APS April Meeting Abstracts*. Vol. 2021. 2021, S16.005.

[Tao+21b] L. Tao, J. Kelley-Derzon, A. C. Green, and P. Fulda. "Power coupling losses for misaligned and mode-mismatched higher-order Hermite–Gauss modes". *Opt. Lett.* 46.11 (2021), pp. 2694–2697. DOI: 10.1364/OL.426999.

[Tar+07] M. G. Tarallo, J. Miller, J. Agresti, E. D'Ambrosio, R. DeSalvo, D. Forest, B. Lagrange, J. M. Mackowsky, C. Michel, J. L. Montorio, et al. "Generation of a flat-top laser beam for gravitational wave detectors by means of a nonspherical Fabry-Perot resonator". *Appl. Opt.* 46.26 (2007), pp. 6648–6654. DOI: 10.1364/AO.46.006648.

[TGF20] L. Tao, A. Green, and P. Fulda. "Higher-order Hermite-Gauss modes as a robust flat beam in interferometric gravitational wave detectors". *Phys. Rev. D* 102 (12 2020), p. 122002. DOI: 10.1103/PhysRevD.102.122002.

[The17] The Royal Swedish Academy of Sciences. *Scientific background: The laser interferometer gravitational-wave observatory and the first direct observation of gravitational waves*. https://www.nobelprize.org/prizes/physics/2017/advanced-information/. Accessed: 2022-05-10. 2017.

[Tra+00] S. Traeger, P. Beyersdorf, L. Goddard, E. Gustafson, M. M. Fejer, and R. L. Byer. "Polarization Sagnac interferometer with a reflective grating beam splitter". *Opt. Lett.* 25.10 (2000), pp. 722–724. DOI: 10.1364/OL.25.000722.

[Tri+16] J. P. Trinastic, R. Hamdan, C. Billman, and H.-P. Cheng. "Molecular dynamics modeling of mechanical loss in amorphous tantala and titania-doped tantala". *Phys. Rev. B* 93 (1 2016), p. 014105. DOI: 10.1103/PhysRevB.93.014105.

[Tse+19] M. Tse, H. Yu, N. Kijbunchoo, A. Fernandez-Galiana, P. Dupej, L. Barsotti, C. D. Blair, D. D. Brown, S. E. Dwyer, A. Effler, et al. "Quantum-Enhanced Advanced LIGO Detectors in the Era of Gravitational-Wave Astronomy". *Phys. Rev. Lett.* 123 (23 2019), p. 231107. DOI: 10.1103/PhysRevLett.123.231107.

[Uch+12] T. Uchiyama, S. Miyoki, S. Telada, K. Yamamoto, M. Ohashi, K. Agatsuma, K. Arai, M.-K. Fujimoto, T. Haruyama, S. Kawamura, et al. "Reduction of Thermal Fluctuations in a Cryogenic Laser Interferometric Gravitational Wave Detector". *Phys. Rev. Lett.* 108 (14 2012), p. 141101. DOI: 10.1103/PhysRevLett.108.141101.

[UP+13] N. Uribe-Patarroyo, A. Fraine, D. S. Simon, O. Minaeva, and A. V. Sergienko. "Object Identification Using Correlated Orbital Angular Momentum States". *Phys. Rev. Lett.* 110 (4 2013), p. 043601. DOI: 10.1103/PhysRevLett.110.043601.

[Vah+06] H. Vahlbruch, S. Chelkowski, B. Hage, A. Franzen, K. Danzmann, and R. Schnabel. "Coherent Control of Vacuum Squeezing in the Gravitational-Wave Detection Band". *Phys. Rev. Lett.* 97 (1 2006), p. 011101. DOI: 10.1103/PhysRevLett.97.011101.

[Vah08] H. Vahlbruch. "Squeezed Light for Gravitational Wave Astronomy". PhD thesis. Gottfried Wilhelm Leibniz Universität Hannover, 2008. DOI: 10.15488/7152.

[Vah+08] H. Vahlbruch, M. Mehmet, S. Chelkowski, B. Hage, A. Franzen, N. Lastzka, S. Goßler, K. Danzmann, and R. Schnabel. "Observation of Squeezed Light with 10-dB Quantum-Noise Reduction". *Phys. Rev. Lett.* 100 (3 2008), p. 033602. DOI: 10.1103/PhysRevLett.100.033602.

[Vah+10] H. Vahlbruch, A. Khalaidovski, N. Lastzka, C. Gräf, K. Danzmann, and R. Schnabel. "The GEO 600 squeezed light source". *Classical and Quantum Gravity* 27.8 (2010), p. 084027. DOI: 10.1088/0264-9381/27/8/084027.

[Vah+16] H. Vahlbruch, M. Mehmet, K. Danzmann, and R. Schnabel. "Detection of 15 dB Squeezed States of Light and their Application for the Absolute Calibration of Photoelectric Quantum Efficiency". *Phys. Rev. Lett.* 117 (11 2016), p. 110801. DOI: 10.1103/PhysRevLett.117.110801.

[Vin09] J. Y. Vinet. "On Special Optical Modes and Thermal Issues in Advanced Gravitational Wave Interferometric Detectors". *Living Rev. Relativ.* 12.5 (2009). DOI: 10.12942/lrr-2009-5.

[Vin10] J.-Y. Vinet. "Thermal noise in advanced gravitational wave interferometric antennas: A comparison between arbitrary order Hermite and Laguerre Gaussian modes". *Phys. Rev. D* 82 (4 2010), p. 042003. DOI: 10.1103/PhysRevD.82.042003.

[Web69] J. Weber. "Evidence for Discovery of Gravitational Radiation". *Phys. Rev. Lett.* 22.24 (1969), pp. 1320–1324. DOI: 10.1103/PhysRevLett.22.1320.

[WH16] J. M. Weisberg and Y. Huang. "Relativistic measurements from timing the binary pulsar PSR B1913+16". *Astrophys. J.* 829.1 (2016), p. 55. DOI: 10.3847/0004-637x/829/1/55.

[Wil14] C. M. Will. "The Confrontation between General Relativity and Experiment". *Living Rev. Relativ.* 17.4 (2014). DOI: 10.12942/lrr-2014-4.

[WT81] J. M. Weisberg and J. H. Taylor. "Gravitational radiation from an orbiting pulsar". *Gen. Relativ. Gravit.* 13 (1981), pp. 1–6. DOI: 10.1007/BF00766292.

[Yu+18] H. Yu, D. Martynov, S. Vitale, M. Evans, D. Shoemaker, B. Barr, G. Hammond, S. Hild, J. Hough, S. Huttner, et al. "Prospects for Detecting Gravitational Waves at 5 Hz with Ground-Based Detectors". *Phys. Rev. Lett.* 120 (14 2018), p. 141102. DOI: 10.1103/PhysRevLett.120.141102.

[Zan21] J. Zander. "Squeezed and Entangled Light: From Foundations of Quantum Mechanics to Quantum Sensing". PhD thesis. Universität Hamburg, 2021.

[Zha+17] T. Zhang, S. L. Danilishin, S. Steinlechner, B. W. Barr, A. S. Bell, P. Dupej, C. Gräf, J.-S. Hennig, E. A. Houston, S. H. Huttner, et al. "Effects of static and dynamic higher-order optical modes in balanced homodyne readout for future gravitational waves detectors". *Phys. Rev. D* 95 (6 2017), p. 062001. DOI: 10.1103/PhysRevD.95.062001.

[Zha+20] Y. Zhao, N. Aritomi, E. Capocasa, M. Leonardi, M. Eisenmann, Y. Guo, E. Polini, A. Tomura, K. Arai, Y. Aso, et al. "Frequency-Dependent Squeezed Vacuum Source for Broadband Quantum Noise Reduction in Advanced Gravitational-Wave Detectors". *Phys. Rev. Lett.* 124 (17 2020), p. 171101. DOI: 10.1103/PhysRevLett.124.171101.

[Zho+14] Z.-Y. Zhou, Y. Li, D.-S. Ding, W. Zhang, S. Shi, B.-S. Shi, and G.-C. Guo. "Highly efficient second harmonic generation of a light carrying orbital angular momentum in an external cavity". *Opt. Express* 22.19 (2014), pp. 23673–23678. DOI: 10.1364/OE.22.023673.